Institut für Biochemie und Biologie
Arbeitsgruppe Molekulare Bioanalytik und Bioelektronik

Electric field-assisted immobilization and alignment of biomolecules

Dissertation zur Erlangung des akademischen Grades
"doctor rerum naturalium" (Dr. rer. nat.)
in der Wissenschaftsdisziplin Bioanalytik

eingereicht an der
Mathematisch-Naturwissenschaftlichen Fakultät
der Universität Potsdam

von
Eva-Maria Laux

Potsdam, den 05.01.2016

Published online at the
Institutional Repository of the University of Potsdam:
URN urn:nbn:de:kobv:517-opus4- 90271
http://nbn-resolving.de/urn:nbn:de:kobv:517-opus4- 90271

Contents

Preface

Statutory declaration

I hereby declare that this thesis is my own work, and that I acknowledged all sources and references used therein. I have not presented this thesis or their results to another university.

Eva-Maria Laux Berlin, January 3, 2016

Acknowledgment

The work described in this dissertation was conducted at the Fraunhofer Institute for Biomedical Engineering in Potsdam-Golm, which is now part of the Fraunhofer Institute for Cell Therapy and Immunology, Branch Bioanalytics and Bioprocesses.

My sincere thanks go to Professor Frank F. Bier for his continuous engagement for the institute despite organizational restructuring. Without his interest in my topic and the projects initiated by him, this dissertation would not have been possible.

Above all, I am grateful to Dr. Ralph Hölzel, not only for the excellent supervision of my doctoral thesis, but also for encouraging conference attendences, for sharing insight into peer-reviewing and grant proposal selection processes. The scientific brainstorming and the diverse discussions related to this work and beyond have made my time in his group instructional and enjoyable.

I heartily thank Xenia Knigge and Dr. Elena Ermilova for the pleasant and productive working atmosphere, for helpful discussions and advice. Furthermore, I thank Alexander Christmann for his instructions on the operation of the atomic force microscope, and Jörg Henkel for IT support.

Dr. Christian Wenger kindly provided the electrode chips that I needed for my experiments. I am thankful for the excellent collaboration, for efficient communication concerning electrode chip design and constitution, and for discussing possible applications. Besides, I thank Dr. Khoa Ly for Raman measurements.

Last but not least, I want to express my gratitude to my family and friends who have constantly supported me on my way.

Publications and presentations

This thesis presents data that was partially published in peer-reviewed journals or peer-reviewed conference proceedings. Some of the results were further presented at national and international conferences in the form of talks or posters.

Peer-reviewed journals

E.-M. Laux, X. Knigge, F. F. Bier, C. Wenger, R. Hölzel, Aligned immobilization of proteins using AC electric fields, *Small*, 2016, *12*, 1514.

E.-M. Laux, X. Knigge, F. F. Bier, C. Wenger, R. Hölzel, Quantification of dielectrophoretically immobilized proteins: Quantification by atomic force microscopy, *Electrophoresis* 2015, *36*, 2094.

E.-M. Laux, C. Wenger, F. F. Bier, R. Hölzel, Functionality of dielectrophoretically immobilized enzyme molecules, *Electrophoresis* 2014, *35*, 459.

Peer-reviewed conference proceedings

C. Wenger, X. Knigge, E.-M. Laux, F. F. Bier, R. Hölzel, Label-free immobilization of nano-particles on silicon based electrodes for single-biomolecule studies, *Proceedings of the International Conference on Biomedical Electronics and Devices* 2014, 176.

Conference presentations (talks)

E.-M. Laux, F. F. Bier, C. Wenger, R. Hölzel, Ausrichtung und Immobilisierung von Proteinen mit elektrischen Wechselfeldern. *Deutsches BioSensor Symposium* 2015, München.

R. Hölzel, X. Knigge, E.-M. Laux, U. Kaletta, S. Otto, S. Stanke, C. Wenger, F. F. Bier, Dielectrophoretic immobilisation of proteins and nanoparticles. *Dielectrophoresis* 2014, London.

R. Hölzel, C. Wenger, X. Knigge, E.-M. Laux, U. Kaletta, S. Otto, S. Stanke, F. F. Bier, Dielectrophoretic immobilisation of antibodies and enzymes on nanoelectrodes. *20th International symposium on electro- and liquid phase-separation techniques* 2013, Puerto de la Cruz.

Conference presentations (posters)

E.-M. Laux, F. F. Bier, C. Wenger, R. Hölzel, Aligned immobilization of proteins in AC electric fields. *European Biophysics Congress* 2015, Dresden.

E.-M. Laux, S. Otto, X. Knigge, C. Wenger, F. F. Bier, R. Hölzel, Dielectrophoretic immobilisation of proteins. *European Biophysics Congress* 2015, Dresden.

E.-M. Laux, C. Wenger, F. F. Bier, R. Hölzel, Functionality of dielectrophoretically immobilized enzyme molecules. *Dielectrophoresis* 2014, London.

E.-M. Laux and S. Otto, F. F. Bier, C. Wenger, R. Hölzel, Functionality of dielectrophoretically immobilized biomolecules. *NanoBioEurope* 2014, Münster.

X. Knigge, U. Kaletta, E.-M. Laux, F. F. Bier, C. Wenger, R. Hölzel, Dielectrophoretic immobilization of nanoobjects on silicon based electrodes for single-biomolecule studies. *NanoBioEurope* 2014, Münster.

R. Hölzel, C. Wenger, X. Knigge, E.-M. Laux, U. Ch. Kaletta, S. Otto, S. Stanke, F. F. Bier, Dielectrophoretic manipulation of biomolecules and nanoparticles. *NanoBioEurope* 2014, Münster.

E.-M. Laux, X. Knigge, U. Kaletta, F. F. Bier, Ch. Wenger, R. Hölzel, Positioning nanoparticles and proteins on nanoelectrodes arrays by dielectrophoresis. *20th International symposium on electro- and liquid phase-separation techniques* 2013, Puerto de la Cruz.

X. Knigge und E.-M. Laux, K. Nicklas, U. Kaletta, F. F. Bier, C. Wenger, R. Hölzel, Dielektrophoretische Immobilisierung von Nanopartikeln und Proteinen an Nanoelektroden. *Wissenschaftliches Symposium zur Eröffnung des Joint Lab Bioelectronics* 2013, Berlin.

E.-M. Laux and X. Knigge, U. Kaletta, F. F. Bier, C. Wenger, R. Hölzel, Dielectrophoretic immobilization of nanoparticles and proteins on nanoelectrodes. *NanoBioEurope* 2013, Toulouse.

R. Hölzel, C. Wenger, X. Knigge, E.-M. Laux, U. Ch. Kaletta, K. Nicklas, S. Otto, S. Stanke, F. F. Bier, Spatial manipulation of nanoparticles and biomolecules by AC electric fields. *NanoBioEurope* 2013, Toulouse.

X. Knigge und E. Laux, K. Nicklas, U. Kaletta, F. F. Bier, C. Wenger, R. Hölzel, Dielektrophoretische Immobilisierung von Nanopartikeln und Proteinen an Nanoelektroden. *Deutsches BioSensor Symposium* 2013, Wildau.

1 Introduction

1.1 Motivation and objective

Aging of the world's population leads to an increased number of people with some kind of diseases or injuries [1] that produce increased healthcare efforts and costs. Point-of-care testing and lab-on-a-chip devices are key words among the approaches to meet these challenges [2]. The ability to monitor health markers like blood pressure, cholesterol or glucose levels at home promises early detection of deteriorating conditions of chronically ill patients and a more personalized therapy. If genetic predispositions are known, diseases like cancer can be treated at an early stage with significantly higher healing probability [3] or, e.g. in the case of Alzheimer's, risk factors can be reduced to slow down the disease progression [4]. In some cases the disease outbreak might even be prevented. Above that, direct measurements of specific biomarkers can be vital for the diagnosis of myocardial infarctions [5] or pulmonary embolisms [6] that demand immediate analysis for successful treatment. This could be provided if the test results were obtained directly in the ambulance, and the clinic was able to prepare the necessary treatment.

Both point-of-care and portable devices profit from the steady miniaturization that has been taking place in the electronics industry for decades and is still progressing [7]. This tendency is promising not only for the handling of portable devices but also for the reduction of production costs [8]. The fabricated structures more and more approach the dimensions of molecules and offer the potential for manipulations on the nanoscale [9] down to molecular manipulation. Functional biomolecules are an essential part of numerous important bioanalytical devices. In biosensors for example, they are immobilized on the surface of a transducer. The sensing principle is based on the ability of the biomolecules to selectively bind or react with the analyte of interest. This selectivity results from a binding event at a specific active site of the biomolecule, rendering their accessibility decisive for the sensitivity of the device. Therefore, an oriented immobilization method is advantageous for improved sensitivity [10]. As a consequence, production costs can be reduced, as less reagents are consumed in the preparation of the device and during analysis.

There are numerous immobilization methods that lead to mostly statistical molecule orientations or that require elaborate procedures to achieve oriented immobilization [11]. There are also methods to orient molecules like desoxyribonucleid acid (DNA) by fluid flow or in electric fields, yet without immobilizing the molecules directly. In this thesis, a method that combines both aspects, immobilization and alignment, in a single-step experiment is developed. An electric field-assisted approach is chosen on the basis of the known accumulation of biomolecules at electrodes under the influence of inhomogeneous alternating current (AC) electric fields and on the existing studies

on particle alignment in electric fields.

The hypothesis for this dissertation was that proteins would be oriented in AC electric fields similar to the alignment of conducting and semiconducting nanowires [12] despite the lower conductivity and diverse shapes of proteins. For this, the method for biomolecule accumulation, dielectrophoresis, was to be extended for a simultaneous alignment and permanent immobilization of proteins. As there are only few research groups that apply molecular dielectrophoresis to proteins [13], general influence factors on the dielectrophoretic behavior had to be investigated. Furthermore, the functionality of the immobilized biomolecules had to be guaranteed in view of a potential incorporation of the electric immobilization method into biosensing devices. The aligned immobilization and the associated access to active sites of functional biomolecules would be a valuable contribution not only for bioanalytical applications but also for basic research on protein structure and interaction. This dissertation shows how to approach the above-mentioned problems using an electric field-assisted immobilization method. It reveals advantages of this method over existing immobilization techniques and also its limitations.

1.2 Literature review

1.2.1 AC electrokinetic effects

When AC electric fields are applied to a solution of molecules or to a suspension of particles, various electrokinetic effects arise, which depend on factors like the applied frequency and voltage, temperature, particle and medium characteristics. The hydrodynamic effects either act directly on the particles or lead to fluid flows that move the particles with them. The magnitudes of the various forces were estimated by Castellanos et al. [14] for model microelectrode systems and typical experimental parameters. The two effects that are relevant in the electrode configurations and under the experimental conditions used in this thesis are alternating current electroosmotic flow (AC EOF) and dielectrophoresis (DEP), which are explained in the following subsections.

AC electroosmotic flow

Electroosmosis is a well-known motion of the bulk fluid that arises in direct current (DC) systems. In an AC microelectrode system, a related fluid flow was described first in 1999 [15]. Likewise, AC EOF is based on induced charges in the electric double layer built on the surface of the electrodes: As the electrodes come into contact with a solution, the surface is charged and counterions are adsorbed on the surface. The

application of an external electric field induces Coulomb forces that act on the ions. Due to the higher field at the electrode edges, these areas are charged more quickly than areas farther away from the edges. As a consequence, the ions move, and they drag the fluid along the electrodes (Fig. 1.1). Since the electrode edges are always charged first, the direction of the fluid flow remains constant in spite of the repeated reversion of electrode polarity. This scenario is valid for intermediate frequencies that lie under the charge relaxation frequency, for at high frequencies reorientation of ions is too slow to follow the charge reversion. At lower frequencies, the potential drops across the double layer, and the remaining electric field in the bulk volume becomes small [16].

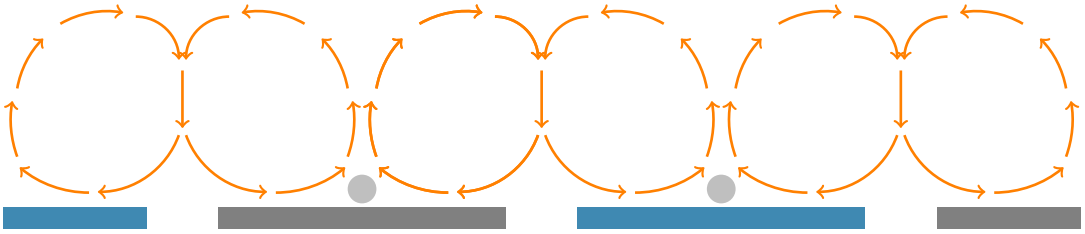

Figure 1.1: Fluid motion induced by alternating current electroosmotic flow over interdigitated electrodes (gray and blue).

Dielectrophoresis

The term "dielectrophoresis" was defined by Pohl [17] in 1951 as "The motion of suspensoid particles relative to that of the solvent resulting from polarization forces produced by an inhomogeneous electric field [...]". If a suspension of dielectric particles is brought into an electric field, charges within the particles are attracted to the oppositely charged electrode, and electric dipoles are induced in those particles. If the electric field is inhomogeneous, the field strength E is stronger on one side of the dipole (Fig. 1.2), resulting in the so-called dielectrophoretic force F_{DEP}, which acts on the particles in dependence on the particle radius r_{p} and of the relative permittivities ε_{x} of the particle (x = p) and the medium (x = m).

For spherical particles, the time-average dielectrophoretic force is given by equation (1.1) [18]. It is dependent on the particle radius r_{p}, on the relative permittivity of the medium ε_{m}, the real part of the Clausius-Mossotti factor Re[K(ω)], and on the electric field strength E. ε_0 is the permittivity of vacuum. The Clausius-Mossotti factor (Eq. (1.2)) depends on the complex permittivities $\varepsilon_{\mathrm{x}}^*$ of the particle (x = p) and of the medium (x = m). The complex permittivity (Eq. (1.3)) is a function of the real permittivity ε_{x}, of the conductivity σ_{x} and of the angular frequency ω. If the permittivity of the particle exceeds that of the suspension medium, the real part of the Clausius-Mossotti factor

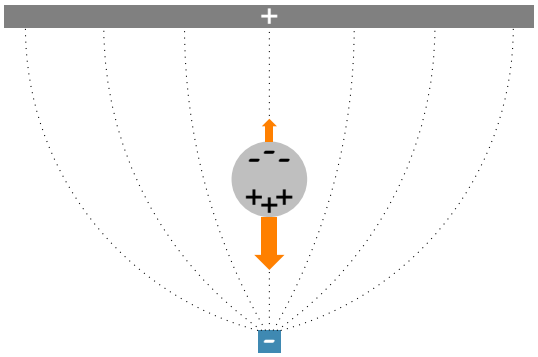

Figure 1.2: Dielectrophoretic force acting on an uncharged particle in the inhomogeneous electric field between two electrodes (gray and blue).

Re$[K(\omega)]$ will be > 0, and the particles will be attracted to regions of highest electric field (also termed positive DEP). *Vice versa*, Re$[K(\omega)]$ will be < 0 for particles with a lower permittivitiy compared to that of the suspension medium, and the particles will be repelled from high field regions (negative DEP).

$$F_{\mathrm{DEP}} = 2\pi r_{\mathrm{p}}^3 \varepsilon_0 \varepsilon_{\mathrm{m}} \mathrm{Re}\left[K(\omega)\right] \nabla |E|^2 \tag{1.1}$$

$$K(\omega) = (\varepsilon_{\mathrm{p}}^* - \varepsilon_{\mathrm{m}}^*)/(\varepsilon_{\mathrm{p}}^* + 2\varepsilon_{\mathrm{m}}^*) \tag{1.2}$$

$$\varepsilon_{\mathrm{x}}^*(\omega) = \varepsilon_{\mathrm{x}}\varepsilon_0 - i\sigma_{\mathrm{x}}/\omega \tag{1.3}$$

1.2.2 Molecular dielectrophoresis

DEP allows the non-destructive spatial manipulation of polarizable objects regardless of size or charge, and provides a great potential for bioanalysis and diagnostics. A lot of research has been conducted on cell concentration, trapping or sorting [19, 20, 21, 22]. Most cells have sizes between 1 µm to 100 µm and belong to the larger particles within the spectrum of dielectrophoretically manipulated objects. With the technological progress in nanostructure fabrication, the miniaturization of biomedical devices has proceeded, and the manipulation of smaller particles or even single molecules has become more and more important.

Within the field of biomedical applications, dielectrophoretic manipulations of DNA have been of particular interest. The molecular size of DNA was derived from the length of stretched DNA strands [23]. One end of the strand was attached non-specifically to an aluminum electrode in the electric field applied, while the other end extended perpendicular to the next electrode edge. In another experiment, a single DNA molecule was stretched between two electrically floating aluminum electrodes, and the DNA bridge remained even after switching off the DEP voltage [24]. In most studies, however, DNA was accumulated temporarily and diffused away after the electric field

had been switched off [23, 25, 26, 27]. This was also reported for ribonucleic acid (RNA) [28]. Sometimes modifications at the DNA, e.g. thiol-residues [29, 30, 31] or coupled avidin [32], were introduced for permanent attachment at the electrodes.

Defined structures can be built by self-assembly of specifically designed, complementary DNA strands with the most prominent example of so-called DNA origami [33]. The exact positioning of such constructs between the tips of electrodes was achieved using DEP [30]. Thus, patterns for the use in nanoelectronics can be built. The conductivities of defined-size DNA constructs were measured by impedance spectroscopy and found to be small enough for the structures to be incorporated into electronic devices without contributing significantly to the overall conductivity [31]. The extremely high level of precision even allows "molecular surgery" [34]. DNA was stretched dielectrophoretically between two floating electrodes. It was subsequently dissected by an enzyme that was bound on a latex particle and positioned at the DNA strand using optical tweezers. The comparison of two different enzymes that either cut the DNA at a random or at a specific site lead to mechanistic insight into the binding process of the restriction enzyme prior to cutting.

While these experiments on DNA were classified as molecular DEP, DNA is a biopolymer with a width of 2.5 nm and a variable length that often amounts to several micrometers when stretched, e.g. 16.5 µm for the lambda-DNA, which is used in a number of studies [23, 24, 34]. Mostly, however, DNA is found in a coiled conformation with not precisely defined shape. Even more important than shape is polarizability, which increases with the number of base pairs [35]. In contrast, proteins are much smaller, have defined structures and lower polarizabilities [36]. Since the dielectrophoretic force scales with the third power of the particle radius and additionally depends on the particle's polarizability (Eq. (1.1)), high electric fields or field gradients, respectively, are needed for dielectrophoretic manipulations. Therefore, proteins were not manipulated directly in some applications but bound to larger structures like microbeads [37, 38, 39]. The first direct protein DEP was demonstrated with the proteins avidin, concanavalin A, chymotrypsinogen A and ribonuclease A, which were attracted at electrodes under the influence of an AC electric field [40]. After switching off the field, the proteins diffused away. A similar reversible accumulation was observed for bovine serum albumin (BSA) [25], and for single R-phycoerythrin (RPE) molecules [41]. Furthermore, protein G and immunoglobulin G were concentrated at the tip of a nanopipette during field application [42]. Accumulation at the electrodes due to positive DEP and trapping in the electrode gap due to negative DEP was demonstrated with the example of avidin [43]. Trapping of BSA by negative DEP in dependence on the medium conductivity and pH and on the electric field strength was also achieved in an insulator-based setup

[44]. In a device with gaps in the nanometer range between insulating constrictions, streptavidin was preconcentrated [45].

At the time when this dissertation was started, there was only one report on permanent immobilization of proteins achieved by DEP: Above a certain voltage threshold, BSA was found to remain immobilized at pillar-structured, aluminum-coated electrodes [46].

Permanent immobilization of proteins like antibodies or enzymes is desirable since it is a crucial step in numerous bioassays. As a prerequisite for the proper use of proteins in such applications, their specific binding sites must remain intact. As the interaction with the surface might lead to changes in protein structure and activity [47], their binding capacity or enzymatic activity needs to be confirmed after immobilization. Among the very few reports that exist on the dielectrophoretic manipulation of enzymes, ribonuclease A was dielectrophoretically attracted to electrodes. However, its biofunctionality was not investigated [40]. The first proof of retained biofunctionality after dielectrophoretic immobilization was provided from our working group for anti-RPE antibodies that were still capable of binding RPE [48].

Insulator-based molecular dielectrophoresis

Among the examples given for molecular dielectrophoresis, there are two inherently different approaches to generate the field inhomogeneities needed for dielectrophoretic experiments: On the one hand, insulating obstacles or constrictions are introduced in an electric field. On the other hand, the inhomogeneity is produced solely by the electrodes.

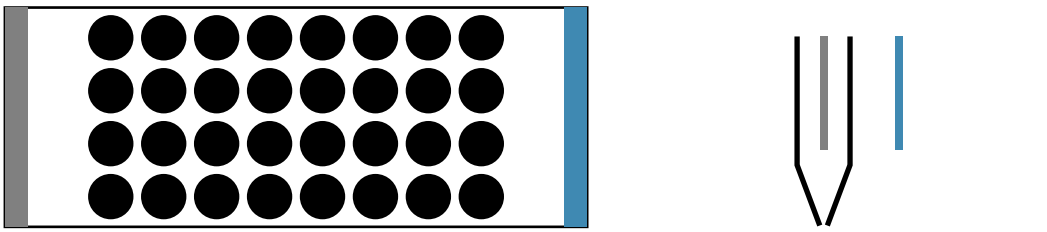

(a) Top view of insulating posts (black). **(b)** Side view of a nanopipette.

Figure 1.3: Schematic view of typical insulator-based DEP devices. Electrodes are depicted in gray and blue, respectively.

For insulator-based or electrodeless DEP, insulating posts (Fig. 1.3a) were mostly made of glass or polymer. With such a device, operated in continuous flow, BSA was trapped temporarily behind the posts by negative DEP in DC electric fields [44]. The influence of different post shapes was compared for immunoglobulin G and BSA, which were focused in stream lines within the device [49]. Constrictions were also introduced

through barriers in the channel [50], or a narrowing channel outlet. With the latter, the so-called "nanopipette" (Fig. 1.3b), trapping of DNA or protein molecules was achieved [42, 51].

The DC electric fields that are applied in the majority of insulator-based DEP experiments bring the disadvantage of DC effects like electrolysis of water, which occurs in dependence on the medium conductivity. The H_2 and O_2 bubbles that are formed at the electrodes replace water at the electrode edges, which leads to fluid motion interfering with dielectrophoretic attraction of the biomolecules. Thus, sometimes low-frequency AC electric fields were applied, or the electrodes were remotely placed to separate the location of bubble formation from the areas of biomolecule accumulation.

For the aims of this dissertation, another aspect of insulator-based DEP is even more significant. The trapping behavior of proteins in electrodeless devices is caused by negative DEP, which repells the proteins from the areas of highest field strength. Consequently, the proteins do not come into contact with the electrode surfaces and cannot be immobilized permanently.

Electrode-based molecular dielectrophoresis

Electrode-based DEP setups are prevalent for the manipulation of biomolecules [13]. Most electrode designs have planar configurations. Interdigitated electrodes (Fig. 1.4a) were used in a great number of experiments. Mostly DNA and RNA were accumulated along electrodes or stretched from one electrode to the next [52, 28]. Sometimes, field inhomogeneities were increased by additional corrogations [23]. Polynomial electrodes (Fig. 1.4b) were used to either collect avidin along the electrodes or to trap it in the electrode gap depending on the applied frequency [43]. In another polynomial electrode configuration, DNA and BSA were trapped between the adjacent areas of the electrodes by positive DEP, whereas negative DEP was not observed in the applied frequency range (50 kHz - 5 MHz) [25]. Nanostructured electrodes are particularly suited

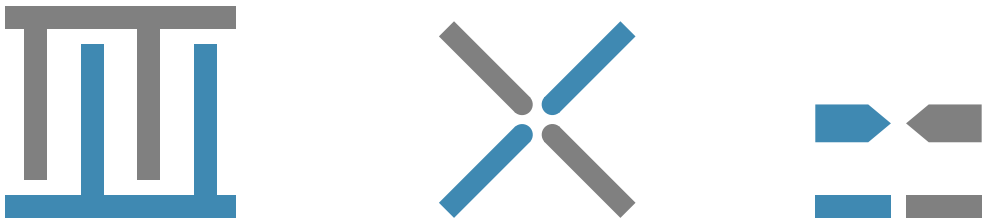

(a) Interdigitated electrodes. **(b)** Polynomial electrodes. **(c)** Electrode pairs.

Figure 1.4: Schematic top view of different types of electrodes used in DEP experiments.

to generate the necessary field gradients at lower voltages [53]. Furthermore, a re-

duction of Joule heating at the smaller electrode surface is desirable, as Joule heating was reported as the cause of protein denaturation and aggregation [49]. Only recently, opposing electrode pairs (Fig. 1.4c) with narrow gaps of below 10 nm were used to trap low numbers of RPE between the tips of titanium electrodes for surface enhanced raman spectroscopy (SERS) and conductance measurements [54]. The proof that even a single molecule can be trapped was also demonstrated with the example of RPE at the tips of sharp gold nanoelectrodes [41].

The first and only previous mention of a 3D electrode geometry with a regular array of pin-electrodes for molecular DEP involved nanopillars with a diameter of 50 nm and a distant counter electrode [46]. This electrode geometry was used for immobilization of BSA, which was reversible or permanent depending on the electric field strength. With insulator-based setups, permanent immobilization of biomolecules has not been reported and appears principally impossible.

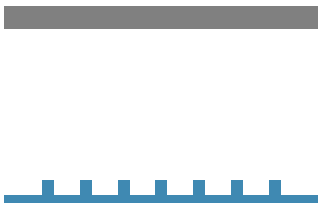

Figure 1.5: Schematic side view of a 3D electrode configuration consisting of a nanopillar array (blue) with one counter electrode (gray).

In cooperation with our partners at the Leibniz Institute for Innovative Microelectronics (IHP), 3D geometries with high-number electrode arrays and a distant counter electrode have been developed (Fig. 1.5) in our group, and successfully used for protein immobilization [48]. The 3D geometries, as opposed to planar geometries, offer the advantage of lower tangential field components and, hence, less fluid flows by AC EOF. In the meantime, the principle of this configuration has been adapted by other working groups for, e.g., BSA accumulation on gold nanocones [55].

1.2.3 Orientation methods

Orientation of molecules and small objects in electric fields

Theoretically, any molecule without spherical symmetry can be oriented or aligned in electric fields if the interaction energy with the electric field exceeds that of thermal rotation. As early as 1966, there were reports on experiments with oriented CH_3I molecules in a focused molecular beam with the purpose to study reactivity in depen-

dence on orientation. Orientation of molecules was achieved by the combined actions of an electric inhomogeneous hexapole field and a weak uniform field [56, 57]. There are further approaches, which mostly use intense polarized laser light for alignment [58] or combined fields to preselect molecules with specific rotational states followed by orientation in static electric fields [59, 60]. These methods are limited to vacuum conditions. A detailed review covering the existing techniques is given by Lemeshko et al. [61]. When applying just a single electric field, higher field strengths are required to orient molecules. Field strengths of $5.2\,\mathrm{MV\,m^{-1}}$ were used to orient adenine and cytosine at 0.37 K, and their IR vibrational transition moments were measured to determine their orientation relative to their permanent dipole moments [62]. Furthermore, oriented films of chloro-aluminum phthalocyanine were obtained by organic molecular deposition with applied field strengths of $14\,\mathrm{MV\,m^{-1}}$ [63]. Temporary alignment of a certain class of organic dyes was also achieved by the guest-host effect. The dyes (guests) were dissolved in liquid crystals (hosts) that form nematic phases upon application of DC electric fields [64, 65].

When working at room temperature, even higher field strengths are needed. The orientation of HCl molecules requires $28\,\mathrm{MV\,m^{-1}}$ in a rotationless state, whereas more than $1000\,\mathrm{MV\,m^{-1}}$ are needed at room temperature [56]. The application of DC electric fields of sufficient strength in an aqueous surrounding is limited by electrochemical effects like bubble formation due to electrolysis and production of ionic species and radicals. This can be avoided by employing AC electric fields.

Böhm et al. compared the use of DC and AC fields for the alignment of microtubules [66]. In DC fields (up to $2 \cdot 10^4\,\mathrm{V\,m^{-1}}$), microtubules were attracted to the electrode of opposite charge without preferred orientation. Higher field strengths could not be applied due to electrolysis and electrode polarization. In AC fields (200 kHz – 2 MHz, $10^5\,\mathrm{V\,m^{-1}}$), microtubule alignment was achieved. This comparison demonstrates the advantages of AC electric fields, which have been applied to a broad variety of objects on the micro- and nanoscale. In the micrometer range, elongated cells like Euglenoidina [67], yeasts [68, 69], llama erythrocytes [70] and bacteria [71] were oriented at MHz frequencies. Alignment of smaller objects was demonstrated for actin filaments [72, 73], virus particles [74] and DNA [23, 52, 75, 76]. In recent years, the controlled positioning of conducting and semiconducting nanowires has been of particular interest because of their potential use in electronic nanodevices [12, 77, 78, 79]. A review on these directed nanomaterial assemblies in non-uniform electric fields was published by Smith [80].

Whilst the aligned objects are termed "nano"-wires and "nano"-tubes, usually only their diameter is in the nanometer range, whereas their length often amounts to several

micrometers. As a result, these objects have high aspect ratios, which, in combination with the very good polarizability of the conducting materials along the long axes, facilitate alignment in electric fields. As opposed to that, proteins are molecules with diverse shapes and sizes that are in the range of nanometers in all three dimensions. Very early studies in the working group of Pörschke on electric dichroism of proteins in solution show a temporal alignment of proteins induced by short electric field pulses [81, 82, 83]. So far, however, this phenomenon has not been further investigated, nor has a permanent alignment in combination with immobilization by electric fields been reported for proteins.

Methods for oriented immobilization of proteins

Many bioanalytical applications involve protein immobilization steps. The majority of these immobilization procedures results in protein layers with a statistical distribution of protein orientations where only a fraction of the binding sites are actually accessible for analytes. As a result, antibody binding capacities or enzyme activities are decreased as compared to respective proteins in solution [84, 85]. In contrast, antibodies and antigen-binding fragments of antibodies (Fab fragments) that were immobilized with a specific orientation showed increased binding activities as compared to antibodies immobilized at random orientations [84]. In another study the activity of immobilized and specifically oriented sulfotransferases approached the activity of solution phase enzymes [85].

Distinct orientations of proteins can be achieved by physical or covalent methods if specific prerequisites are met. Physical immobilization methods lead to adherence of proteins to the substrate through van der Waals forces and hydrophobic or electrostatic interactions. On charged surfaces, enzymes with a distinct charge distribution prefer orientations where repulsive forces are minimized [86].

Covalent methods are based on the formation of bonds between particular sites of the protein, mostly amino acid residues, and the support. With multiple reaction sites present the degree of orientation decreases, and it is more probable that active sites are altered resulting in a reduced activity or binding ability. Ideally, there is only one residue that can be addressed individually, e.g., carbohydrate residues of glycoproteins [87] or the C- or N-termini [88]. Usually, these specific sites are chemically modified and subsequently bound to surfaces that need to be prepared adequately to be able to react with the introduced chemical modifications at the proteins. To name but a few examples, proteins were phosphorylated [89], coupled with biotin [84] or with polyhistidine tails [90] and bound to suitable supports. It is also possible to introduce these residues by site-directed mutagenesis [91, 92]. As most of these strategies need

adjustments for each protein according to its requirements, they are rather costly and time-consuming.

A detailed overview over the numerous and diverse strategies to achieve an oriented immobilization of proteins is given in reviews by Turkova et al. [10] and Rao et al. [11].

1.2.4 Investigation of oriented molecules

The orientation of elongated molecules or protein assemblies can be determined directly using microscopic techniques. With atomic force microscopy, for example, the substructure of myosin was studied, and a substructure with two heads and a tail of 155 nm length was displayed [93]. Furthermore, different types of DNA structures, e.g. linear, circular or supercoiled, could be visualized [94]. Thus, their orientation can be determined as well.

Despite the much higher spatial resolution of an atomic force microscope (AFM), which lies in the range of a few nanometers or even in the subnanometer range for the x/y-plane [95], optical microscopy is more common for orientational investigations, since it allows for real-time observations and is easier to handle. With darkfield microscopy [96] or differential interference contrast [66], the alignment in electric fields of microtubules with lengths up to 20 µm was monitored. The accumulation of fluorescently labeled microtubules and their alignment in AC electric fields was further studied by fluorescence microscopy [97]. Similarly, the orientation of actin filaments [72, 73] and of DNA [23, 52, 75, 76] was investigated using fluorescence labels attached to the filaments or DNA strands, respectively.

Fluorescence microscopy is the method of choice for most experiments, since the presence of several fluorescence labels at one molecule leads to a significant signal enhancement. Even more important is the development of detection techniques with resolutions of down to 20 nm in the x/y-plane, enabling single molecule detection [98]. In addition to the improved spatial localization, fluorescent molecules further offer approaches to gain orientational information. The emission of single fluorescence dye molecules was found to produce different intensity distributions depending on the orientations of their absorption and emission dipoles [99]. Such emission patterns can be matched to electrodynamic calculations of single-molecule emission in order to determine their orientations [100]. With this approach, the orientation and position of myosin V was determined from a series of slightly defocused fluorescence images, giving insight into the dynamic process of myosin V movement along actin filaments [101]. Instead of defocusing the fluorescence image, the dipole emission patterns of single molecules were also measured directly in the back focal plane of the microscope objective [102].

A further approach to determine molecule orientations, which is not dependent on the spatial resolution of single fluorophores, is based on polarized excitation and/or emission. Fluorophore interaction with light is characterized by absorption and emission transition dipole moments (TDMs), which are often parallel and can be assumed as identical [103]. The TDM direction indicates the polarization of the photons either absorbed at the transition from the ground state to the excited state or the photons emitted at the transition from the excited state to the ground state. As a result, the excitation efficiency of a fluorophore depends on the polarization of the excitation light, and likewise the polarization of the emitted light depends on the orientation of the fluorophore. This relationship was used to confirm the expected alignment of carbocyanine dyes with long hydrocarbon tails in membrane bilayers with their hydrocarbon chains parallel to those of the membrane bilayer phospholipids. A fluorescence polarization microscope with epi-illumination and high aperture objectives was used for this study [104]. Another class of dyes that can be incorporated into membranes are diphenylpolyenes. Their alignment in stretched polymers was studied by fluorescence polarization spectroscopy [105].

Changes of fluorescence spectra upon illumination with differently polarized light were also used to confirm the temporary alignment of organic dyes in liquid crystals by the guest-host effect [65]. Similarly, pleochroic dyes aligned in liquid crystals exhibited absorption spectra that depended on the polarization of the incident light [64]. The orientation of fluorescence dipoles in solid crystals was determined for pentacene in *p*-terphenyl at cryogenic temperatures from the fluorescence intensity variations in dependence on the polarization of the excitation light [106]. A transilluminating polarizing microscope was used to derive the orientation of the chromophores in Green Fluorescent Protein (GFP) crystals from fluorescence polarization measurements of the crystals [107].

Microscopic methods are of exceptional interest as they combine spatial and orientational investigations. With conventional setups, however, the polarization component along the microscope's optical axis is not accessible, and only polarizations in the plane of the microscope slide can be detected. For the determination of the three-dimensional orientation, a total internal reflection fluorescence (TIRF) setup is suited, where the excitation possesses a strong polarization component also in the z-axis [108].

Enhanced Green Fluorescent Protein for orientational studies

GFP is an intrinsically fluorescent protein that occurs naturally in the jellyfish *Aequorea victoria*. It consists of 238 amino acids, mostly in β-strand conformation, that form a barrel-like geometry with an aspect ratio of approximately 4:3. GFP has two

absorption maxima at 395 nm and 475 nm [109]. The chromophore is a relatively small part of the whole molecule structure. It lies the inside the barrel, and it is fixed in its position by covalent and hydrogen bonds. Therefore, the protein orientation can be deduced from the TDM of the chromophore alone.

One of the existing variants is the enhanced Green Fluorescent Protein (eGFP) (Fig. 1.6) with only two mutations (S65T and F64L) that lead to enhanced fluorescence properties and improved stability [110]. The orientation of its TDM relative to the chromophore structure was calculated by Ansbacher et al. [111]. Not only is this protein suited for orientational investigations on the basis of the TDM, its fluorescence further serves as an indicator for proper folding and integrity of the molecule, as the protein is only fluorescent in its native state. For these reasons, proteins of the GFP family are popular for the use as functional model proteins.

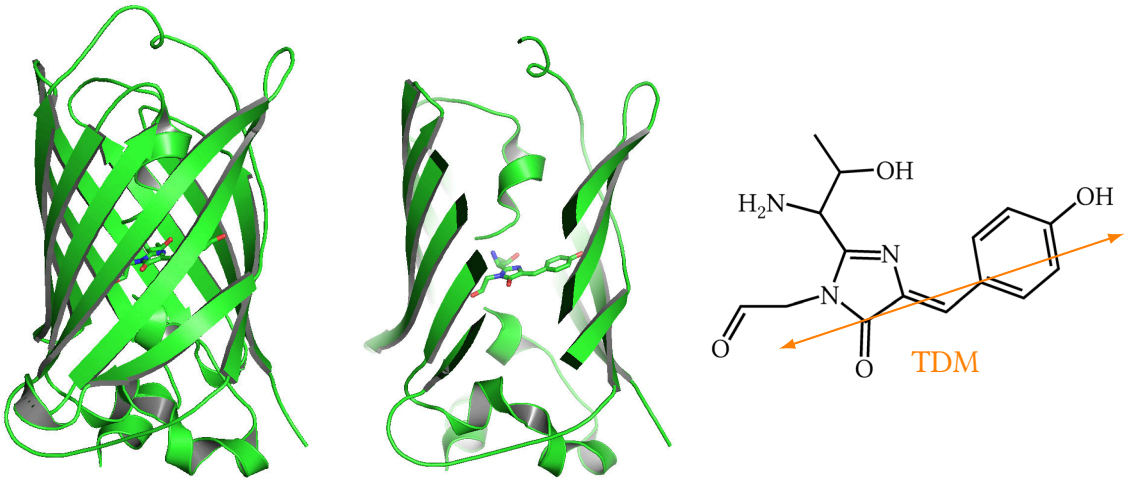

(a) Ribbon diagram, side view.

(b) Ribbon diagram, cut open to reveal the chromophore.

(c) Chromophore structure with the TDM.

Figure 1.6: eGFP molecular structure (PDB ID: 2y0g). The protein backbone is depicted as bands or thin tubes in the ribbon diagram, while the chromophore is given as structural formula with C: green, N: blue, O: red. The transition dipole moment (TDM) of the chromophore, which is responsible for interaction with light, is indicated by an orange arrow.

In one of the examples given for the determination of molecular orientation, GFP crystals with a diameter of approximately 1 µm and lengths up to several hundred micrometers were studied with a transilluminating polarizing microscope [107]. Configurations with polarized excitation, polarized emission, and the use of parallel or crossed polarizers for excitation and emission were employed while the microscope stage with the crystal was rotated. Fluorescence intensities were measured as functions of the stage's orientation angle for an individual crystal. This protocol, however,

is not readily adaptable to measurements of smaller regions of immobilized eGFP as the region of interest is difficult to be kept in the center of the field of view. An alternative would be to vary the polarizer orientation instead of rotating the stage, which has been done in measurements of single organic dye molecules [112]. With a similar approach, it should be possible to determine the orientation of homogeneously oriented fluorescent proteins.

1.2.5 Biosensors

Biosensors are bioanalytical devices that detect an analyte of interest. They make use of the specific interactions of a bioreceptor with the analyte and the thereby generated response (Fig. 1.7). This response is usually transduced into an electrical signal that represents the analyte concentration. Electrochemical transducers are most widely spread, but there are also optical, acoustic and calorimetric transducers [113, 114, 115]. The bioreceptors can be any kind of material that binds or reacts with the analyte of

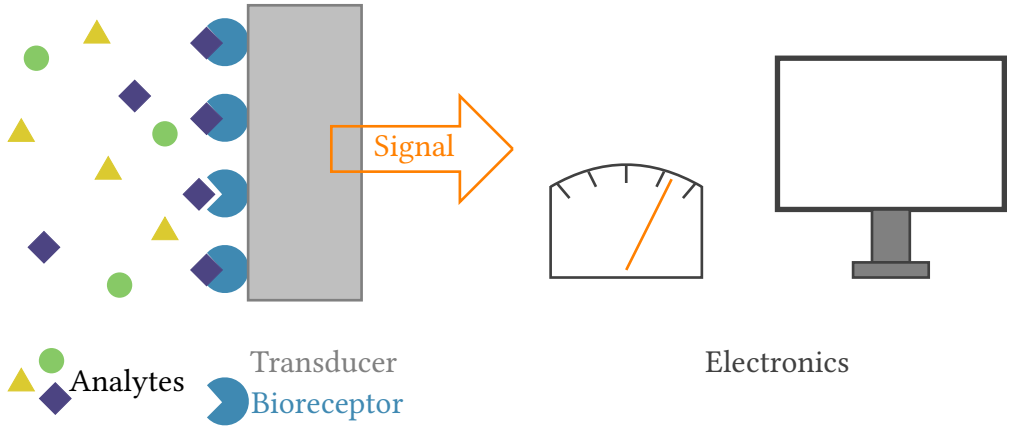

Figure 1.7: Working principle of a biosensor.

interest, e.g. tissues, microorganisms, cells or biomolecules like nucleic acids and proteins [116]. The diverse group of proteins includes receptors, antibodies and enzymes, which are prevalent in commercial biosensors [117]. The bioreceptors are connected to the transducer by covalent immobilization, by adsorption or inclusion [118]. It is possible that binding sites are modified or sterically shielded in the course of the immobilization step. For the functionality of a biosensor, however, the bioreceptors' ability to bind or react with the analyte is cruical. Therefore, the immobilization protocol has to be optimized for sensitivity and stability [116]. Elaborate immobilization methods have been developed to control the orientation of the bioreceptors and to assure free access of the binding sites [11].

Horseradish peroxidase in biosensors

Horseradish peroxidase (HRP) is an enzyme from the roots of horseradish with 308 amino acids [119]. It belongs to the class of oxidoreductases and catalyzes the electron transfer from an electron donor, which is oxidized, to an electron acceptor, which is reduced. More specifically, horseradish peroxidase (HRP) is a peroxidase. It oxidizes substrates in the presence of a peroxide, mostly H_2O_2, and it is relatively unspecific concerning the acceptance of substrates. HRP is soluble in distilled water and in dilute buffer, where it exhibits high activity at pH 6 - 8 in a temperature range of 20 °C to 45 °C [120]. Moreover, it can be purchased commercially at reasonable costs. These facts render it popular for numerous applications, which include the detection of, e.g., hydrogen peroxide [121], organic peroxides [122], phenols or aromatic amines [123]. The catalytic nature of the reaction produces a strong signal enhancement, which is beneficial for the detection of small amounts of analytes. For this reason, HRP is also employed as an indirect label. In Western blots or enzyme-linked immunosorbent assay (ELISA), for example, HRP is conjugated to antibodies that specifically bind the proteins of interest and enables detection by a luminescent reaction [124].

Luminol as a substrate for HRP

Among the broad variety of substrates for HRP, chromogenic or fluorogenic substrates are popular since they allow optical readout. Luminol is a substrate for HRP that can be oxidized in the presence of H_2O_2 [125]. The oxidation is a chemiluminescence reaction; the product 3-aminophthalate is formed in an excited state and relaxes with the emission of a photon (Fig. 1.8). However, the quantum yield of luminol in aque-

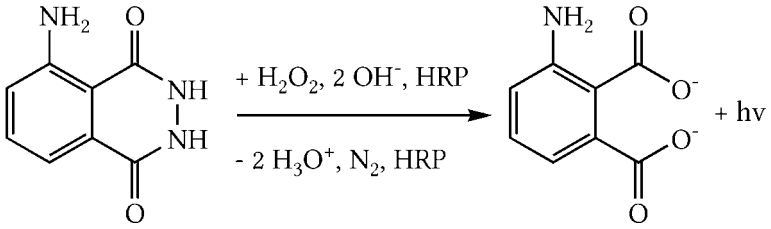

Figure 1.8: Horseradish peroxidase (HRP)-catalyzed oxidation of luminol to 3-aminophthalate.

ous solution is relatively low ($\phi = 0.0123$ [126]). Nevertheless, the appeal of using this substrate is the emission of photons precisely at the location of the reaction site so that the presence and activity of enzymes can be detected immediately. Moreover, there is no need of an excitation light source and, hence, no stray light. Thus, a high signal-to-noise ratio can be achieved, which is beneficial for sensitive measurements. The

luminol chemiluminescence reaction is the basis for a variety of quantitative applications [127]. Obviously, it can be used to detect H_2O_2 [128] or HRP, e.g. encapsulated in liposomes [129] or on a membrane [130]. The latter is useful for detection of HRP conjugates in Western blot assays.

Dihydrorhodamine 123 as a substrate for HRP

Precursors of fluorescence dyes like dihydrorhodamine 123 (DHR) can also serve as substrates for HRP. In the presence of H_2O_2, the fluorescence dye rhodamine 123 (Rh123) is formed (Fig. 1.9). Rh123 is a very bright dye that exhibits a high molar extinction coefficient at 500 nm of 78 780 L mol^{-1} cm^{-1} [131] and a high quantum yield of 0.90 [132]. Furthermore, the possibility for repeated excitation of the fluorescence dye is advantageous for the detection of enzyme activity, as higher emission intensities can be achieved by longer illumination of the sample. A major field of application for DHR is the indication of oxidative activity in cells [133].

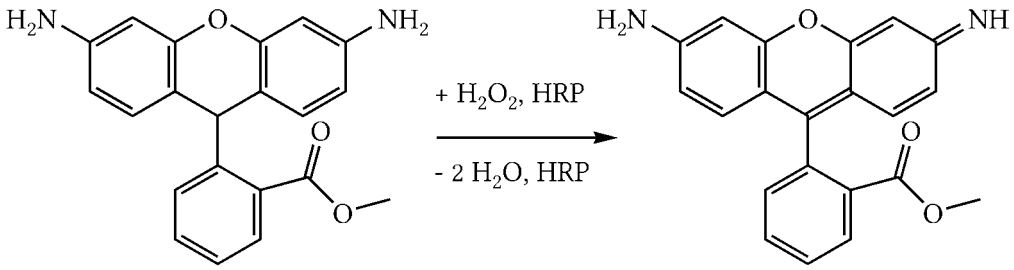

Figure 1.9: Horseradish peroxidase (HRP)-catalyzed oxidation of dihydrorhodamine 123 to rhodamine 123.

1.3 Scope of this thesis

From the literature review it is evident that there was not much known about molecular dielectrophoresis (DEP) of proteins and electrode-based DEP in particular at the beginning of this work. Only one report on permanent immobilization of bovine serum albumin (BSA) had been published. The permanent immobilization of proteins, however, is a prerequisite for the preparation of biosensing surfaces. Hence, general research is needed to understand the influence of experimental parameters on electrokinetic effects and the consequences for molecule motion, which is investigated in this thesis for different electrode geometries.

The existing studies on aligned immobilization by electric methods are limited to non-biological objects with high aspect-ratios and high conductivities. Molecular alignment is shown for DNA or protein filaments whose lengths often amount to several

micrometers, and immobilization is only achieved by chemical modifications on both the molecule and on the electrode. To date, there are no publications on the aligned immobilization of proteins with an electric field-assisted approach. The hypothesis that is investigated in this thesis is that the orientational effect in electric field applies also to proteins.

The number of existing methods for oriented immobilization of proteins demonstrates how desirable it is to gain control over protein orientation on surfaces, and that there is no universal method but rather very specialized approaches for different types of proteins. Specifically oriented proteins are of interest for interaction studies and for the use in bioanalytical applications like biosensors. The working principle of biosensors and also the role of horseradish peroxidase (HRP) in biosensors is described extensively in the literature and is not repeated in the literature review, as the details are not relevant to understand this thesis. What is important is a proof of concept that enzymes that are immobilized on electrodes by electric fields retain their catalytic activity. This aspect is addressed in this thesis with the example of HRP.

This thesis' objective is to gain insights into the field of molecular electrode-based DEP and to demonstrate how to use this method in bioanalytical applications.

2 Material and methods

2.1 Material

2.1.1 Chemicals

Ultrapure water with a conductivity < 1 µS cm^{-1} was used for all experiments. Chemicals were used as received.

Acridine orange	85 %, Sigma-Aldrich
2 µm beads (latex beads, carboxylate-modified polystyrene, red fluorescent)	Sigma
20 nm beads (FluoSpheres®, carboxylate-modified microspheres, red fluorescent)	Invitrogen
Bovine serum albumin (BSA)	> 98 %, Sigma-Aldrich
4-Cyano-4'-*n*-pentylbiphenyl	Alfa Aesar
Dihydrorhodamine 123 (DHR)	Cayman Chemical
Lambda-DNA	Fermentas
Enhanced Green Fluorescent Protein (eGFP)	BioVision
Ethanol	99.8 %, Roth
1-ethyl-3-(3-dimethylaminopropyl)carbodiimide (EDC)	> 98 %, Fluka
Gold-plating solution (Elektrolyt Gold)	Conrad
Hydrochloric acid	1 M, AppliChem
Hydrogen peroxide H_2O_2	30 %, Roth
N-hydroxysuccinimide (NHS)	> 97 %, Fluka
Mercaptoundecanoid acid (MUA)	95 %, Sigma-Aldrich
Peroxidase from horseradish (HRP), type VI-A, EC 1.11.1.7	Sigma-Aldrich
Oyster-555-TRP	Luminartis
Oyster-647-TRP	Luminartis
Phosphate buffered saline (PBS)	1 ×, AppliChem
PicoGreen (Quant-iT™ PicoGreen® dsDNA Reagent and Kits)	Molecular Probes
Silver paint, conducting	Conrad
Sodium hydroxide NaOH	Roth
Sodium bicarbonate $NaHCO_3$	Merck

Table 2.1: Chemicals.

2.1.2 Analytic devices

DC voltmeter	M9803R, Mastech
Demodulator probe	TT-DE112, Testec
Function generator	Model 193, Wavetek
Frequency counter	Voltcraft 7207, Conrad
Indium tin oxide coverslip	SPI Supplier (30-60 Ω)
Oscilloscope	HM307, Hameg
Power amplifier	TOE 7606, Toellner

Table 2.2: Electrical setup and components.

Atomic force microscope (AFM)	NanoWizard 3, JPK Instruments
AFM cantilever	OMCL-TR400PSA, Olympus
Scanning electron microscope (SEM)	Evo MA10, Zeiss
Energy dispersive X-ray spectroscopy (EDX) system	Quantas XFlash6 EDS System, Bruker
Fluorescence microscope	BX51, Olympus
CCD camera	Olympus F-View
Excitation filter ET 545/25	AHF Analysentechnik
Emission filter ET 605/70	AHF Analysentechnik
Beam splitter T 565 LPXR	AHF Analysentechnik
Excitation filter BP 460-495	Olympus
Emission filter BA 510-550	Olympus
Dichroic mirror DM505	Olympus
Mercury lamp	Osram HBO 103W/2
Objective 4 ×	UPLFLN, NA = 0.13, Olympus
Objective 10 ×	UPLFLN, NA = 0.30, Olympus
Objective 40 ×	UPLFLN, NA = 0.75, Olympus
Objective 60 ×	LUC Plan FL N, NA = 0.70, Olympus
Objective 100 ×	UPLFLN, NA = 1.3, Olympus
Wire grid polarizer	WP25L-UB, Thorlabs
Rotatable analyzer polarizer	U-AN360-3, Olympus
Confocal laser scanning microscope (CLSM)	Axiovert 100M, Zeiss
Fluorescence correlation spectroscopy (FCS) unit	ConfoCor 2, Zeiss
Objective 10 ×	Plan Neofluar, NA = 0.17, Zeiss
Objective 60 ×	LUC Plan FL N, NA = 0.70, Olympus
Nunc™ Lab-Tek™ Chambered Coverglass	155441, Thermo Scientific

Table 2.3: Microscopes and components.

Absorption (UV/VIS) Spectrophotometer	Specord200, Analytik Jena
Centrifuge	5415 D, Eppendorf
Concentrator	Vivaspin 500, Sartorius
Conductivity meter	LF Digi 550, WTW
Cuvettes	Fluorescence cell type 104F-OS, Hellma
Fluorescence spectrometer	LS55, Perkin Elmer
pH meter	761 Calimatic, Knick
Press (heatable, hydraulic)	LaboPress P 200 S, Vogt
Thermoshaker-incubator	Thriller, peqlab
Vortexer	Vortex-Genie 2, Scientific Industries

Table 2.4: Other devices.

2.1.3 Electrodes

With the exception of one type of interdigitated electrodes (IDE) taken from commercial surface acoustic wave (SAW) components, all electrode chips were produced at IHP in Frankfurt/Oder, Germany, in a standard 0.25 µm complementary metal-oxide-semiconductor (CMOS) process on 8 inch silicon wafers. The protocol comprised several photolithographic patterning, etching and polishing steps.

Tungsten cylinder electrodes

One type of electrodes used for dielectrophoretic protein immobilization were tungsten cylinder electrodes that were arranged in a square array on a chip with dimensions of 1 cm × 1 cm. The electrode array was subdivided into four square subarrays (Fig. 2.1a). Each subarray could be excited separately, and it contained 6256 electrode pins that were set on one potential. 16 cross-shaped areas were formed by omitting electrodes to allow a better identification of individual electrodes. The electrodes were prepared by filling cylindrical holes etched in the silicon dioxide SiO_2 with tungsten. The electrodes were 900 nm thick, and they had a diameter of about 500 nm and gaps of 2 µm to the nearest neighboring electrodes. The surface was polished to result in a nearly flat surface. Due to the different erosion rates of tungsten and SiO_2 the tungsten electrodes were slightly recessed and lay approximately 30 nm deeper than the surrounding SiO_2 as determined by atomic force microscopy. The electrical contact between the electrodes of each subarray was provided by an underlying metal layer made of Ti/TiN/AlCu/TiN/Ti (Fig. 2.1b). The metal layers of all four subarrays lead further to connection pads on the surface of the chip.

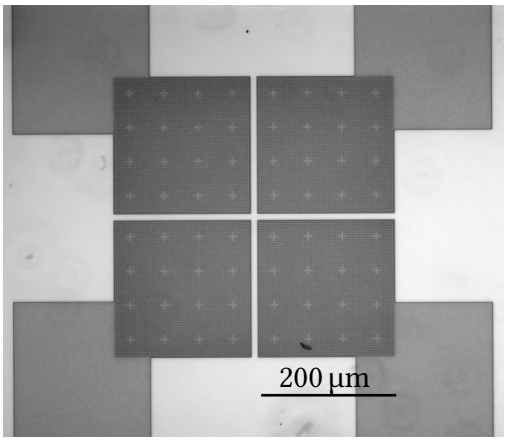

(a) Incident light micrograph of all four subarrays.

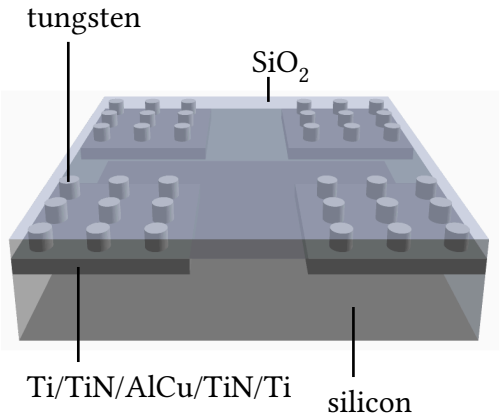

(b) 3D scheme of the material composition; parts of all four subarrays are displayed.

Figure 2.1: Arrangement and composition of a chip with tungsten cylinder electrodes.

Titanium nitride ring electrodes

A further, similar electrode design was used for dielectrophoretic immobilization of proteins. Here, the nanoelectrodes were again arranged in a square array that was divided into four subarrays. In contrast to the previously described electrode design,

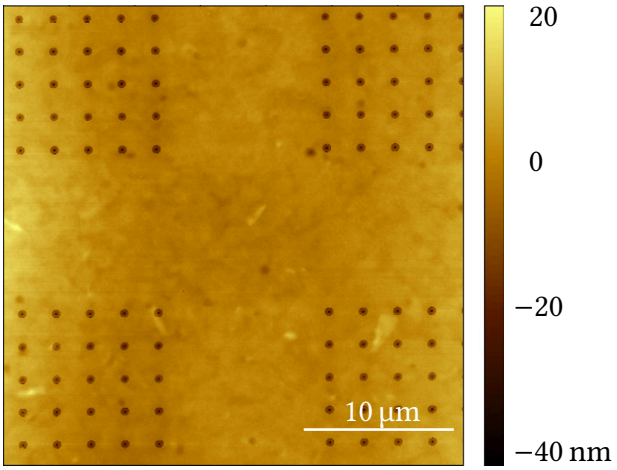

(a) Section with parts of all four subarrays.

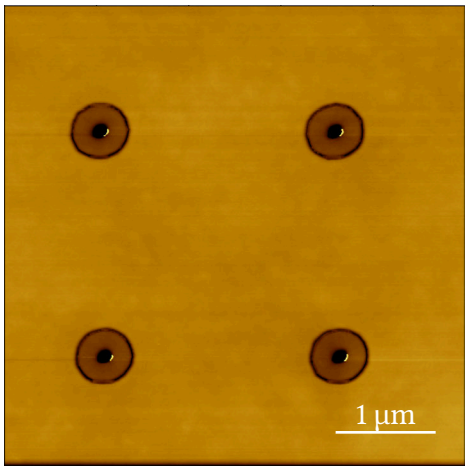

(b) Magnified section of four TiN electrodes.

Figure 2.2: Titanium nitride ring electrodes; AFM height images.

all subarrays were connected to each other by an underlying metal layer made of Ti/TiN/AlCu/TiN/Ti. Cylindrical holes with a diameter of 500 nm were etched into the SiO_2 and coated with a 20 nm thick layer of titanium nitride. Subsequently, the holes were filled with SiO_2. After the last grinding step, elevated titanium nitride rings with a thickness of approximately 20 nm remained on the surface. AFM measurements

(Fig. 2.2) revealed a recess of the internal surface by 10 nm to 15 nm in relation to the external surface. In the center of the rings there was an additional hole that results from incomplete filling of the hollow cylinders with SiO_2. The depth of these holes varied on the chips that were examined from 30 nm to 150 nm.

Interdigitated tungsten electrodes

Interdigitated tungsten electrodes (IDE) were used for the aligned immobilization of proteins. Two pairs of IDE were fabricated on a chip that had dimensions of 1 cm × 1 cm (Fig. 2.3a,c). Each electrode comb comprised 15 electrode fingers of 30 µm length. The

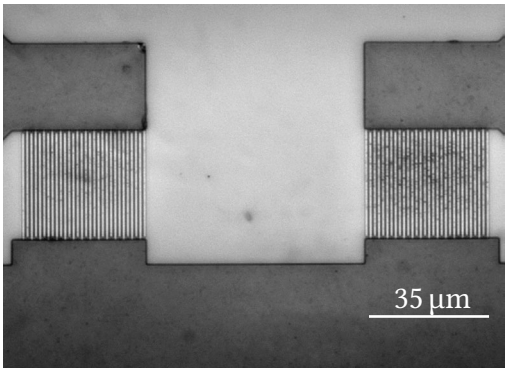

(a) Chip with two pairs of IDE; incident light micrograph.

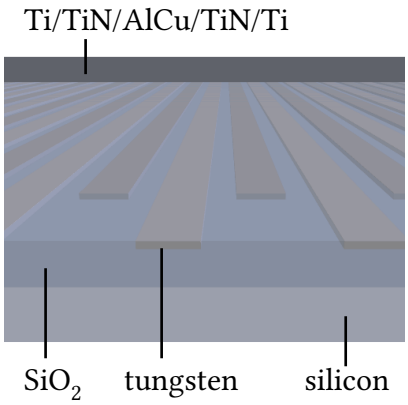

(b) 3D scheme of the material composition; cross section along one electrode basis.

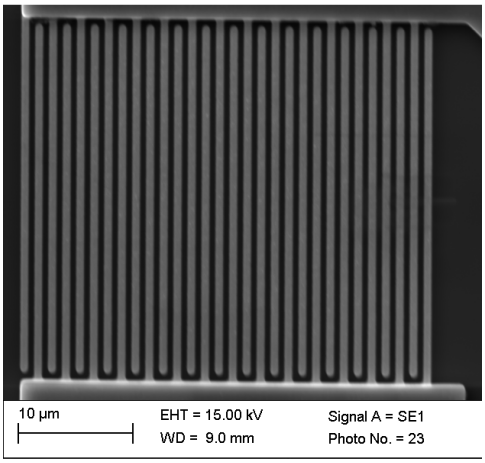

(c) One pair of IDE; SEM micrograph.

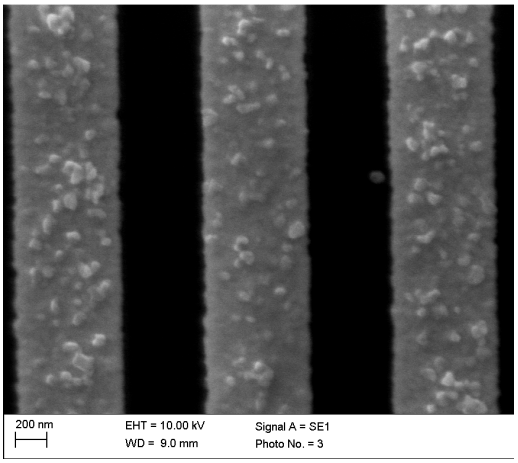

(d) Morphology of the electrode surface; SEM micrograph.

Figure 2.3: Arrangement and composition of interdigitated tungsten electrodes.

electrodes had a thickness of 100 nm, and they were embedded in SiO_2 (Fig. 2.3b). The electrical connection was provided by conducting Ti/TiN/AlCu/TiN/Ti metal layers leading to connection pads. The final chemical and mechanical polishing step re-

sulted in a surface, which was 10 nm deeper than the surrounding SiO_2 as determined by AFM measurements. Electrode bands and gaps were 750 nm and 450 nm wide, respectively. According to SEM measurements combined with energy dispersive X-ray spectroscopy (EDX) analysis, the surface of the tungsten electrodes was covered by a thin layer of tungsten oxide. This oxide layer lead to a roughness of the surface with structures that amounted to heights of 30 nm to 50 nm and whose diameters were in the range of 30 nm to 100 nm (Fig. 2.3d).

Interdigitated aluminum electrodes

Aluminum IDE were prepared from commercial SAW components (X 6964 M, Epcos). Two electrode combs were placed on a quartz substrate; they had 8 or 9 fingers, respectively (Fig. 2.4). The electrode fingers had widths of 22.6 µm and gaps of 22.2 µm.

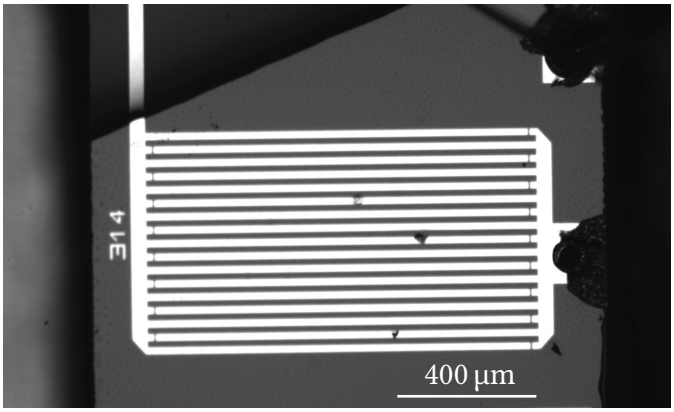

Figure 2.4: Interdigitated aluminum electrodes.

2.2 Methods

2.2.1 Epifluorescence microscopy

Microscope setup

An upright fluorescence microscope was used for imaging of experiments. The microscope was equipped with a cooled CCD camera. Images were acquired using different objectives with magnifications ranging from 4 × to 100 ×. For fluorescence micrographs, filters matching excitation and emission of the respective fluorophores were chosen. The samples were illuminated with either a tungsten-halogen light source or, for fluorescence excitation, a mercury arc light source. Illumination times up to 5 s were applied. For orientational investigations, the fluorescence microscope was equipped with an additional polarization filter, which was mounted in a self-manufac-

tured rotatable slider and inserted into the excitation beam. A wire grid polarizer with high transmission (> 83%) and high extinction rate (> 800:1) was employed.

Image acquisition and processing

Images were acquired using Olympus *Cell*^{M} 3.1, an imaging and analysis software, which controls the camera and shutters of the illumination system. Images were processed using *ImageJ*, a public domain Java image processing program, suited for microscopy evaluation.

2.2.2 Atomic force microscopy

AFM measurements

An atomic force microscope (AFM) was used for the detection and quantification of immobilized proteins. Imaging of dried chips was performed in contact mode in air. Cantilevers with a spring constant of $0.02\,\mathrm{N\,m^{-1}}$ and pyramidal silicon nitride tips with a nominal tip radius of 15 nm were used. Scanning rates between 0.4 Hz and 1.0 Hz and pixel resolutions of 512×512 or higher were employed.

Evaluation of AFM images

AFM images were processed with the scanning probe microscopy evaluation software *Gwyddion*. A possible tilt of the chip was compensated by the plane leveling function: Three points were selected to define a plane that is set to zero. Electrodes were selected with the *Gwyddion* grain analysis tool by either a threshold value (or – for electrodes with few proteins – by edge detection). Different parameters like heights, volumes, and areas of the grains were calculated using the program for further analysis, i.e. for the quantification of the amount of immobilized proteins.

2.2.3 Scanning electron microscopy

A scanning electron microscope (SEM) was employed to characterize the surface of tungsten nanoelectrodes and to visualize the differently grown gold structures of the gold-plated electrodes. The SEM was operated using the software *SmartSEM* (version 5.07). Acceleration voltages in the range between 5 kV to 15 kV and probe currents between 10 pA to 500 pA were applied for imaging. The working distance was set between 5 mm to 11 mm.

2.2.4 Energy dispersive X-ray spectroscopy

The elemental constitution of the materials contained in the electrode chips on and near the surface was determined by EDX analysis, especially after gold-plating. The combination with the SEM allowed for a spatial resolution of the measurements. 10 kV to 15 kV and probe currents up to 2 nA were applied to ensure an appropriate count rate (> 50 kcps). The working distance was kept between 9 mm and 10 mm.
Line scans or element maps were measured and evaluated using the software *Esprit 1.9*.

2.2.5 Labeling of proteins

Oyster dyes are fluorescent dyes, which are commercially available, that have been developed for fluorescent labeling of proteins. Here, tetrafluorophenyl (TFP)-functionalized reactive dyes were used that bind to free amino residues of the proteins (Fig. 2.5).

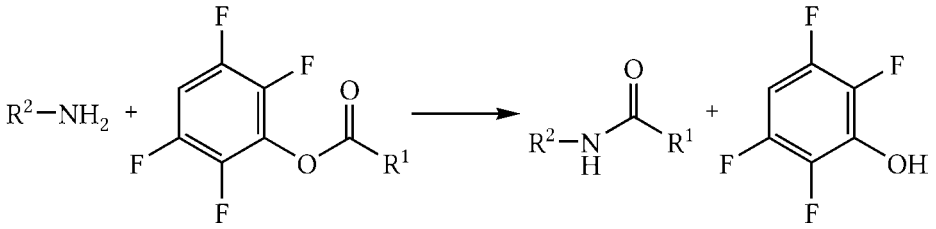

Figure 2.5: Covalent coupling of a fluorescent reactive dye to a protein. R^1 - fluorescence dye, R^2 - protein.

Fluorescence labeling protocol

The proteins BSA or HRP were dissolved in sodium bicarbonate buffer (100 mM, pH 8.5) to give a concentration of 5 mg mL^{-1}. The protein solution was added to the dry reactive fluorescent dye Oyster-647-TFP or Oyster-555-TFP, respectively, and complete dissolution was ensured by short vortexing. The reaction mixture was shaken continuously at 23 °C for 1 h with a thermoshaker-incubator at 300 rpm. Subsequently the reaction mixture was filled into two concentrators with 30 kDa molecular weight cutoff. The concentrators were centrifuged at 15 000 rcf for 5 min. The filtrates were removed, and the protein residues were redissolved in water. The centrifugation was repeated for 6 or 9 cycles, respectively, to remove unreacted dyes and to exchange the buffer against water. After the final centrifugation step, the proteins were diluted to a concentration of about 10 mg mL^{-1}. The exact concentration was checked by absorption spectroscopy. This stock solution was divided into aliquots of 10 µL, which were stored at −20 °C.

Absorption spectroscopy

Extinctions of protein and dye solutions were measured with an UV/VIS spectrophotometer at room temperature. Extinction was measured in 1 nm steps with integration times of 0.1 s. Cuvettes with a volume of 1400 µL and a light path of 10 mm were used. The baseline was recorded with a cuvette containing ultrapure water.

Density of labeling

Density of labeling (DOL) was determined according to the supplier's protocol. The absorbance A of the protein-dye conjugate was measured at 280 nm for the protein portion and at 552 nm for Oyster-555 or 651 nm for Oyster-647. With the molar extinction coefficients ϵ the concentration of fluorophores c_{Fluor} can be calculated (Eq. (2.1)).

$$c_{\text{Fluor}} = \frac{A_{552}}{\epsilon_{\text{Fluor}}} \tag{2.1}$$

$$c_{\text{Protein}} = \frac{A_{280} - (A_{552} \cdot C_{\text{f280}})}{\epsilon_{\text{Protein}}} \tag{2.2}$$

$$\text{DOL} = \frac{c_{\text{Fluor}}}{c_{\text{Protein}}} \tag{2.3}$$

For the calculation of the protein concentration c_{Protein} the fluorophores' contribution to the extinction at 280 nm has to be considered (Eq. (2.2)) using correction factors C_{f280} as provided by the supplier. The density of labeling (DOL) is defined as the ratio of the fluorophore and protein concentrations (Eq. (2.3)). The molar extinction coefficients for the proteins and the dyes, and the correction factors for the dyes are listed in Table 2.5.

	λ_{max} / nm	$\epsilon_{\lambda,\text{max}}$ / L mol^{-1} cm^{-1}	C_{f280}
HRP	280	37112	-
BSA	280	43824	-
Oyster-555	552	150000	0.06
Oyster-647	651	240000	0.04

Table 2.5: Molar extinction coefficients and correction factors for density of labeling determination.

2.2.6 Dielectrophoretic immobilization of proteins

Electrical setup

AC signals (sine wave) were generated by a function generator and amplified by a wide band amplifier (Fig. 2.6). Frequencies were controlled with a counter. Amplitudes were

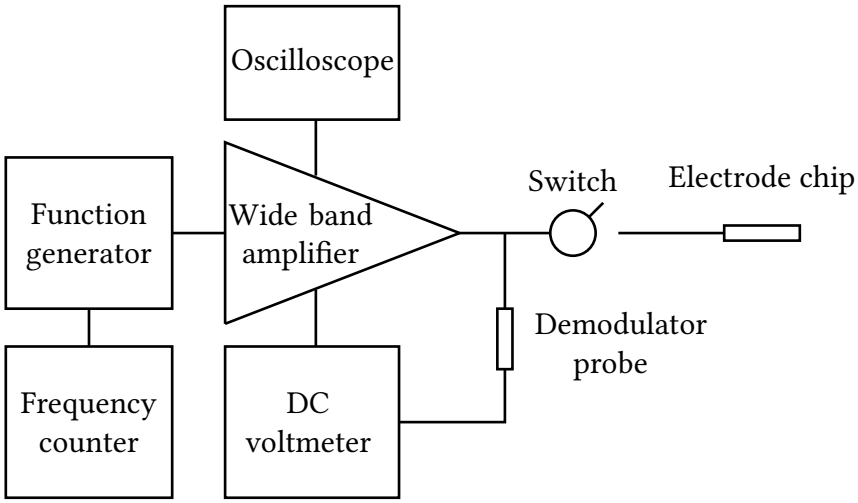

Figure 2.6: Scheme of the electrical setup for DEP experiments.

determined by a DC voltmeter equipped with a demodulator probe. The signal was additionally monitored with an oscilloscope. Connections were made by coaxial cables with the exception of a 10 cm flexible flat cable attached to the electrode chip that helped to avoid any unintended displacement of the electrodes. A 3.3 µF polycarbonate capacitor in series to the power amplifier output prevented any DC components reaching the electrodes.

Electrode preparation

Sample chambers were prepared from a laminating film that covered the chip surface with the exception of the electrodes (Fig. 2.7). The laminating film had a thickness of 0.1 mm. It further served as a spacer to separate the tungsten or titanium nitride nanoelectrode arrays from the counter electrode. The counter electrode, a conductive, transparent indium tin oxide (ITO) coverslip, was placed on the chip for immobilization experiments. The electric contact to the electrodes was provided by connection pads on the chip surface. Thin copper wires were attached by conducting silver paint

Figure 2.7: Tungsten cylinder electrode chip prepared for DEP. On this chip, all four subarrays were connected by conducting silver paint.

and soldered to the connector. Similarly, the counter electrode was connected by conducting silver paint. In the end, the electrode chip was fixed on a glass slide to facilitate its handling.

Protocol for dielectrophoretic immobilization

For DEP experiments the protein stock solutions were diluted with water to give concentrations of 0.1 mg mL^{-1} to 5 mg mL^{-1} (≈ 3 µM to 75 µM). A sample volume of 0.5 µL to 3.0 µL was pipetted into the sample chamber. The conductivity of the sample solution was estimated to be less than 10 µS cm^{-1} on the basis of conductivity measurements of larger volumes. AC signals (1 kHz to 1 MHz, < 37 V) were applied for a duration of few seconds up to 20 min to attract the proteins towards the electrodes. (Peak-to-peak values of voltages are given throughout the thesis.) Subsequently, the chip was rinsed with water to remove non-immobilized proteins and dried in a stream of nitrogen (Fig. 2.8).

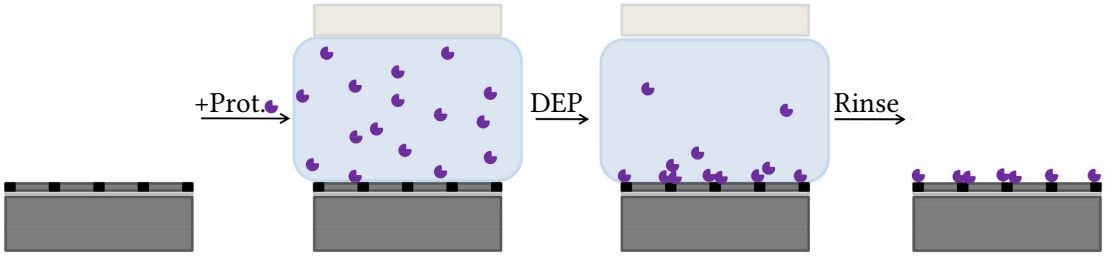

Figure 2.8: Scheme of the experimental procedure for dielectrophoretic immobilization of proteins at nanoelectrode arrays.

Conductivity measurements

Conductivities of buffer solutions were measured with a conductivity meter, which comprised a pair of platinum electrodes. For this, the solutions were filled into 1.5 mL Eppendorf tubes. Solutions with high buffer concentrations were measured at a frequency of 40 Hz, solutions without buffer or with low buffer concentrations were measured at 4 kHz.

2.2.7 Quantification of the amount of immobilized proteins

Dielectrophoretically immobilized proteins were quantified using two different approaches: Firstly, a relative quantification was done using fluorescence intensities of immobilized, fluorescently labeled proteins. For this purpose, three different programs were applied. Secondly, atomic force microscopy was used for an absolute quantification.

Relative quantification using fluorescence microscopy

a) Quantification using *ImageJ*

ImageJ (version: 1.43u), a microscopy image evaluation software [134], was used for the relative quantification of dielectrophoretically immobilized proteins. Circular regions of interest (ROIs) with fixed sizes were manually selected, and their mean intensity values were calculated by the measuring tool *ROI analyzer*. Only electrodes with fluorescence intensities above a certain threshold were considered for evaluation. The background (BG) was determined with ROIs of the same size and shape in the vicinity of the evaluated electrodes. The mean background intensity I_{BG} was subtracted from the mean fluorescence intensities I_{ROI} of the selected electrodes.

$$I = I_{\mathrm{ROI}} - I_{\mathrm{BG}} \tag{2.4}$$

The variation of sensitivities resulting from the use of different filter sets and of different illumination times for the measurement of either the enzyme label or of Rh123 was considered - if necessary - by dividing the background corrected intensities by the corresponding background (Eq. (2.5)). These average intensities I_{av} were used to compare the amounts of immobilized enzymes or of the reaction product Rh123 from different experiments.

$$I_{\mathrm{av}} = \frac{I_{\mathrm{ROI}} - I_{\mathrm{BG}}}{I_{\mathrm{BG}}} \tag{2.5}$$

b) Quantification using *GenePix Pro*

With *GenePix Pro* (version 3.0.5, Axon Instruments), a microarray acquisition and analysis software, fluorescent electrodes were automatically selected by defining a mask with a number of colums and rows that was laid over the fluorescence micrograph. The spot size was automatically fitted to the individual spots. The number of electrodes used for evaluation is only limited by the section covered by the fluorescence micrograph. Mean background intensities from regions around the electrodes I_{BG} and mean fluorescence intensities I_{ROI} were calculated automatically by the software. Again, background corrected average intensities I_{av} (Eq. (2.5)) were determined to account for different sensitivities and to allow a comparison of the fluorescence intensities.

c) Quantification using *Gwyddion*

The scanning probe microscopy evaluation software *Gwyddion* (version 2.28) [135] was used to detect fluorescence located at the electrodes and to determine the respective fluorescence intensities. First, the whole fluorescence micrograph was background

corrected by chosing three points in the image with background intensities. The plane defined by those three points was set as the background level with zero intensity. Fluorescent electrodes in the fluoresence micrograph were selected with the grain analysis tool. Since electrodes without immobilized proteins reflect light at the metal surface and lead to intensities exceeding those of electrodes with only few proteins, those bare electrodes had to be omitted by selecting a threshold value. The mean intensities of the selected electrodes were calculated by the grain analysis tool and used for further evaluation.

Absolute quantification using atomic force microscopy

The volumes of immobilized proteins located on the electrodes V_{AFM} were determined from the AFM height measurements with the program *Gwyddion* (see section 2.2.2). Volumes were calculated from the areas covered with proteins and the mean heights of the respective deposits. The recess of the electrodes in relation to the SiO_2 surface by approximately 30 nm was taken into account by adding this value to the heights used for volume calculation. Subsequently, a maximum number of proteins N_{max} contained in the actual protein deposit volumes was estimated on the basis of the protein crystal unit cell volume $V_{\mathrm{unit\ cell}}$ (Eq. (2.6)). According to the published crystal structure, the unit cell has dimensions of 21.56 nm × 4.51 nm × 14.24 nm [136]. From the monoclinic crystal form and the *C*2 space group follows a number of eight protein molecules contained in one unit cell.

$$N_{\mathrm{max}} = 8 \cdot \frac{V_{\mathrm{AFM}}}{V_{\mathrm{unit\ cell}}} \tag{2.6}$$

2.2.8 Investigation of enzyme activities

Monitoring of enzymatic reactions

An inverted confocal laser scanning microscope (CLSM) coupled with a fluorescence correlation spectroscopy (FCS) unit was used to monitor enzymatic reactions in solution. The sample was either contained in a chambered coverglass with a nominal volume of 400 µL or pipetted onto a microscope slide. The focus of the optics was set into the sample volume, and photon emission from the luminescent reaction was detected with the sensitive avalanche photodiode detector of the FCS unit. The count rate was monitored in intervals of 10 s to 30 s for a duration up to 100 min. Objectives with magnifications of 10 × or 60 × were used. Chemiluminescent reactions were detected without laser illumination. The formation of fluorescent products was monitored upon excitation with an argon ion laser at 514 nm and a maximum power of 300 µW in the

beam focus.

Enzymatic oxidation of dihydrorhodamine 123

DHR was dissolved in N_2-purged ethanol at a concentration of 12.6 mM. The stock solution was stored at −20 °C in the dark to prevent auto-oxidation, which was further checked by fluorescence spectroscopy. 30% hydrogen peroxide H_2O_2 was freshly diluted for experiments to 0.05% (14.7 mM) with water. For the enzymatic reaction, 1 µL of the DHR solution (12.6 nmol) and 1 µL H_2O_2 (14.7 nmol) were mixed in the sample chamber of an electrode chip with immobilized enzymes (Fig. 2.9). The chip was rinsed with water after less than five seconds incubation. Conversion of the non-fluorescent DHR to the fluorescent Rh123 was subsequently monitored by fluorescence microscopy.

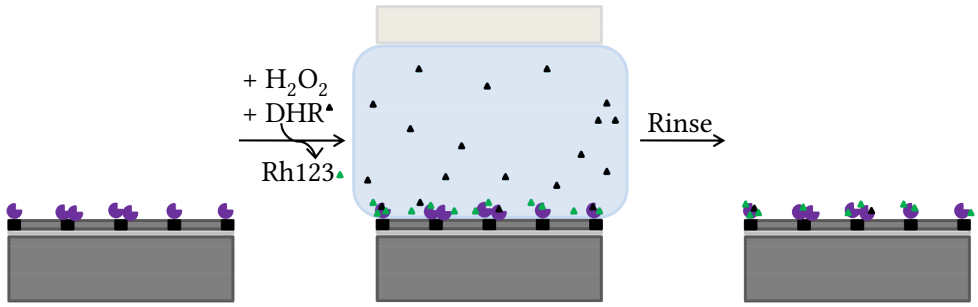

Figure 2.9: Scheme of the experimental procedure for enzymatic oxidation of dihydrorhodamine 123 (DHR) to rhodamine 123 (Rh123) by immobilized horseradish peroxidase.

Quantification of enzyme efficiency

The enzyme efficiency *EE* was calculated as the ratio of the amount of newly formed dye to the amount of immobilized enzymes (Eq. (2.7)). The amounts of the reaction product and of immobilized enzymes were determined using the fluorescence intensities of the fluorescent enzyme labels and the fluorescent reaction product, respectively (Eq. (2.5)). *GenePix Pro* was used to determine fluorescence intensities similarly to the relative quantification of immobilized proteins.

$$EE = \frac{I_{\text{av, Rh123}}}{I_{\text{av, HRP}}} \tag{2.7}$$

Fluorescence spectroscopy

Fluorescence spectra of Rh123 solutions were recorded with a fluorescence spectrometer at room temperature. A scan rate of 200 nm min^{-1} and monochromator slit

widths of 10 nm were chosen. Cuvettes with a volume of 1400 µL and a light path of 10 mm were used.

2.2.9 Molecular alignment

Alignment of acridine orange

Acridine orange was dissolved in denatured alcohol at a concentration of 27 nM. It was subsequently mixed with 4-cyano-4'-*n*-pentylbiphenyl in a ratio of 1:50 and filled in the sample chamber of an electrode chip with two opposing gold electrodes. The sample chamber was sealed with a coverslip, and AC voltages of 20 V to 37 V were applied to align the acridine orange molecules by the guest-host effect [137].

Alignment of DNA strands

Linear lambda-phage double-stranded desoxyribonucleic acid (dsDNA) with 48502 base pairs and a molecular weight of 31.5 MDa, dissolved in buffer (10 mM Tris-HCl, pH = 7.6, 1 mM EDTA) at a concentration of 0.3 µg µL^{-1} was diluted with water in a ratio of 1:200. The DNA amounts to a contour length of approximately 16 µm. The dsDNA was stained with a solution of PicoGreen (DMSO, concentration not provided by the supplier, diluted with water 1:200) by mixing the solutions in a ratio of 1:1. The stained DNA was pipetted into the sample chamber of an IDE chip, and AC signals (> 1 MHz, > 25 V) were applied to align the DNA strands between the electrodes.

Aligned immobilization of eGFP

eGFP was dissolved in water to give a concentration of 1 mg mL^{-1} (30.6 µM). The stock solution was divided into aliquots of 10 µL and stored at −20 °C. For immobilization experiments, an aliquot of the eGFP stock solution was thawed and diluted with water to a concentration of 0.35 mg mL^{-1}. A volume of between 0.5 µL and 2 µL eGFP solution was pipetted into the sample chamber. A transparent coverslip was put on the sample chamber to seal the chamber and to reduce evaporation. Protein movement was imaged by fluorescence microscopy. An AC electric field (frequency range 100 kHz – 1 MHz, voltages up to 37 V) was applied for 1 min to 5 min to immobilize proteins at the IDE. After switching off the field, the chip was rinsed with water to remove non-immobilized proteins and dried in a stream of nitrogen.

2.2.10 Orientational investigations

Experimental setup

Chromophore orientations were investigated with a fluorescence microscope that was equipped with rotatable polarizers. The polarizers were inserted into either the excitation light beam or the emission light beam or both (Fig. 2.10a). Fluorescence intensities were determined from fluorescence micrographs using *ImageJ*. The different polarizer configurations were compared using uncorrected fluorescence intensities.

For the setup with one excitation polarizer, data acquisition and evaluation was refined: The samples were excited with polarized light, and their fluorescence intensities were measured by acquiring fluorescence micrographs. The excitation polarizer was rotated in 22.5°-steps with a variation of the polarization angle α over 360° or more (Fig. 2.10b), and fluorescence intensity images were acquired for each polarizer position. Subsequently, the electrode chip was rotated and fixed in the new chip orientation β. Again, the excitation polarizer was rotated in 22.5°-steps, and a new data set of fluorescence micrographs was acquired. This procedure was repeated for several chip orientations. The chip orientation with the electrode fingers oriented vertical in the image will be referred to as "0°" throughout the dissertation.

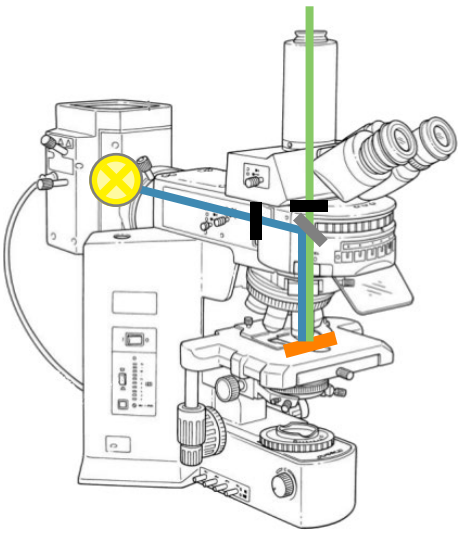

(a) Fluorescence microscope[1] with two polarizer slots for excitation and emission (black).

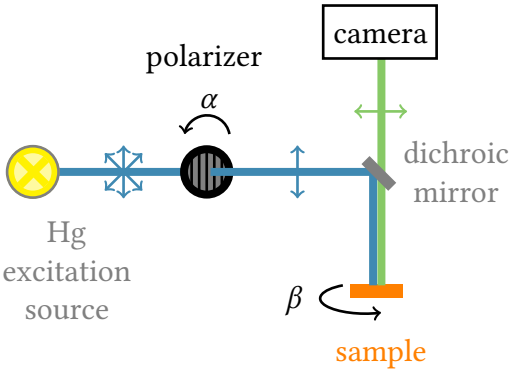

(b) Light path for fluorescence measurements with an excitation polarizer. Polarizer orientation α and sample orientation β are varied stepwise.

Figure 2.10: Experimental setup for orientational investigations with its light path (blue = excitation, green = emission). Double-headed arrows indicate the plane of polarization.

[1]Image source: Olympus BX51 manual, modified.

Data correction of polarized light fluorescence intensities

Dichroic mirrors or filters are employed in fluorescence microscopes to selectively reflect or transmit light of certain wavelengths. The transmission efficiency of these filters depends not only on the wavelength but also on the incident angle and on the polarization of the incoming light [138]. This characteristic of the dichroic mirror leads to polarizing effects of the optical setup that have to be taken into account for a quantitative determination of fluorescence polarization [139]. Therefore, measured data were corrected with reference data from statistically oriented samples.
For this purpose, a solution of fluorescent proteins was chosen. The intensity modulation obtained in response to changes of the excitation polarizer orientation by this reference sample was assigned to the optical properties of the system [138]. For further influence factors on the measured intensities, the following assumptions were made: The intensity of the light source I_{Hg} and transmission efficiencies of excitation and emission filters t_{ex} and t_{em}, respectively, is constant for given wavelengths and independent of the polarization. The transmission t_α of dichroic mirrors for given wavelengths is dependent on the polarization orientation α and, as a consequence, so is the excitation intensity $I_{\mathrm{ex}}(\alpha) = t_{\mathrm{ex}} \cdot t_\alpha \cdot I_{\mathrm{Hg}}$. Scattered light from components of the optical pathway or the sample is blocked by the filters and can be neglected here. As images were acquired in darkness, residual light can also be neglected. A constant background a_{fix} is caused by dark current and camera noise. It was determined experimentally from dark frames (shutter closed, acquisition time according to respective data collection). The software *ImageJ* was used to select ROIs within the images. The plugin *ROI manager* was used to determine mean intensities of ROIs for further evaluation. The mean intensities $I_{\mathrm{ref}}(\alpha)$ measured with the reference protein solution were background corrected and used to correct fluorescence intensities from unknown samples.

Evaluation of data from polarized light fluorescence microscopy

The mean fluorescence intensities $I_{\mathrm{m}}(\alpha)$ measured from unknown samples were corrected with reference data $I_{\mathrm{ref}}(\alpha)$ with consideration of a constant background a_{fix} (Eq. (2.8)).

$$I(\alpha) = \frac{I_{\mathrm{m}}(\alpha) - a_{\mathrm{fix}}}{I_{\mathrm{ref}}(\alpha) - a_{\mathrm{fix}}} \tag{2.8}$$

For the case of an oriented sample, the corrected intensity $I(\alpha)$ is expected to show periodic variations as a function of the polarization orientation α of the excitation light.

This periodicity can be described by a $\sin^2$ function of the general form (Eq. (2.9))

$$I_{\text{per}}(\alpha) = I_{\text{av}} + A_0 \cdot \sin(\alpha - \rho)^2 \tag{2.9}$$

with an average intensity I_{av}, the amplitude A_0 representing the amplitude of intensity variation, and a phase offset ρ. This equation was used for the simplest cases of orientational investigations, where no overall intensity decrease due to fluorescence bleaching was observed. If necessary, however, bleaching was taken into account by, e.g., a linear approximation (Eq. (2.10)) to the data. As an alternative to a linear approximation, bleaching can be accounted for more precisely by assuming a monoexponential decay (Eq. (2.11)) for the fluorescence intensity. I_0 is the fluorescence intensity of an unbleached sample, b or d are the linear or exponential decay constant, respectively, and I_∞ is the residual background intensity of the bleached sample.

Bleaching is dependent on the duration of illumination and, hence, the number of micrographs acquired. As a fluorescence micrograph is taken for each polarizer position, bleaching is indirectly a function of the polarizer orientation. If the sample is not or only very shortly illuminated between the acquisition of fluorescence micrographs or between reorientation of the chip, a continuous fluorescence decrease is observable extending several data sets.

$$I_{\text{bleach},1}(\alpha) = I_0 + b \cdot \alpha \tag{2.10}$$

$$I_{\text{bleach},2}(\alpha) = I_0 \cdot \exp(-\alpha/d) + I_\infty \tag{2.11}$$

$$I(\alpha) = I_{\text{bleach},2}(\alpha) \cdot I_{\text{per}}(\alpha) \tag{2.12}$$

$$I(\alpha) = (I_0 \cdot \exp(-\alpha/d) + I_\infty) \cdot (I_{\text{av}} + A_0 \cdot \sin(\alpha - \rho))^2 \tag{2.13}$$

In the course of the following fitting procedure, the exponential function's parameters I_0, d and I_∞ were included in the $\sin^2$ fit function Eq. (2.13) and allowed to vary just within the interval given by their standard deviations resulting from the initial exponential fit. All functions were fitted to corrected data using Origin (OriginPro 8G), a data analysis and graphing software.

2.2.11 Electroplating

Experimental setup

The electrodes were electrically connected to a DC voltage source using a conducting rubber pad and a brass plate held in place by an alligator clip. The sample chamber was formed by a silicon sealing ring enclosing the electrode array. The anode, a gold-plated copper wire, was placed on the sealing ring and positioned over the electrode

array so that it would later be in contact with the gold-plating solution. The gold-plating solution contained 2-3% $K_4Fe(CN)_6$, 1% $H[AuCl_4]$ and 2-3% $(NH_4)_2CO_3$.

Protocol for electrolytic gold-plating

For gold-plating of tungsten cylinder electrodes, DC voltages in the range of 1.0 V to 3.0 V were applied, and 10 µL gold plating solution were added immediately. After a duration of 30 s to 30 min the gold plating solution was removed with a pipette, and subsequently the voltage was turned off. The electrode chip was rinsed with water and dried in a stream of nitrogen. If the electrode chips were pre-cleaned with isopropanol, ethanol or 10 % hydrochloric acid, the chip was incubated with 5 µL to 10 µL of the solvent for 3 min. It was subsequently rinsed with ethanol and dried in a stream of nitrogen. Annealing was performed in a heatable, hydraulic press (the press-function was not used) *in vacuo* (50 mbar) at 300 °C for 30 min.

Calculation of current densities

Current densities J were calculated from from the measured electric current I and the electrode surface area A_{ele} (Eq. (2.14)). The electrode surface area A_{ele} depends on the number of connected subarrays $N_{sub} \in \{1; 2; 3; 4\}$, the number of electrodes contained in one subarray $N_{ele} = 6256$, and the electrode radius $r_{ele} = 250\,nm$ (Eq. (2.15)).

$$J = \frac{I}{A_{ele}} \tag{2.14}$$

$$A_{ele} = \pi \cdot r_{ele}^2 \cdot N_{ele} \cdot N_{sub} \tag{2.15}$$

2.2.12 Covalent immobilization of proteins

Gold-plated electrodes were incubated in mercapto undecanoic acid (MUA) (5 mM) for > 48 h to allow arrangement of mercapto undecanoic acid (MUA) molecules on the gold surface and the formation of Au-S bonds (Fig. 2.11). The carboxyl groups of MUA were activated by a mixture of 1-ethyl-3-(3-dimethylaminopropyl)carbodiimide (EDC) (0.4 M) and *N*-hydroxysuccinimide (NHS) (0.1 M) in a ratio of 1:1 for 10 min. Subsequently, a solution of the protein was added for immobilization (10 mg mL^{-1}). After 10 min incubation with the proteins, the chip was rinsed with water.

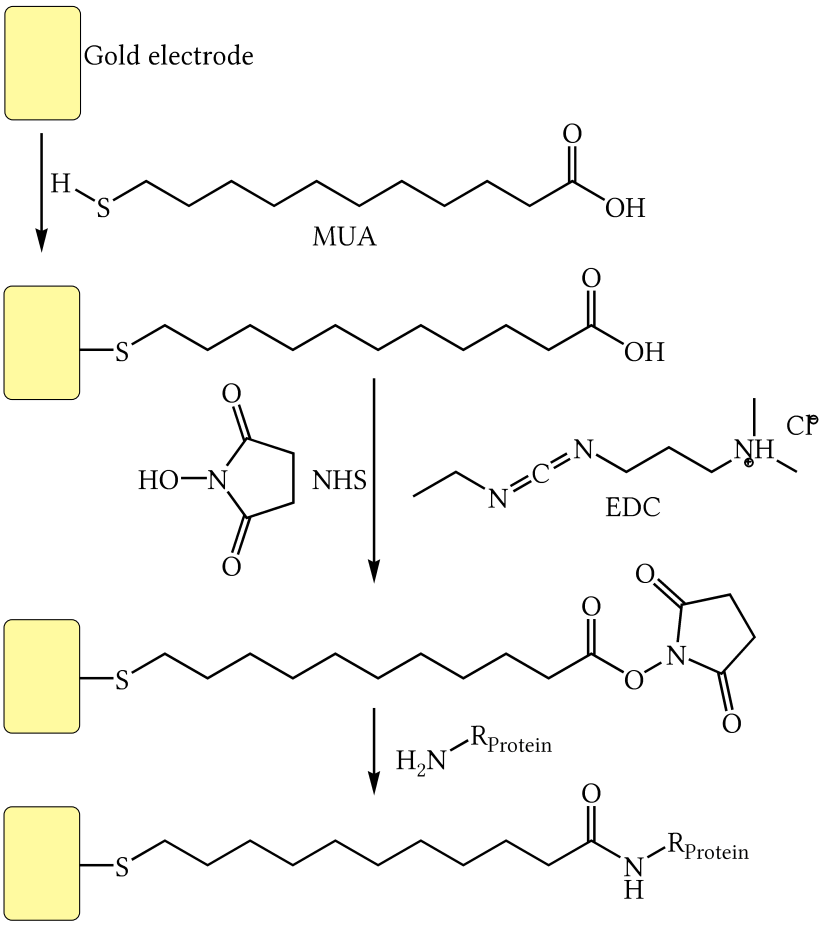

Figure 2.11: Reaction scheme of covalent attachment of a protein to a MUA-modified gold electrode using NHS/EDC activation.

2.2.13 Raman spectroscopy

Raman spectra were measured by Dr. Khoa Ly, AG Weidinger, TU Berlin. A confocal Raman spectrometer (LabRam HR-800, Jobin Yvon) was used with a krypton ion laser as excitation source (413 nm, 5 mW). A 25 x objective with numerical aperture NA = 0.2 was used.

3 Results and discussion

3.1 Quantification of dielectrophoretically immobilized proteins

Reliable quantification methods are required to determine the influence of different experimental parameters on the dielectrophoretic immobilization of proteins. Usually, fluorescence dyes are used to label proteins, and DEP experiments are evaluated by fluorescence microscopy. A new approach for the investigation of the dielectrophoretic immobilization of proteins using an AFM is presented, and its advantages and disadvantages are demonstrated and compared to fluorescence microscopy.

3.1.1 Relative quantification using fluorescence microscopy

In this work, three different programs were applied for the determination of fluorescence intensities. One being the microscopic imaging software *ImageJ* [134], the second being a software for the evaluation of microarray slides, *GenePix Pro* (Axon Instruments), and the third being a software for scanning probe microscopy evaluations, *Gwyddion* [135]. The different programs were employed on the one hand to mutually validate the evaluation protocols. On the other hand, depending on the nature of the fluorescence micrograph and, e.g., the number of displayed electrodes, a choice of evaluation protocols is handy to meet the differing requirements for evaluation.

Comparison of different evaluation softwares

The most obvious approach to determine fluorescence intensities of different ROIs in a fluorescence micrograph is to use a microscopy evaluation software like *ImageJ*. ROIs of various shapes and sizes can be defined manually in the image, and the corresponding mean intensities can be calculated. Individual selection of each ROI brings the advantage that there are no restrictions for the choice of ROIs, i.e. regions showing low intensities, can be selected without any problems. This evaluation procedure is straightforward and particularly useful when the number of ROIs is limited.

When more ROIs need to be evaluated, manual selection is tedious and automated detection of ROIs is desirable. Microarray readers are commonly used to scan the numerous fluorescent spots on microarray slides. The spots are arranged in arrays that are automatically evaluated by softwares provided with the readers. The electrodes used for dielectrophoretic immobilization are about two orders of magnitude smaller than most microarray spots, but due to the regular arrangement of the electrodes in arrays the fluorescence images resemble those of microarray slides. Consequently, fluorescence images of the electrode arrays can be acquired using a fluorescence mi-

croscope, and the image files can be evaluated by a microarray evaluation software, i.e. *GenePix Pro*.

Similarly, an automated detection of all fluorescing electrodes contained in a fluorescence image is feasible with the scanning probe microscopy evaluation software *Gwyddion*. This software features a tool to analyze grains that automatically recognizes structures from their height differences or curvatures. This tool generates a mask of which characteristics like the mean heights, areas, etc. can be calculated. Evaluation with *Gwyddion* is advisable for better comparability of fluorescence intensities and parameters obtained from AFM measurements (deposit heights or volumes) by evaluating the respective images with the same software. The evaluation using

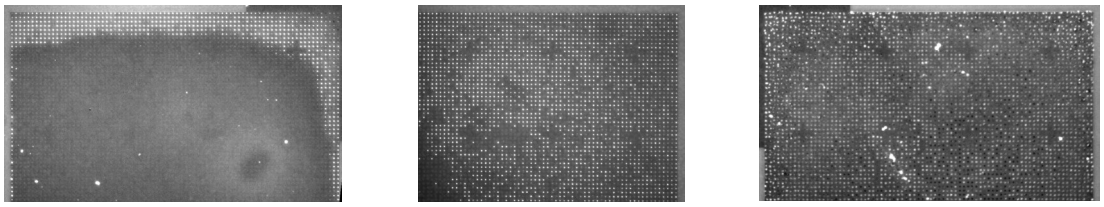

(a) 5 V. **(b)** 10 V. **(c)** 20 V.

Figure 3.1: Three individual electrode subarrays with HRP-Oyster-555 immobilized at 10 kHz and different voltages; fluorescence micrographs.

ImageJ, *GenePix Pro*, or *Gwyddion* for the determination of fluorescence intensities is exemplarily shown for three experiments on three individual electrode chips (Fig. 3.1). Horseradish peroxidase (HRP) was labeled with the fluorescence dye Oyster-555. According to the calculated DOL, three fluorophores were bound per enzyme. HRP-Oyster-555 was then immobilized on the electrodes of one subarray by applying 5 V, 10 V and 20 V, respectively, at a constant frequency of 10 kHz for a duration of 20 min. At the lowest voltage a coverage of about 25 % of the electrodes resulted whereas at higher voltages immobilization occurred at nearly all electrodes.

With *ImageJ*, 100 electrodes were selected manually as circular ROIs and 20 background ROIs of the same shape and size were selected in the electrode gaps. From these ROIs, mean fluorescence I_{ROI} or background intensities I_{BG} were determined. The (mean) fluorescence intensities at the electrodes were subsequently background corrected: $I_{\mathrm{ROI}} - I_{\mathrm{BG}}$.

With *GenePix Pro*, the microarray evaluation software, arrays were defined with a fix number of columns and lines. The spot size was automatically fitted to the electrodes, and the intensities were background corrected each with a local background intensity from the space surrounding the electrodes. Nearly all electrodes that were visible in the fluorescence micrographs (840, 2700 or 4800 electrodes) were considered.

Using *Gwyddion*, the scanning probe microscopy evaluation software, all electrodes

contained in the fluorescence micrographs with fluorescence intensities above a certain threshold (677, 2079 or 3963 electrodes) were considered.

The normalized mean intensities for the three experiments are displayed in Fig. 3.2. All three independent evaluation methods gave quite similar results showing decreas-

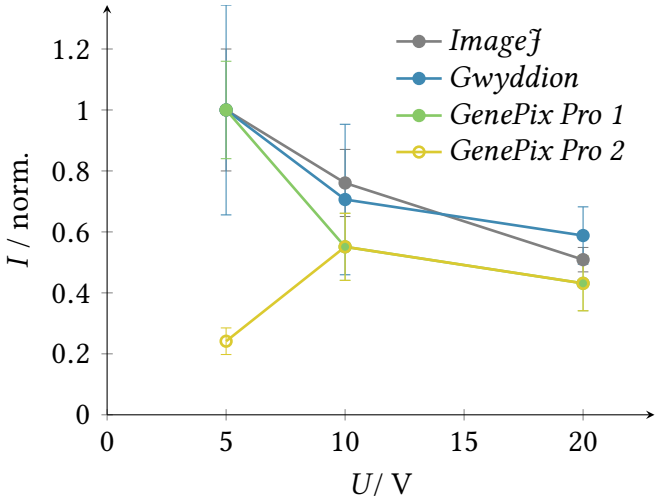

Figure 3.2: Normalized fluorescence intensities of immobilized HRP-Oyster-555, evaluated using three different programs. With the program *GenePix Pro*, two values were determined for the data point at 5 V.

ing intensities with higher voltages applied for DEP. From DEP theory an increase would be expected due to the square dependence of the dielectrophoretic force on the applied voltage (Eq. (1.1)). There are two explanations for this phenomenon of decreasing intensities. The first explanation assumes a positive correlation of fluorescence intensities with the amount of immobilized proteins. In this case the coverage of only about 25 % of the electrodes in the experiment with the lowest voltage leads to a distribution of the proteins onto less electrodes resulting in higher amounts of accumulated proteins per covered electrode. The second explanation assumes a negative correlation of fluorescence intensities with the amount of immobilized proteins. High amounts of immobilized proteins would lead to a dense packing of fluorophores and a decrease in fluorescence intensity caused by self-quenching of the fluorophores.

The very good agreement of the results using *ImageJ* and *Gwyddion* supports the qualitative equivalency of the two methods. With these two evaluation procedures, electrodes showing low fluorescence intensities were omitted. Only *GenePix Pro* evaluation enabled a consideration of those electrodes. In the experiment with the lowest applied voltage and a coverage of only about 25 % of the electrodes this leads to a significant difference. As a consequence two data points were determined for this experiment. *GenePix Pro 1* omits the electrodes with low intensities similar to the evaluation procedures using *ImageJ* and *Gwyddion*. At contrast those electrodes were taken into

account for *GenePix Pro 2*. The overall lower mean intensity values obtained by *GenePix Pro* evaluation are supposedly the result of the automated selection of a background from the area surrounding the electrodes. In those areas fluorescence might be higher than in the electrode gaps and thus lead to a reduction of the background corrected intensity values.

The choice of the program that is best suited for an evaluation depends on the specific requirements; e.g., the number of ROIs and the presence or absence of fluorescence localized at some of the ROIs have to be taken into account.

3.1.2 Comparison of fluorescence microscopy and atomic force microscopy for protein quantification on an electrode-to-electrode basis

One immobilization experiment using an electrode chip that comprises four electrode subarrays with 6256 electrodes each can be considered as simultaneous experiments on 6256 individual electrodes. Theoretically, all electrodes are equally active, and for most evaluations it is justified to average their characteristics. However, fluid flows and the protein supply from the solution vary with spatial dependence. Therefore, a comparison of fluorescence intensities and protein deposit heights on an electrode-to-electrode basis is of special interest.

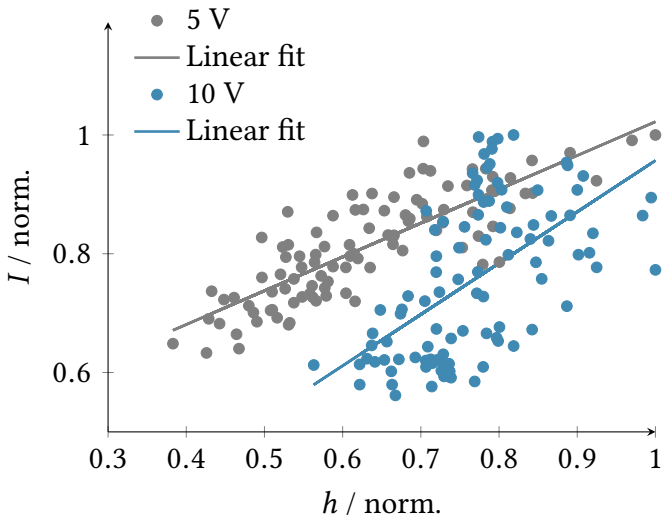

Figure 3.3: Correlation of normalized mean intensities of 100 electrodes with immobilized BSA-Oyster-647 obtained from fluorescence and AFM height images. Dielectrophoretic immobilization was performed at 5 V and 10 V on separate electrode chips.

A prerequisite for this kind of evaluation is an electrode chip with evenly distributed proteins to enable a clear assignment of specific electrodes. As this assignment is not

readily possible with an automated detection of the electrodes, the manual approach using *ImageJ* was chosen. The amount of immobilized proteins was determined exemplarily for two experiments with fluorescently labeled BSA immobilized at 5 V or 10 V, respectively. ROIs were selected manually using *ImageJ* to ensure that exactly the same 100 electrodes in an outer corner of the subarray were selected in the correct order. Mean intensities of these ROIs were determined from a fluorescence micrograph and from an AFM height image. The correlation between normalized fluorescence and AFM data is linear for both experiments (Fig. 3.3), with Pearson's correlation coefficients of $r_{5\,\mathrm{V}} = 0.83$ and $r_{10\,\mathrm{V}} = 0.57$. Deviations are interpreted as a result of fluorescence quenching in large protein deposits with high fluorophore densities or of weak fluorescence in small protein deposits.

3.1.3 Absolute quantification using atomic force microscopy

Quantification of dielectrophoretically immobilized proteins

The number of proteins immobilized on a single electrode can be estimated by calculating the maximal number of immobilized proteins using the crystal unit cell size. According to the Protein Data Bank the symmetry group is C_{121}, hence a unit cell of 21.56 nm × 4.51 nm × 14.24 nm contains 8 protein molecules [136].

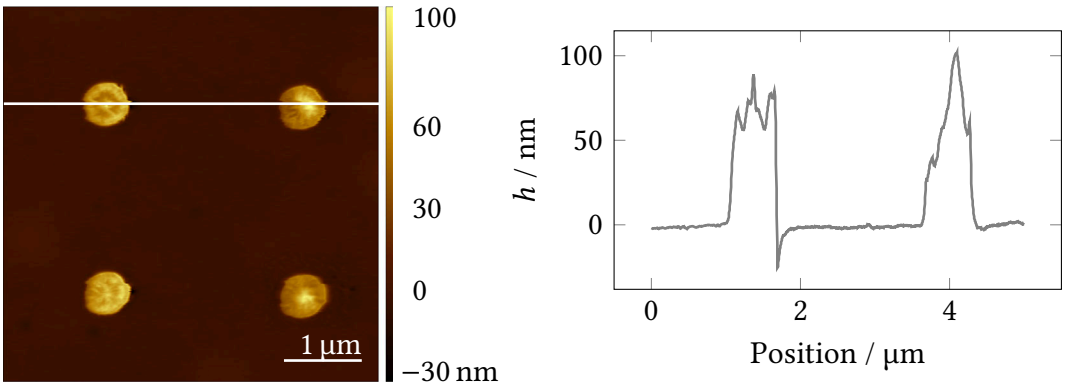

(a) AFM height image. **(b)** AFM height profile.

Figure 3.4: Four tungsten cylinder electrodes with dielectrophoretically immobilized bovine serum albumin.

During standard DEP experiments with durations between 5 min to 10 min, all of the electrode surface is covered with proteins that pile up to cylindrically shaped deposits (Fig. 3.4). Mean volumes in the presented example amount to approximately $3.1 \cdot 10^{-20}\,\mathrm{m}^3$. Assuming a packing of proteins that is not as dense as in the crystal, the maximal number of proteins in this deposit can be calculated according to Eq. (2.6). It amounts to $1.8 \cdot 10^5$. Analogously, the maximal number of proteins in the largest

and in the smallest deposits on tungsten cylinder electrodes was determined: Up to $4.4 \cdot 10^6$ protein molecules were calculated for the largest deposits with volumes of $7.6 \cdot 10^{-19}\,\mathrm{m}^3$ after an experiment at 10 kHz and 20 V. After the shortest experiment, which was terminated after just one second, a protein volume of $9.4 \cdot 10^{-21}\,\mathrm{m}^3$ had accumulated per electrode, corresponding to a maximal number of $5.4 \cdot 10^4$.

Quantification of small protein deposits

Apart from the proteins accumulated at the electrodes, some AFM height images showed small deposits on the SiO_2 surface. The determination of the dimension of these deposits is limited by the resolution of the actual AFM setup, which is approximately 15 nm in x, y direction, whereas in z direction a resolution of 1 nm can be reached. Consequently, it does not make sense to calculate the deposit volume and the number of proteins contained therein. However, it is possible to estimate the number of protein layers in those deposits from their heights. This is exemplarily demonstrated for eGFP deposits on a TiN electrode chip (Fig. 3.5a), where eGFP was dielectrophoretically immobilized.

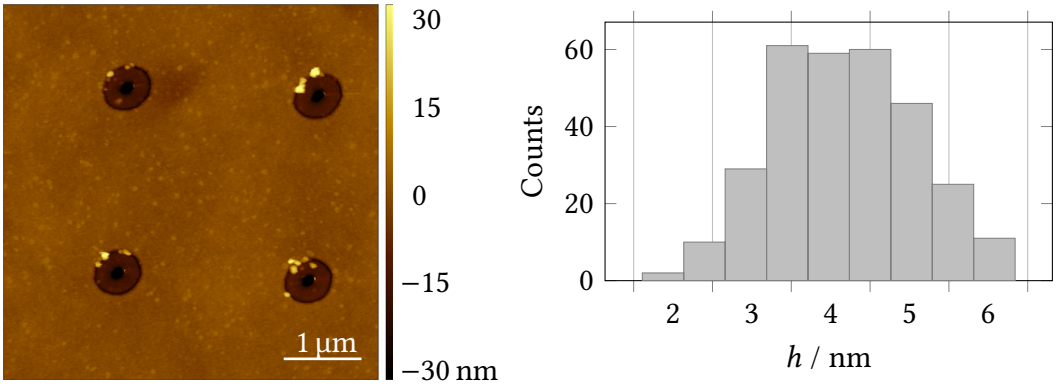

(a) AFM height image. **(b)** Histogram of 303 small deposit heights.

Figure 3.5: Titanium nitride ring electrodes with dielectrophoretically immobilized eGFP deposited at the electrodes and additional small aggregates on the SiO_2 surface between the electodes.

The TiN electrodes were chosen because of their thin ring structures along which less proteins are immobilized than on the much larger surface of the tungsten electrodes. The experimental parameters were chosen with the intention to achieve as small deposits at the electrodes as possible. After field application and subsequent rinsing, the chip was examined with an AFM to investigate the spatial distribution of the proteins along the electrode structures. Interestingly, the proteins were not distributed evenly along the TiN rings. They had accumulated preferably on one side of the electrodes, which might be the result of fluid rolls along the edges of the electrode chip. In

the electrode gaps, additional deposits with smaller dimensions could be detected as a result of the good height resolution of the AFM measurement. The heights of 14 protein aggregates at the electrodes and of 303 small aggregates in the electrode gaps (Fig. 3.5a) were determined to quantify the protein amounts. The deposits along the ring electrodes had heights in the range from 7 nm to 27 nm and volumes of $6 \cdot 10^{-23}\,\mathrm{m}^3$ to $51 \cdot 10^{-23}\,\mathrm{m}^3$. The mean height was (15 ± 4) nm, which corresponds to approximately four to five protein layers. The small deposits in the gaps had a mean height of (4.7 ± 0.5) nm indicating monolayer spots of eGFP. The deposit height show a Gaussian distribution around the mean height (Fig. 3.5b). From the difference in the size of protein deposits in the electrode gaps and on the electrodes it is evident that the proteins are not aggregated in solution prior to field application, and that the formation of aggregates is not a direct result of the field application but rather a process of accumulating proteins in the course of the experiment.

3.1.4 Discussion

Fluorescence microscopy is the method of choice for investigations of biomolecule manipulations. It is easy to implement, and it allows real-time imaging of DEP experiments with fluorescently labeled biomolecules. Thus, reversible accumulations and fluid rolls that move proteins along can be observed. However, the detection of low protein amounts was not always possible due to a low signal-to-noise ratio. The background noise was presumably caused by reflections at the metal surface and stray light, additionally, non-specific adsorption lead to background fluorescence. Above that, fluorescence quenching at high label densities or time-dependent bleaching render a reliable quantification of fluorescence intensities difficult. Without the use of intensity standards for calibration, only a relative quantification is possible.

Three different programs were compared for the relative quantification of dielectrophoretically immobilized proteins using fluorescence intensities located at the electrodes. Using *ImageJ* the selection of ROIs located at the electrodes had to be done manually, which can be tedious when considering several hundreds or even thousands of electrodes. In contrast, protocols for the use of the microarray evaluation software *GenePix Pro* and for the scanning probe microscopy evaluation software *Gwyddion* were developed to achieve an automated evaluation of the great number of electrodes. The automation provides a high reproducibility by defining an array with the same number of columns and rows and the same spot size or by selecting the same threshold, respectively. Moreover, evaluation is faster even with very high numbers of ROIs, and increasing the number of ROIs does not significally impact evaluation times. *GenePix Pro* also detects spots with low intensity more easily. *Gwyddion* allows better compa-

rability of fluorescence intensitities with AFM height or volumes.

The AFM was introduced as an approach to absolute quantification of dielectrophoretically immobilized proteins. Whilst atomic force microscopy is undeniably a time-consuming method, it also holds valuable advantages: The high spatial resolution of the AFM revealed the distribution of proteins on single nanoelectrodes and in the gaps in between. Very small amounts down to only a few proteins could be detected. It was found that protein deposits in the electrode gaps were smaller than the smallest deposits detected on the electrodes. Thus, accumulation in the course of a DEP experiment could be distinguished from aggregation in solution prior to field application. The areas covered with proteins and the heights of the protein deposits are accessible from height measurements in contact mode. Consequently, atomic force microscopy allows an absolute quantification of the amount of dielectrophoretically immobilized proteins. Estimates of the maximal number of immobilized proteins per electrode were calculated on the basis of their crystal structure. These values give an idea of the order of magnitude of the protein amounts contained in the deposits after dielectrophoretic immobilization. With a better knowledge of protein interactions and their arrangement on the electrodes, this number can be determined more precisely.

In general, both quantification methods using fluorescence intensities on the one hand and AFM heights or volumes on the other hand yielded matching results: Those electrodes that were suitable for both evaluation methods gave a strong correlation between fluorescence intensities and AFM heights in the investigation on an electrode-to-electrode basis. For those electrodes that can only be evaluated by either AFM or fluorescence measurements, the two methods complement each other.

3.2 Dielectrophoretic immobilization of proteins on nanoelectrode arrays

In DEP experiments, Brownian motion and AC electrokinetic effects compete with each other [14]. Of the latter, electrothermal flow is the most dominant factor besides DEP at frequencies in the MHz range, whereas AC EOF interferes with DEP at lower frequencies [97, 140, 141]. As AC EOF is a tangential force [15], it can be minimized by employing electrode configuration with low tangential components. For this reason, nanoelectrode arrays with one distant counter electrode above the array were designed and used for protein DEP in this work. Not only are electrode dimensions, shape, the gap width and arrangement of substantial importance for the interplay of the involved forces. Also experimental parameters have to be optimized for each electrode configuration. In this section the influence of frequency, voltage, experiment duration, and

medium conductivity on dielectrophoretic immobilization is examined.

3.2.1 Frequency dependence

Polystyrene beads with a diameter of 2 µm were used to monitor the influence of the frequency in dielectrophoretic immobilization experiments in real-time. The employment of beads is advantageous since each bead can be tracked individually, and the response upon frequency variation is directly observable. This allows the observation of reversible accumulations and of fluid flows like rolls or vortices, that do not lead to permanent immobilization at the electrodes. The applied frequency was varied from 1 kHz to 10 MHz at a constant voltage of approximately 10 V. Movement of the beads away from the electrode arrays was observed for high frequencies in the range between 100 kHz to 2 MHz. The mechanism responsible for this movement is presumably negative DEP. Attraction to the electrodes by positive DEP occurred between 1 kHz to 100 kHz, indicating a crossover frequency of 100 kHz. Most beads were immobilized at the electrodes, but some beads moved from one electrode to a neighboring one, or they were carried away by fluid flows. Below 5 kHz, in addition to an attraction towards electrodes, gas bubbles were formed at the edges of the electrode array and at the corner electrodes (Fig. 3.6). The formation of these gas bubbles is the result of water electrolysis: $2\,H_2O\,(l) \longrightarrow 2\,H_2\,(g) + O_2\,(g)$. Electrolysis is facilitated at low frequencies, but it is also dependent on the applied voltage.

With proteins only positive DEP was observed in the whole frequency range. This is probably a result of the smaller dimension of proteins and the associated higher crossover frequency [142, 143]. At frequencies around 100 kHz, fluid flows were more

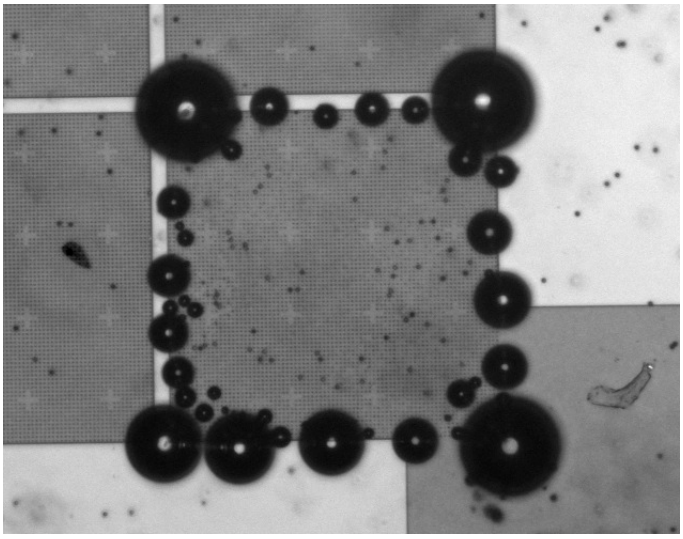

Figure 3.6: Bubble formation due to water electrolysis at the edges of the contacted electrode array in a DEP experiment with 2 µm beads; 10 Hz, 38 V.

pronounced, and at frequencies in the MHz range dielectrophoretic accumulation was less effective. Consequently, a compromise has to be made for the choice of the optimal frequency in order to maximize dielectrophoretic attraction and at the same time circumvent water electrolysis at lower frequencies. This optimum for protein immobilization on the electrode arrays is 10 kHz.

3.2.2 Voltage dependence

From the voltage variation at a constant frequency of 10 kHz, a threshold voltage of approximately 5 V was obtained that had to be overcome for positive DEP to start. Voltages up to 20 V lead to fast bead movement towards the electrodes. At higher voltages the movement was even faster, but at the same time bubble formation could be observed as a result of water electrolysis, which lead to gas formation. These gas bubbles formed mainly at electrodes of the outmost lines and corners of the subarrays (Fig. 3.6).

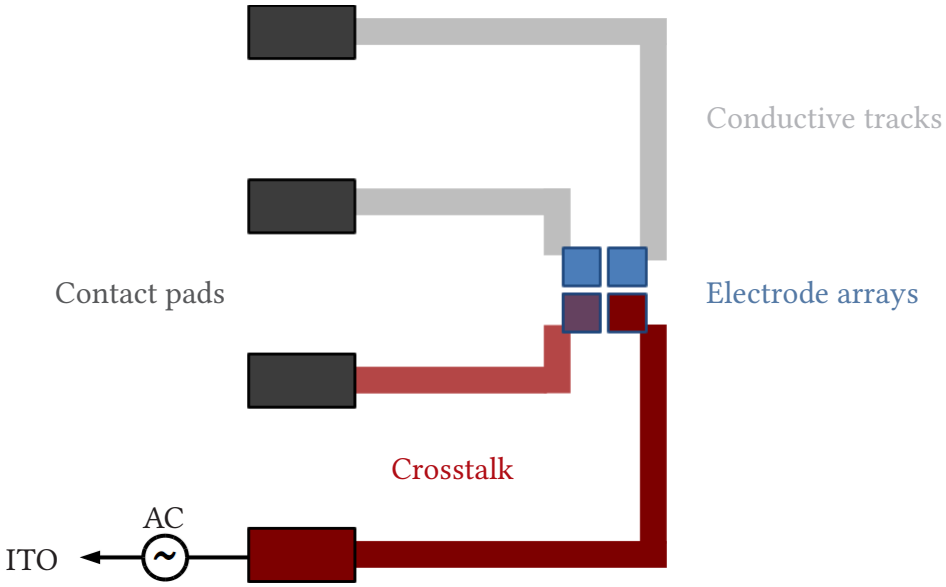

Figure 3.7: Scheme of the electrode chip showing four contact pads and corresponding conductive tracks leading to the four electrode subarrays. One subarray (dark red) is connected to a voltage source causing a crosstalk effect on the neighboring subarray (red).

Furthermore, effects at neighboring subarrays were observed that resembled the effects obtained at small applied voltages. The latter were caused by electric crosstalk from the connected conductive track to the next track that runs in parallel with a distance of only 2 mm. Thus, voltages are capacitively coupled into subarrays that are not directly connected to the voltage source. The effect is most pronounced on the neighboring subarray that has a conducting track in parallel. The other neighboring

subarray and the one located diagonally show less effects owing to the more remote conducting tracks (Fig. 3.7). The electric crosstalk has to be considered when separate experiments are performed on different subarrays of an electrode chip and when an unused subarray is considered as negative control.

The effect of voltage variation on dielectrophoretic immobilization of proteins was systematically investigated with fluorescently labeled BSA. The frequency was 10 kHz, and an experiment duration of 20 min was kept for all experiments. Voltages of 1, 5, 10 and 20 V were applied to separate electrode chips. After field application the chip was rinsed with water and dried in a stream of nitrogen. With the exception of the experiment at 1 V, the proteins remained immobilized after rinsing. Additionally, a reference chip was prepared by incubating the chip for 20 min with fluorescently labeled BSA, followed by rinsing and drying analogously to the treatment of DEP chips. Without the application of an electric field, proteins adhere to the SiO_2 surface and to the electrodes by non-specific interactions. No preference for either SiO_2 or tungsten could be detected on the reference chip. The amount of immobilized proteins

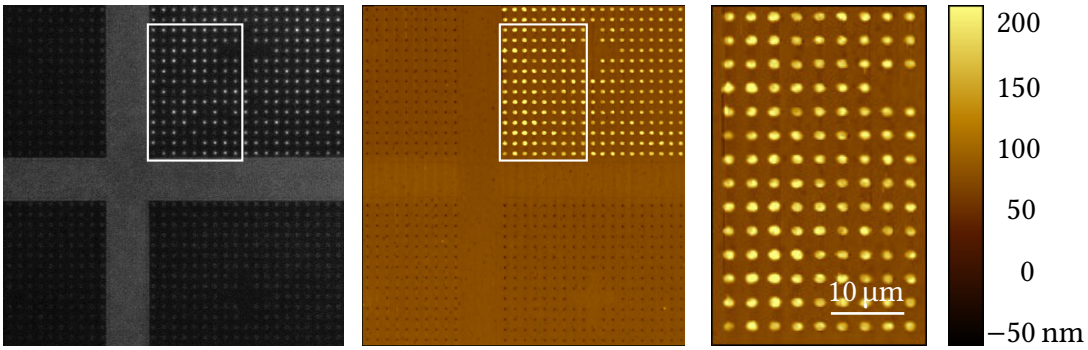

(a) Fluorescence micrograph. **(b)** AFM height image. **(c)** Electrodes for evaluation.

Figure 3.8: Fluorescence micrograph (a) and AFM height image (b) of the electrode chip with immobilized BSA-Oyster-647. The section comprising the 124 electrodes used for evaluation (c) is framed in (a) and (b).

was determined for each experiment using fluorescence intensities and deposit volumes. Sections of the chip comprising 124 electrodes were chosen for evaluation (Fig. 3.8). Background corrected intensities from fluorescence measurements were averaged for those 124 electrodes for each experiment, and the deposit volumes from AFM measurements at those 124 electrodes were added together for each experiment. Both approaches revealed increasing protein amounts with higher voltages (Fig. 3.9). The standard deviations of the fluorescence intensities or the deposit volumes are displayed as error bars to visualize the variations within one experiment.

The high intensity value for the reference chip (0 V) measured by fluorescence mi-

croscopy is inconsistent with the low volume measured with the AFM. This apparent contradiction can be explained by reflections of the excitation light at the surface of the metallic electrodes that partly pass the fluorescence filters, which have optical densities between 5 and 6, and transmit 10^{-5} to 10^{-6} of the excitation light. As a consequence, this data point was not included in the fit for the fluorescence intensity I. At the highest potential applied, 20 V, pronounced fluid flows were observed during the experiment. Furthermore, large protein aggregates were formed, resulting in a reduced number of evaluated deposits with broader variations and, hence, a dramatically higher standard deviation of this data point.

The dependence of the fluorescence intensity I or the deposit volumes V, respectively, on the applied voltage was fitted by square functions; errors were calculated as standard deviations of the fit parameters: $I = (8.6 \pm 0.1) + (0.079 \pm 0.004) \cdot U^2$, $R^2 = 0.991$; $V = (1.55 \pm 0.08) \cdot 10^{-9} + (1.29 \pm 0.04) \cdot 10^{-11} \cdot U^2$, $R^2 = 0.996$.

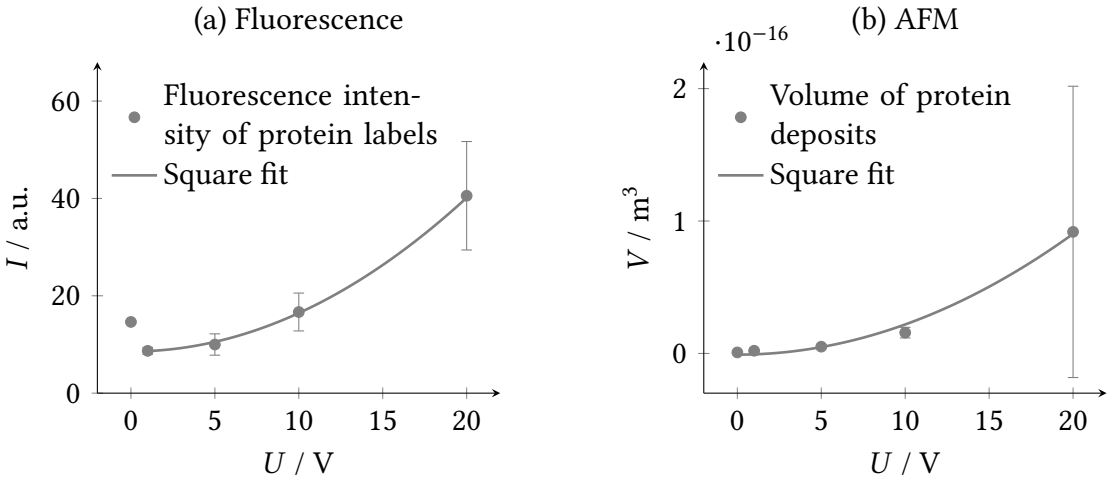

Figure 3.9: Dependence of the amount of immobilized proteins on the applied voltage during DEP experiments at 10 kHz with constant experiment duration of 20 min, evaluated for identical chips in (a) and (b); the error bars indicate the variation for each experiment. (a) Relative quantification via fluorescence intensities; (b) Absolute quantification via AFM deposit volumes.

The applied voltage is a crucial parameter for the amount of immobilized proteins owing to the square dependence of the dielectrophoretic force on the electric field gradient. For the choice of the optimal voltage it is advisable to minimize effects that interfere with positive DEP; these effects being, e.g., pronounced fluid flows and water electrolysis. At the same time the threshold voltage has to be considered. Thus follow low applied voltages that exceed the threshold. In the presented electrode configuration a voltage of 10 V was found to be optimal for dielectrophoretic immobilization of both polystyrene beads and proteins.

3.2.3 Experiment duration

The influence of the experiment duration on the amount of immobilized proteins was investigated by immobilizing BSA-Oyster-647 on six separate electrode chips with an applied frequency of 10 kHz and a voltage of 10 V for 1 s, 10 s, 1 min, 5 min, 10 min and 20 min, respectively. As fluorescence intensities for short experiment durations yielded no detectable change in fluorescence, the amount of immobilized proteins was determined with the AFM. *Gwyddion*'s grain analysis tool was used to calculate the overall deposit volume on the same 124 electrodes of each chip by multiplication of the mean heights with the areas covered by proteins. During the first seconds the

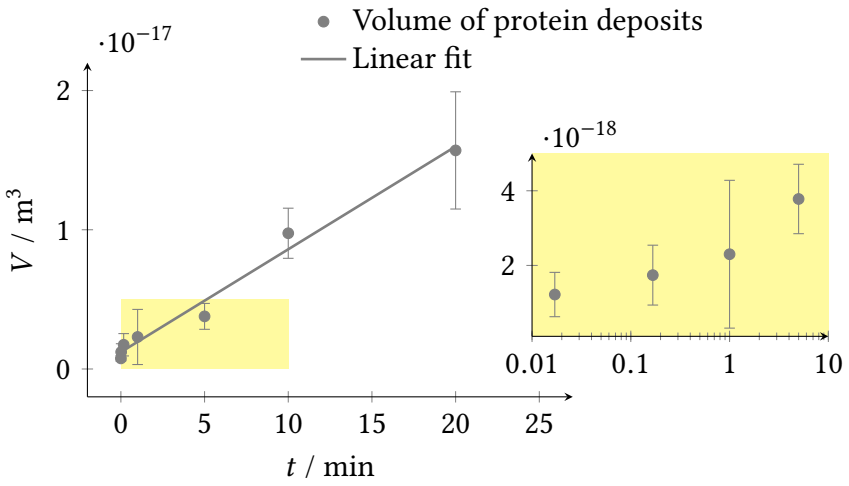

Figure 3.10: Dependence of the amount of immobilized proteins on the duration of DEP experiments at 10 kHz and a constant applied voltage of 10 V; the error bars indicate the variation for each experiment. Inset: magnification of the yellow highlighted region.

proteins in direct vicinity of the electrodes are attracted, leading to a steep rise in deposit volumes (Fig. 3.10). In the course of the experiment, proteins are continuously attracted to and accumulated at the electrodes. This leads to an increasing amount of immobilized proteins with longer experiment durations. The correlation is linear ($V = (1.2 \pm 0.4) \cdot 10^{-18}\,\mathrm{m}^3 + (7.4 \pm 0.4) \cdot 10^{-19}\,\mathrm{m}^3\,\mathrm{min}^{-1} \cdot t$, $R^2 = 0.980$, errors were calculated as the standard deviations of the fit parameters.) with no signs of saturation, which could be caused by a limited protein supply, and no substantial disturbance of the electric field by immobilized proteins on the electrodes. This means that the amount of immobilized proteins can be directly controlled by the duration of an experiment given a sufficient supply of proteins.

3.2.4 Medium conductivity

Water is a favorable medium for dielectrophoretic experiments with objects that are of interest for bioanalytic applications. Ultrapure water with very low conductivity is often used to prevent effects like Joule heating, electrothermal fluid flows and electrolysis of water [14]. Numerous biomolecules require the presence of specific ions or detergents for proper folding. Functional groups of amino acid residues on the surface of proteins, for example, are stabilized by ions in solution. Consequently the absence of ions can lead to aggregation of proteins, possibly combined with denaturation and a loss of their biofunction. In general, high protein concentrations promote aggregation.

The proteins BSA, eGFP and the enzyme HRP used in this thesis are relatively robust, and they were dissolved in water without the addition of buffer components or detergents for DEP experiments. Nevertheless, in some experiments with high voltages and pronounced fluid flows, aggregation of proteins occurred. For these reasons the applicability of the dielectrophoretic immobilization procedure was investigated with media of different conductivities (Table 3.1). The conductivity was adjusted by dilution of a phosphate buffer (c = 12.6 mM, pH = 7.46, κ = 1.9 mS cm^{-1}), and it was measured with a conductivity meter. The frequency was kept constant at 10 kHz and the maximal applicable voltage was determined for experiments in undiluted buffer, in 1:10 dilution, 1:100 dilution, and in ultrapure water, respectively. 20 nm beads were suspended in the different media to monitor dielectrophoretic effects and fluid flows. Positive DEP was observed in ultrapure water with voltages up to 26 V. At this point,

Medium	Conductivity	Maximal voltage	DEP
H_2O, ultrapure	<1 µS cm^{-1}	26 V	yes
Buffer, diluted 1:100	23 µS cm^{-1}	20 V	yes
Buffer, diluted 1:10	200 µS cm^{-1}	19 V	yes
Buffer, undiluted	1900 µS cm^{-1}	15 V	no

Table 3.1: Maximal voltages used for DEP experiments with 20 nm beads suspended in aqueous media of different conductivities.

gas bubbles were formed due to water electrolysis. In 1:100 diluted buffer, bubble formation started at 20 V, and in 1:10 diluted buffer at 19 V. At lower voltages, positive DEP could be observed. Only in undiluted buffer there was no dielectrophoretic attraction towards the electrodes although the voltage could be increased to 15 V before bubble formation started.

From these measurements it can be concluded that a threshold value has to be overcome for water electrolysis to start. This threshold is given by the intrinsic potential needed for the electrolysis reaction on the one hand and by the material-dependent

overpotential, which is required for the activation energy of gas formation at the electrodes, on the other hand. The efficiency of electrolysis further depends on medium conductivity and temperature due to their influence on ion mobility. The small electrode distance in the present setup further reduces the resistance of the medium and facilitates water electrolysis.

From the conductivity variations it can be concluded that low-conductance media are favorable for dielectrophoretic experiments since higher voltages can be applied before electrolysis starts and before DEP is hampered by gas bubble formation. In the nanoarray configuration at hand, where the counter electrode is about 100 µm away, DEP experiments can be conducted with objects suspended in media with conductivities up to approximately 200 $\mu S\,cm^{-1}$.

3.2.5 Discussion

Several experimental parameters that affect the dielectrophoretic force were optimized for the electrode configuration that was used for dielectrophoretic immobilization of proteins. According to theory, the frequency is decisive for the direction of the dielectrophoretic force (Eq. (1.1)). For proteins only positive DEP was observed, whereas polystyrene beads underwent negative DEP at frequencies above a crossover frequency of approximately 100 kHz. These results are in agreement with findings in the literature on beads [144] and on proteins, where negative DEP was only observed at frequencies in the higher MHz range, i.e. 40 MHz for myoglobin [145], that were not applied here. Frequencies in the range of 0.1 MHz to 1 MHz or higher strongly promoted fluid motion. These flows can be of electrothermal origin [14], since the high field inhomogeneity needed for molecular DEP also leads to strong gradients of field induced heating. This results in gradients of the electrical properties of the medium that, combined with the electric field, give rise to fluid flows. If the protein concentration is sufficiently high, these fluid flows provide a steady supply of proteins in the course of an experiment so that dielectrophoretic attraction is not limited by depletion in the close vicinity of the electrodes or slow diffusion. This was confirmed by the linear correlation of the amount of immobilized proteins with experiment duration.

A square dependence was found for the effect of the applied voltage on the amount of immobilized proteins, which is in agreement with theory: The dielectrophoretic force is proportional to the square of the applied voltage (Eq. (1.1)). In a study on the dielectrophoretic collection of RNA, Giraud et al. found the expected square dependence on voltage starting at a threshold voltage [28]. The threshold effect is explained by Brownian motion and streaming forces that have to be overcome by the dielectrophoretic force. In this thesis, a threshold was observed for all proteins used. Such

an effect has also been reported in several publications on, e.g., viruses [74], metallic nanoparticles [146] and protein molecules [41].

The irreversible immobilization of proteins on the electrodes is presumably the result of strong dielectrophoretic forces, which draw proteins that close to the electrode surface and close to other protein molecules that water molecules in between are removed. Thus, the impact of hydrophobic interactions strongly increases, leading to permanent adhesion of proteins.

In general, the dielectrophoretic immobilization method is easy to implement and generally applicable to small objects spanning various types of cells, bacteria, viruses, polystyrene, metallic or semiconducting particles, DNA and proteins, with no or only very little adjustments. Most other immobilization methods have to be individually adjusted to address functional groups. This usually involves chemical modifications with several reaction steps both at the object and at the surface. The main restriction of dielectrophoretic immobilization is the limited applicability of solutions with higher conductivities due to disturbing bubble formation by water electrolysis. The smaller the electrode gap and the higher the temperature and the medium conductivity, the more likely electrolysis is to occur. In the present setup, dielectrophoretic experiments can be conducted in solutions with conductivities up to $200\,\mu S\,cm^{-1}$, which excludes all biomolecules for that a handling in common buffer solutions with a certain ion strength or with the addition of ionic detergents is mandatory.

3.3 Functionality of dielectrophoretically immobilized enzymes

Immobilization of enzymes on surfaces and on metal surfaces in particular can lead to rearrangements in the protein structure [147], which might further cause decreased enzyme activity or even complete inactivation. On top of this, enzymes are exposed to extremely high electric fields during dielectrophoretic immobilization. Therefore, the functionality of dielectrophoretically immobilized enzymes is not self-evident. In this section, the dielectrophoretic immobilization of enzymes and their functionality is shown. First, the catalytic activity is demonstrated by conversion of a suitable substrate for the enzyme that can be assessed by optical microscopy. Secondly, the enzymatic efficiency is quantified and compared for different immobilization parameters. Finally, the long-term stability of HRP immobilized on the tungsten nanoelectrodes is investigated.

3.3.1 Substrates for horseradish peroxidase activity detection

Luminol as a substrate for horseradish peroxidase

The chemiluminescence reaction of luminol in the presence of H_2O_2 is catalyzed by enzymes, e.g. by HRP. The oxidation product 3-aminophthalate is produced in an excited state and relaxes under the emission of a photon. First experiments were conducted in solution in a chambered coverglass. The focus of the optics was set into the volume, and photons in this volume were collected by a 10 × objective (NA = 0.17) and detected with the FCS unit of the CLSM. In a mixture of luminol and H_2O_2 in absence of HRP, a count rate comparable to that of pure H_2O, the negative control, was measured. Addition of the enzyme started the oxidation reaction. Count rates were measured every 30 s and background-corrected by subtraction of the count rate prior to HRP addition. The count rate increased quickly and reached its maximum shortly after 2 min (Fig. 3.11). Then, it decreased continuously and reached the background level after approximately 15 min. The delay of the maximal count rate by 2 min is most likely caused by diffusion of the enzyme into the observed volume. Then, luminol molecules in the proximity of the enzymes are oxidized, and photons emitted by the oxidation product, 3-aminophthalate, are detected. The count rate decreases with luminol consumption, until the reaction comes to an end.

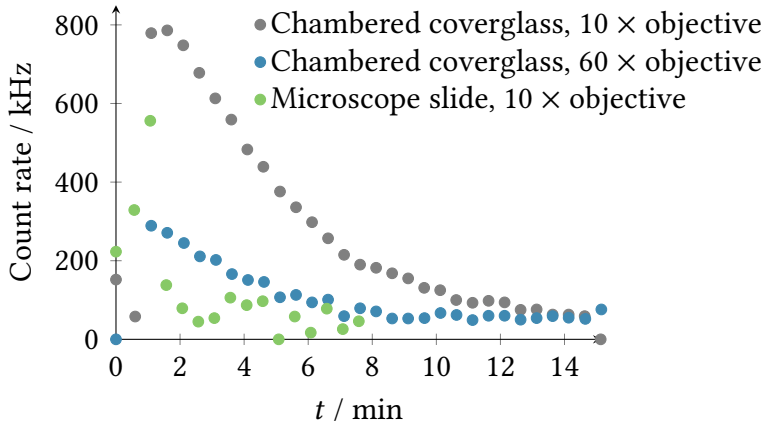

Figure 3.11: Background-corrected count rates of photon emission upon relaxation of excited 3-aminophthalate being formed as the result of the horseradish peroxidase-catalyzed oxidation of luminol. The reaction was carried out in different sample carriers (chambered coverglass or microscope slide) and photons were collected by different microscope objectives (10 × or 60 ×).

If the activity of immobilized enzymes is to be monitored at specific nanoelectrodes, an objective with higher magnification and numerical aperture (NA) is needed to distinguish the electrodes. Therefore, the experiment in solution was repeated with a 60 × objective (NA = 0.70). Here, the count rate showed the same trend (Fig. 3.11) with

a quick increase of the count rate, a maximal count rate after 1 min, and a continuous decrease down to the background level after approximately 9 min. The maximal count rate, however, was only 37 % of that measured with the 10 × objective. This is probably the result of the smaller observation volume of the 60 × objective and the smaller number of emitting molecules contained therein.

In view of the small dimensions of the electrode chips and the associated low reaction volumes, the sample volume was decreased to less than 10 µL. Luminol and H_2O_2 were pipetted onto the microscope slide. The 10 × objective was used to obtain the highest possible count rates in the small reaction volume. Due to its location below the microscope slide the start of the reaction could be monitored directly upon HRP addition. After 1 min, the maximum was reached (Fig. 3.11), followed by a steep decrease within a time span of only 30 s. The background value was reached after less than 3 min. Although the maximal count rate amounted to 70 % of that measured in the larger sample volume, the fast decay is unfavorable for the determination of enzymatic activity.

Observations of the non-transparent electrode chip are only possible with an upright microscope, and the chip has to be taken from the microscope stage for sample addition. As the preparation of the electrode chip for microscopic observation takes at least 1 min the luminescence might be decayed for the most part by then. Unfortunately, the sample volume cannot be increased to prolong the reaction as it is limited by the dimensions of the electrode chip. In spite of the advantages of a chemiluminescent substrate like luminol that does not need an external excitation source and that is very sensitive, the fast reaction kinetic and the intensity decrease with substrate consumption rule this substrate out for the detection of HRP activities after dielectrophoretically immobilization.

Dihydrorhodamine 123 as a substrate for horseradish peroxidase

For the detection of enzymatic activities after dielectrophoretic immobilization at electrodes, the response of the reaction product is supposed to be constant for a longer period of time. This would allow to determine activities from a single intensity image and to assign intensities to specific electrodes and the activity of enzymes immobilized at those electrodes. Fluorogenic substrates are suitable candidates that fulfill these requirements. One such substrate is DHR, a non-fluorescent derivative of the fluorescence dye Rh123.

Its response to HRP addition was monitored with the FCS unit of a CLSM similar to the measurements of luminol oxidation. The 10 × objective was used again to profit from the larger detection volume and the corresponding higher count rates. HRP and

H_2O_2 were mixed with H_2O in a chambered coverglass, and the oxidation reaction was triggered by addition of the substrate DHR. The count rate increased linearly not only within the first 6 min that were monitored in intervals of 10 s (Fig. 3.12), it continued to increase linearly for at least 100 min (not shown). This trend is the result of the increasing number of Rh123 molecules and the repeated excitation of these fluorescence dyes, which is followed by emission.

The reaction volume was decreased to 10 µL for the subsequent experiment on a microscope slide to mimic the conditions on an electrode chip. HRP and H_2O_2 were again mixed prior to DHR addition. The sample volume contained the same amount of each reactant as in the chambered coverglass. Nevertheless, the count rate increased only little as compared to that in the larger sample volume, and it reached a constant count rate within less than 1 min. Still, this constant value exceeded the maximal count rates obtained from the luminescent reaction of luminol. The fact that the count rate did not increase further might be the result of bleaching effects of the fluorescence dyes. Even so, these results show the suitability of DHR as a substrate to detect HRP activity at electrodes.

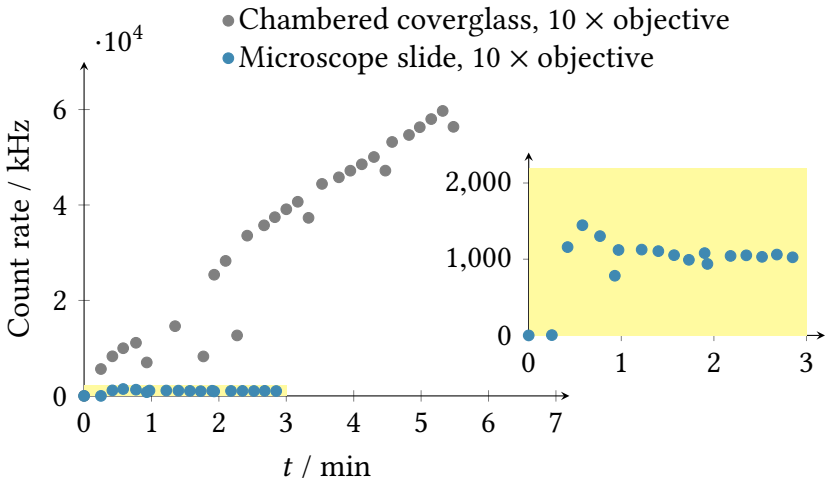

Figure 3.12: Background-corrected count rate of rhodamine 123 fluorescence upon formation by horseradish peroxidase-catalyzed oxidation of dihydrorhodamine 123. The reaction was carried out in different sample carriers (chambered coverglass or microscope slide). Inset: Magnification of the yellow highlighted region.

Furthermore, the auto-oxidation of DHR had to be investigated to be able to reliably assign Rh123 formation to HRP activity. In the literature, oxidation of DHR by H_2O_2 in the absence of enzymes is reported as insignificant [148], and while oxidation by HRP alone occurs at a higher rate, it is still less effective than in the presence of H_2O_2 [131]. Nevertheless, control experiments were performed to rule out factors that could lead to misinterpretation of the fluorescence measurements. First of all, air oxidation

of DHR in solution [149] was mostly prevented by storing the precursor under oxygen free conditions in the dark. Additionally, the DHR solution (Fig. 3.13) was checked for auto-oxidation by fluorescence spectroscopy with excitation at 450 nm. Moreover, the

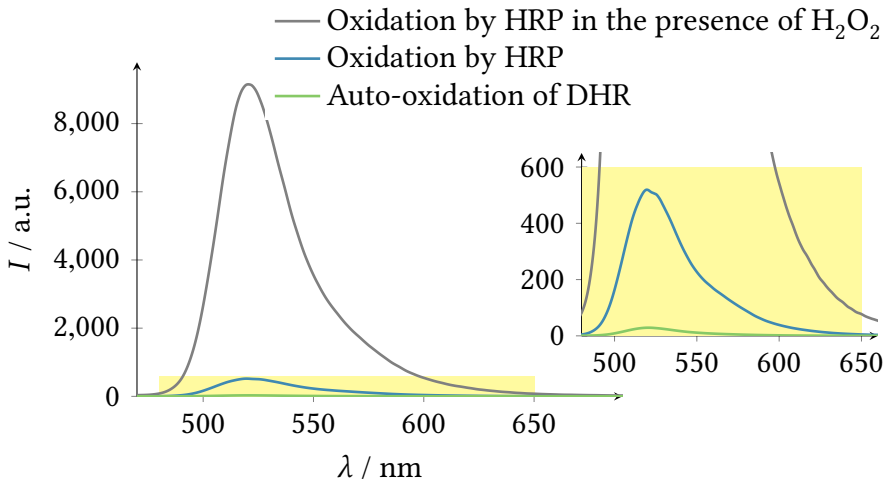

Figure 3.13: Emission spectra of a dihydrorhodamine 123 solution, after addition of horseradish peroxidase, and after subsequent addition of H_2O_2; λ_{ex} = 450 nm. Inset: magnification of the yellow highlighted region.

influence of enzyme addition and subsequent H_2O_2 addition was investigated. H_2O_2 addition lead to a drastic intensity increase, and the solution had to be diluted 1:100 to work within the optimal dynamic range of the spectrometer. The resulting spectrum was renormalized by multiplication by 100 to compare the intensities of the different spectra. The fluorescence intensity increased 18 times upon addition of HRP and further 18 times upon addition of H_2O_2. These measurements demonstrate that auto-oxidation of the DHR solution can be neglected and that the formation of Rh123 is a valid indicator for HRP activity.

3.3.2 Proof of enzymatic activity

Fluorescently labeled HRP was immobilized on a subarray of tungsten nanoelectrodes by applying 10 V at 10 kHz for 20 min. The activity of dielectrophoretically immobilized HRP was demonstrated using the formation of the fluorescence dye Rh123 from its non-fluorescent precursor DHR by enzymatic oxidation in the presence of H_2O_2. The enzymatic reaction was investigated qualitatively using fluorescence intensities of either the HRP label or the product Rh123. The excitation and emission wavelength ranges of the respective filters are separated sufficiently so that after the immobilization step, the fluorescence from the enzyme label was detected exclusively with the corresponding filter set (Fig. 3.14a), whereas no light was detected with the filter set

for Rh123 (Fig. 3.14b).

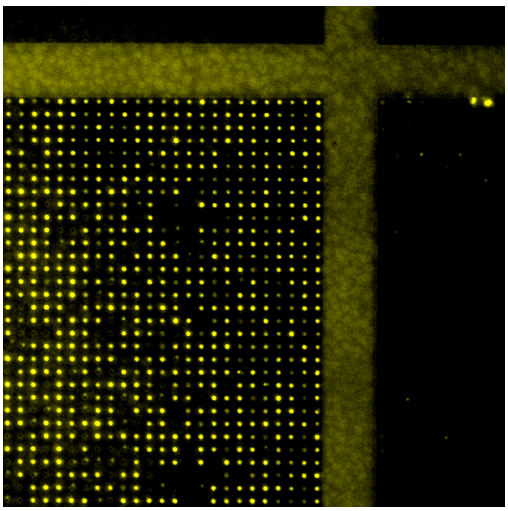

(a) After HRP immobilization; filter set for HRP label.

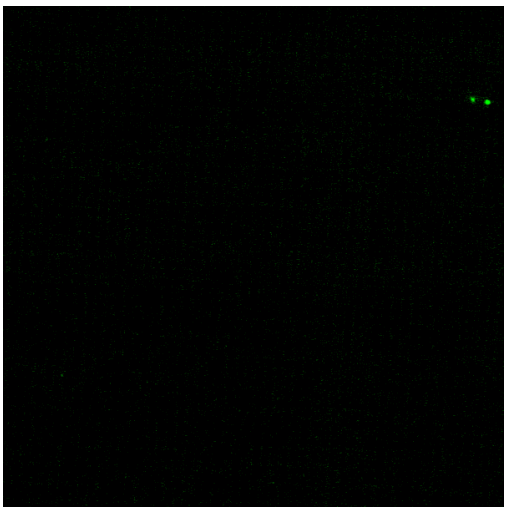

(b) After HRP immobilization; filter set for Rh123.

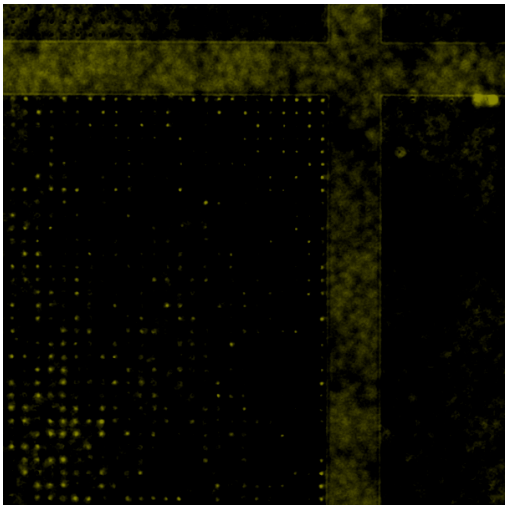

(c) After subsequent oxidation of DHR to Rh123; filter set for HRP label.

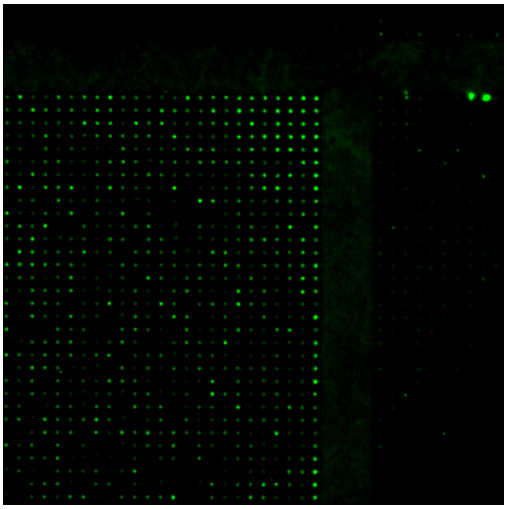

(d) After subsequent oxidation of DHR to Rh123; filter set for Rh123.

Figure 3.14: Fluorescence micrographs of HRP-Oyster-555, immobilized at nanoelectrodes, before and after conversion of dihydrorhodamine 123 to rhodamine 123. Each of the images shows a part of the contacted subarray and smaller parts of the three non-contacted subarrays.

The enzymatic reaction was started with the subsequent addition of the non-fluorescent precursor dye DHR and H_2O_2 as a co-oxidant. The newly formed Rh123 dye lead to fluorescence that could be observed with the matching filter set (Fig. 3.14d). Since the dye was released from the enzyme after oxidation, it freely diffused away from the electrodes causing a strong fluorescent background. To enhance the contrast of the fluorescence micrographs, diffusing dye molecules were removed by rinsing the chip

carefully after a reaction time of not more than 5 seconds. Since the dye molecules adhered stronger to the protein than to the SiO_2 surface, enough fluorescence remained for a relative quantification of the reaction product. The decreasing fluorescence intensity of the enzyme label (Fig. 3.14c) is presumably a consequence of absorption of the excitation light by Rh123 molecules, reducing excitation of the labels.

In addition to the control of DHR auto-oxidation in solution (Fig. 3.13), a direct control was run on an electrode chip by mixing DHR and H_2O_2 in the absence of enzyme. Only a slight increase of the background fluorescence was observed. This background was subsequently subtracted to evaluate the result of enzymatic activity alone. The remaining fluorescence measured in the emission range of Rh123 on the electrode chips with immobilized HRP can thus be reliably accounted to active enzymes, giving proof of a preserved enzymatic activity of HRP after dielectrophoretic immobilization.

3.3.3 Quantification of enzyme efficiency

The fluorescence intensities after the immobilization step and after formation of Rh123 were used as a basis for quantification. Enzyme efficiency was investigated for HRP that had been immobilized at different voltages. The microarray evaluation software *GenePix Pro* was used to determine mean fluorescence intensities at the electrodes, since it not only provides an automated detection of ROIs, but also allows to include ROIs that show no fluorescence.

Enzyme immobilization

The effect of the applied voltage on immobilization of HRP and its enzymatic activity was investigated with voltages ranging from 1 V to 20 V and for a constant experiment duration of 20 min. The frequency of 10 kHz was chosen according to the results of the previous optimization to circumvent electrolysis of water and to minimize fluid flows.

As a negative control, an electrode array was incubated with a solution of the fluorescently labeled HRP without field application for 20 min. Adhesion of the enzymes on the SiO_2 surface and on the tungsten electrodes due to non-specific interactions led to a general rise in background fluorescence with no preference of the enzymes for neither tungsten nor SiO_2.

For the evaluation of the distribution and of the amount of dielectrophoretically immobilized enzymes, fluorescence intensities from the enzyme labels in ROIs located at the electrodes were determined. Intensities were background corrected according to Eq. (2.7). At 1 V only an increase in background fluorescence similar to the negative control was observed with no distinction of the electrodes. At 5 V enzymes covered

about 25 % of the electrodes. Averaging over all 3600 electrodes that are visible in the micrograph yielded a background corrected average intensity $I_{av} = 0.10$ (Fig. 3.15). If only those electrodes with intensities above the background level were considered, the intensity amounted to $I_{av} = 0.35$. An even distribution of enzymes on nearly all electrodes was achieved at 10 V (Fig. 3.14a) and 20 V, i.e., only few electrodes were not covered by enzymes, and the standard deviations amounted to 19 % or 20 % for the respective experiments. From both experiments, 2250 electrodes could be evaluated giving average intensities of $I_{av} = 0.35$ and $I_{av} = 0.14$, respectively. Consequently, the amount of immobilized enzymes per electrode is similar for the experiments at 5 V and 10 V. The intensity drop at 20 V, where an increased amount of immobilized enzymes would be expected, is presumably the result of intensified fluid flows (see section 3.2.2) that interfere with dielectrophoretic attraction towards the electrodes. The high voltage leads to fast accumulation of enzymes at the electrodes, where enzyme aggregates are formed, probably due to the increased local concentration. These aggregates are then dragged away by the fluid flow, further reducing the amount of enzymes immobilized at the electrodes.

Enzyme activity

For the examination of the enzyme activity on the different electrode chips, DHR and H_2O_2 were mixed on the chips. As a negative control, DHR and H_2O_2 were also added to an electrode chip without immobilized enzymes. After rinsing the chips with water, enzyme activity was evaluated using the fluorescence of the newly formed dyes located at the electrodes, similar to the quantification of immobilized enzymes. For this it is

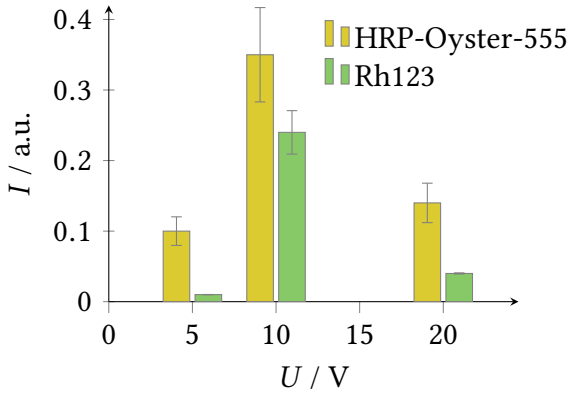

Figure 3.15: Amounts of immobilized HRP-Oyster-555 or of the oxidation product rhodamine 123 in dependence of the voltage used for dielectrophoretic immobilization.

assumed that the relative amounts of adhered Rh123 remain comparable despite the additional rinsing step. Background corrected average intensities of $I_{av}(5\,V) = 0.01$,

$I_{av}(10\,V) = 0.24$, and $I_{av}(20\,V) = 0.04$ were determined (Fig. 3.15), showing the same trend as the intensities of the enzyme labels with the strongest signals on the electrodes where HRP had been immobilized by applying 10 V. These results confirm the positive correlation of Rh123 formation and the amount of immobilized HRP.

Enzyme efficiency

Enzyme efficiency (*EE*) is defined here as the amount of newly formed Rh123 in relation to the amount of immobilized enzymes (Eq. (2.7)). From the background corrected fluorescence intensities, values of $EE(5\,V) = 0.1$, $EE(10\,V) = 0.7$, and $EE(20\,V) = 0.3$ were calculated, respectively (Fig. 3.16). These values take into account the differing coverage of electrodes with enzymes after the immobilization step and the actual activity of those enzymes. According to this, the best enzyme efficiency is obtained after dielectrophoretic immobilization of HRP at 10 kHz and 10 V.

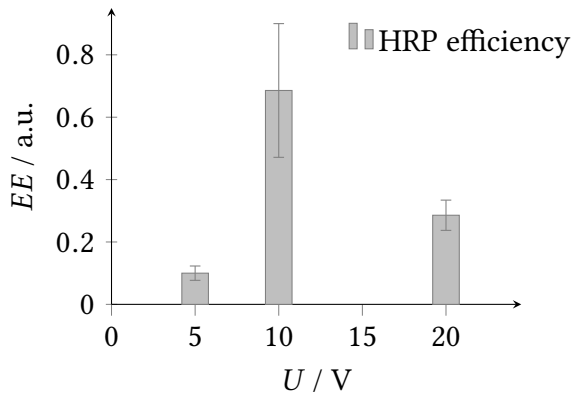

Figure 3.16: Enzyme efficiency in dependence on the voltage used for dielectrophoretic immobilization of HRP-Oyster-555.

3.3.4 Long-term stability

For biosensing devices it is important that the biomolecules that are responsible for the sensing reaction remain active from the time of device production until the actual application. The development of HRP activity after immobilization was investigated over a time span of 104 days (Fig. 3.17, data set 1). HRP was immobilized under optimized conditions (10 kHz, 10 V, 10 min), and the dry chips were stored at room temperature. On day 1, DHR and H_2O_2 were mixed on the chip and rinsed after 2 min. The fluorescence intensities at the electrodes were determined from fluorescence micrographs using the *Gwyddion* software. The standard deviation of the intensities at electrodes within one chip was calculated and used as error bars in Fig. 3.17. The experiments were repeated with a data set that spanned 51 days (Fig. 3.17, data set 2).

In both data sets, a decrease of activity was observed that roughly followed an exponential decay function ($I_1 = (2.4 \pm 0.5) \cdot 10^{-5} \cdot \exp(-x/(5.8 \pm 4.3)) + (1.5 \pm 0.5) \cdot 10^{-5}$, $R^2 = 0.76$: $I_2 = (2.0 \pm 0.8) \cdot 10^{-5} \cdot \exp(-x/(3.6 \pm 4.6)) + (2.6 \pm 0.6) \cdot 10^{-5}$; $R^2 = 0.43$; errors were calculated as the standard deviations of the fit parameters). The initial activ-

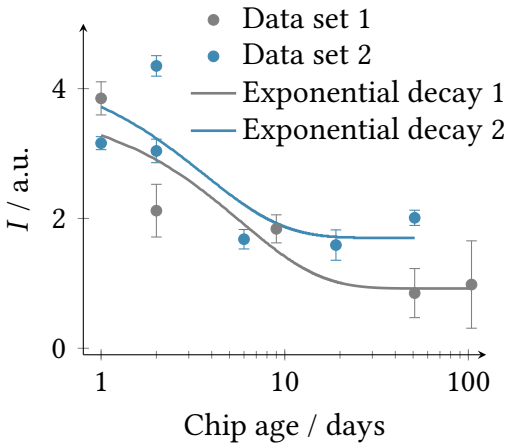

Figure 3.17: Long-term development of horseradish peroxidase activity when immobilized on nanoelectrodes; storage at room temperature, dry, air exposed, in the dark.

ity was about halved after less than 3 days. It further decreased rapidly to a background level, which was determined by leveling the intensities obtained from the negative controls conducted with BSA for both data sets individually. Data set 1 reached this level after approximately two weeks, data set 2 already on the sixth day. The higher intensity measured within data set 2 and on day 51 in particular cannot be assigned with certainty to enzymatic activity. It is likely that it merely indicates the reproducibility deviation and the uncertainty of the measurements, which was calculated from the double determination on day 2 (data set 2) as the ratio of standard deviation and mean value, and which lies in the range of ± 20 %.

3.3.5 Discussion

Up to this date, the only report on enzymatic activity in combination with DEP was an indirect approach by Kumemura et al. who generated and manipulated liquid droplets containing β-galactosidase and fluorescein di-β-D-galactopyranoside, respectively. In their study, they also demonstrated enzymatic reactions after fusion of droplets [150].

In this chapter, the direct manipulation of enzymes and their activity after permanent dielectrophoretic immobilization has been demonstrated for the first time. An efficient dielectrophoretic immobilization protocol was developed for HRP enzymes, and a suitable substrate was identified for the investigation of its catalytic activity. The non-fluorescent precursor dye DHR was successfully oxidized to the fluorescence

dye Rh123, thus demonstrating the functionality of dielectrophoretically immobilized HRP. The applied voltage influenced the distribution and the amount of enzymes that were immobilized. The formation of Rh123 depended on the amount of immobilized enzymes, and in the present electrode configuration, it was most effective after immobilization of HRP at 10 kHz and 10 V.

The chemiluminescent substrate luminol, which was also examined, has the potential to allow monitoring with time and spatial resolution. However, a continuous-flow system would be advisable for such examinations, as microscopic detection after the preparation of the electrode chip was not possible due to the fast luminescent reaction.

The presented results demonstrate AC DEP as a simple and promising method for the immobilization of functioning enzymes, which is expected to be applicable to any enzyme or protein without covalent modifications of the molecule or substrate. If an integration of this method in sensing devices is envisaged, the decrease of enzymatic activity within a few weeks during storage, which is a common challenge also with other immobilization methods [151] and also in solution [120], has to be considered. Although some residual fluorescence that exceeded that of the negative controls could be measured at the electrodes after storage of the chips for time spans up to two weeks, the exponential intensity decrease advises fresh preparation of chips with immobilized enzymes for best results. While short applicability times might be sufficient for sensors used in research laboratories or for prototypes, this is unfavorable for commercial biosensing devices that should preferably be storable for several months.

Modifications of the electrode might help to retain the functionality of immobilized biomolecules for a longer period of time. One possibility is to use alternative electrode materials, which might be more biocompatible than bare metal electrodes and, hence, better suited for sensing devices involving immobilized proteins. Titanium nitride or titanium silicide for example are materials that can easily be incorporated into the CMOS fabrication process. Another possibility is to cover the electrode with, e.g., a thin layer of SiO_2 or a self assembled monolayer of spacer molecules [152] to shield the proteins from the metal surface. Moreover, specific storage conditions [153], e.g. in buffer solutions with additives, at low temperatures, in dry state with desiccants or *in vacuo*, are possible strategies to prolong the functionality of immobilized enzymes.

3.4 Alignment and aligned immobilization in AC electric fields

Among the various strategies that have been developed to achieve specific orientations of particles or macromolecules in electric fields is the alignment between a pair

of opposing electrodes [73] or IDE [52]. The main challenge concerning molecules that cannot be visualized directly by optical methods, however, is the determination of the orientation. On top of this, positive and negative controls are needed to validate the setup and the experimental procedure. These control samples, however, require statistical distributions or oriented molecules themselves. In this section, suitable samples and controls for aligned immobilization are identified. An experimental procedure for the investigation of oriented chromophores is developed. Different polarizer configurations of the fluorescence microscope setup are compared and validated using the control samples. With the optimized setup and evaluation protocol, the alignment of lambda-DNA and of eGFP at IDE is investigated.

3.4.1 Development of an experimental setup

With a fluorescence microscope setup several approaches are possible to orientational investigations of fluorophores: The excitation light can be polarized, polarized emission light can be detected, or a combination of polarized excitation light and polarized detection can be used. This is easily employed by insertion of polarizers into the beam path (see section 2.2.10.). The different configurations were compared using the positive control sample that consisted of acridine orange molecules embedded in a liquid crystal, and aligned in an AC electric field.

Polarized excitation and polarized emission

Two polarizers in parallel configuration were inserted into the excitation and emission path, respectively. The polarizer orientations remained fixed throughout all measurements, while the chip with the sample was rotated. For each chip orientation β, a fluorescence micrograph was acquired. The same ROIs were selected for evaluation in all images. The measured fluorescence intensity is expected to stay constant for statistically oriented samples. For samples with a preferential orientation, an intensity modulation according to a $\sin^4$-function is expected, since both excitation and emission follow $\sin^2$-functions.

The data from acridine orange in a liquid crystal (Fig. 3.18) could be fitted very well with a $\sin^4$-function ($R^2 = 0.95$), proving a preferential orientation of the fluorescence molecules. For a fully aligned sample, one would expect no fluorescence intensity for orientations perpendicular to the polarizer orientation. The modulation depth was calculated as $Q = \frac{I_{max}-I_{min}}{I_{min}} = 0.20$. The background of approximately 170 is composed of a constant background that is caused by dark current and camera noise (see section 2.2.10) and of a variable background that indicates incomplete alignment of the

sample or imperfect polarizers. Both factors, incomplete alignment and imperfect polarizers, lead to excitation of an ensemble of fluorophores with a broader variation in orientation angles, thus preventing an intensity reduction to zero.

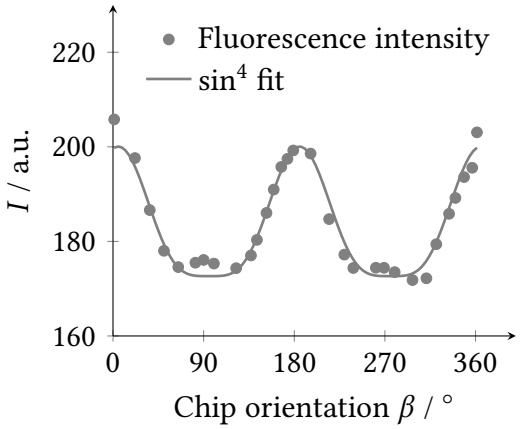

Figure 3.18: Fluorescence intensities I of the positive control acridine orange, aligned in a liquid crystal, in dependence on the chip orientation β. Intensities were detected with parallel polarizers and fitted by a $\sin^4$-function.

This configuration with two polarizers is favorable for accurate measurements of the molecules' orientation, since the position of the maxima of a $\sin^4$-function can be determined more precisely than those of a $\sin^2$-function from a single-polarizer measurement. On the downside, light is filtered by two polarizers in this setup, and light intensity is reduced twice. After each repositioning the chip, the focus needs to be adjusted while alluminating the sample. This might be problematic for samples that exhibit weaker fluorescence or that are prone to fluorescence bleaching.

Polarized emission

Unpolarized excitation light comprises all polarization planes equally. In a sample with statistically distributed chromophore orientations, the emission is also unpolarized. In samples with aligned chromophores, however, the emission is polarized along the TDMs of the chromophores. This polarized emission can be determined by rotating a polarizer in the emission light path.

Acridine orange molecules were aligned in liquid crystals, and the sample was excited with non-polarized light. Fluorescence intensities were measured using a polarizer in the emission beam that was rotated in 22.5°-steps, leading to a periodic intensity modulation (Fig. 3.19) with a ratio $Q = \frac{I_{max}-I_{min}}{I_{min}} = 0.05$. This procedure was repeated for two further chip orientations to ensure that the polarizing effect is caused by the sample. In that case the position of the maxima is shifted for the different sample orientations, whereas polarizing artifacts of the setup would appear at the exact same

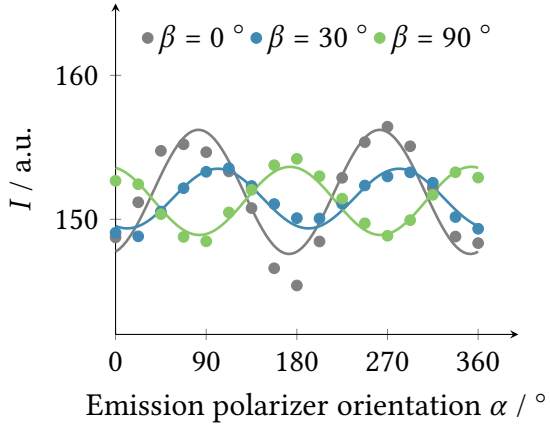

Figure 3.19: Fluorescence intensities I of the positive control acridine orange, aligned in a liquid crystal, in dependence on th emission polarizer orientation α for different chip orientations β (symbols), and corresponding $\sin^2$ fits (solid lines).

position regardless of the sample position.

The intensity data were fitted by $\sin^2$-functions (with fixed periods of 180°) for each chip orientation β. Periodic intensity fluctuations were obtained as a result of the polarized emission of aligned acridine orange molecules. The shifted phases for each sample orientation prove that the cause for the intensity modulation stems from the sample. An imperfect alignment, however, is indicated again by the background of approximately 145. This background is the result of fluorescence by chromophores with deviating orientations in addition to a fix background. Nevertheless, these results confirm the general applicability of an experimental setup with polarized emission for the determination of fluorophore orientations.

Polarized excitation

If the sample is illuminated with polarized light, only those chromophores that are in accordance with the polarization are excited. The emitted light is detected in its full intensity without reduction by the passage through a polarizer.

The fluorescence intensities of acridine orange molecules were measured using polarized excitation light while rotating the polarizer orientation. This procedure was repeated for five sample orientations β to be able to differentiate between effects from the sample and polarizing artifacts from the optical setup. Additionally, the sample orientations of 1° and 181° are identical so that the agreement of the two data sets serves as a control for reproducibility and reliability of the data. The intensity variation due to polarizer rotation exhibited a modulation depth of $Q = 0.16$ for the chip orientation 1°.

All data was fitted by $\sin^2$-functions (with fixed periods of 180°) (Fig. 3.20a). The resulting periodic intensity fluctuations were expected from the dependence of ab-

sorption efficiency on the polarization of the excitation light. The fit equations from the different chip orientations yield shifted phases that correlate very well with the chip orientations (Fig. 3.20b). The linear fit ($\rho = (1.05 \pm 0.09) \cdot \beta + (-13.42 \pm 9.94)$; $R^2 = 0.97$) has a slope of 1.05, which is very close to the ideal value of 1 for a shift of the phase offset upon chip rotation by the same angle. The y-intercept would theoretically be 0 for a preferential orientation of acridine orange precisely parallel to the electric field. The deviation from 0 and its relatively large standard deviation might be the result of uncertainties in the determination of the orientation angle of both the chip and the polarizer. The chip orientation was determined from fluorescence micrographs, where the angle between the electrode edges and the image margins was measured. Here, the uncertainty is assumed to be less than ± 1°. Consequently, the uncertainty of the polarizer orientation is the decisive factor contributing to the deviation of the y-intercept from 0. This uncertainty was estimated to be no more than ± 5° from the standard deviations of the phase offsets obtained from the $\sin^2$ fits. It is also possible that the polarizer orientation uncertainty additionally includes a fix offset.

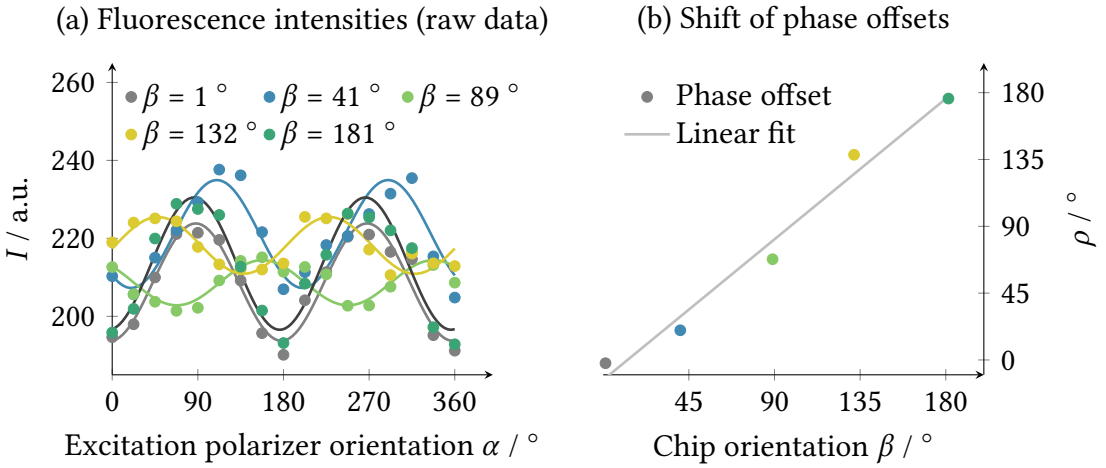

Figure 3.20: Fluorescence intensities I of the positive control acridine orange, aligned in a liquid crystal, in dependence on the excitation polarizer orientation α for different chip orientations β (symbols), and corresponding $\sin^2$ fits (solid lines). (b) Phase offsets ρ of the $\sin^2$ fits in dependence of the respective chip orientation (symbols) and corresponding linear fit (solid line).

Similar to the configuration based on the polarized detection of emission light, this experimental setup with an excitation polarizer is suited for orientational investigations of fluorophores. The direct comparison of the two configurations favors the excitation polarizer due to its higher modulation depth. Compared to the setup with two polarizers, the evaluation requires less effort, and the intensities are reduced by only one polarizer. For these reasons, polarized excitation was applied for all further orientational investigations.

Validation of the selected setup using a negative control

The microscopic setup with polarized excitation light proved most suitable for the orientational investigation of fluorescence molecules. This setup was validated further using a negative control. A solution of eGFP molecules was chosen to get a negative control that is as close to the sample of interest as possible. The eGFP solution was filled into the sample chamber of an electrode chip, and the fluorescence micrographs were taken with the electrode array in focus. Four data sets were acquired following the previously described procedure with polarized excitation light. The ROI for evaluation was set along one of the electrode fingers. Notably, all four data sets exhibited periodic intensity modulations (not shown), although no variations were expected from such a sample with statistically distributed fluorophores. Hence, the modulations were referred to a polarizing effect of the optical setup. This effect was taken into account by normalizing the intensity data with reference data (Eq. (2.8), see also section 2.2.10). The resulting corrected intensities show nearly no modulation for the negative control. The weak modulation at 0° hints towards some residual polarization of the microscope optics that has not been removed by the correction procedure. Small as these artifacts are, they might still disguise modulations from samples that are not perfectly aligned, or they might feign alignment where there is none. To exclude any ambiguity, the following fluorescence measurements were carried out at several chip orientations.

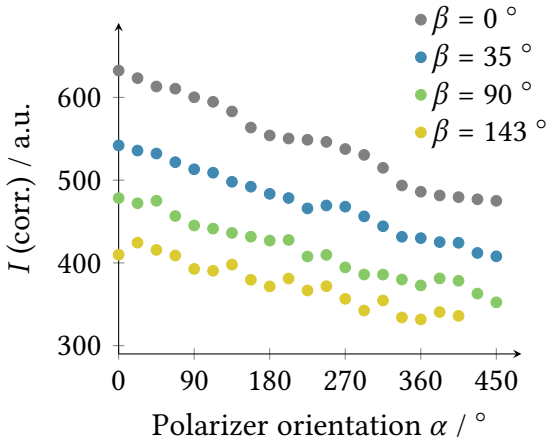

Figure 3.21: Corrected fluorescence intensities of the negative control, eGFP in solution, in dependence on the polarizer orientation α for different chip orientations β.

The decrease from one image (data point) to the next is almost constant. From one set of measurements at one chip orientation to the next, intensity increased probably by fluorescence recovery due to diffusions, since the interval between sets was around 5 min as compared to 5 s to 10 s between images within a set. If necessary, this intensity

decrease can be considered using a linear or an exponential fit.

3.4.2 Alignment of DNA

Alignment of DNA strands between interdigitated electrodes

Lambda-DNA was stained with PicoGreen, a common fluorescence stain for dsDNA, and a frequency of 1 MHz and a voltage of 25 V was applied to aluminum IDE with gaps of 22.2 µm to achieve DNA alignment between the edges of adjacent IDE. The alignment of DNA strands was visualized in real-time using fluorescence microscopy. Fluorescent bands between the electrodes were observed that spanned the electrode gaps (Fig. 3.22). Additionally, bright fluorescent spots accumulated along the IDE edges.

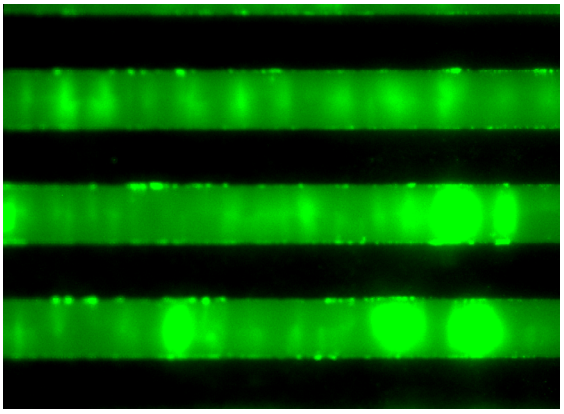

Figure 3.22: Stained DNA strands (bright green) stretched between interdigitated electrodes (black) in an AC electric field; fluorescence micrograph.

These spots are supposedly caused by coiled DNA. The fluorescent bands stem from stretched DNA strands that were aligned between the IDE. The intensity within the bands is not evenly distributed. The brightest areas are located in the center of the electrode gaps where the bands appear to be wider than at the electrode edges. Since the electrode gap of 22.2 µm exceeds the length of stretched lambda-DNA (16 µm), only one end of the DNA strands can be attached to an electrode edge while the other end is stretched towards the adjacent electrode without making contact. The free end is more prone to thermal movement and fluid flow, leading to broader bands. The higher intensity in the center of the electrode gaps is probably the result of overlapping DNA strands.

Orientation of PicoGreen in dsDNA

PicoGreen binds to DNA by several binding mechanisms including intercalation between the base pairs [154]. By stretching and aligning DNA strands between IDE,

the base pairs form defined, parallel ladder steps. As a result of intercalation, the dye molecules are also aligned in parallel. This alignment can theoretically be detected by measuring the fluorescence modulation in dependence of the excitation polarization. The stretching and alignment of DNA strands in AC electric fields, however, is a dynamic process. They are not attached permanently at the electrode edges but can move along the edges, they can be released from the electrodes and attracted anew. Consequently, the ROIs for orientational investigations have to be selected carefully.

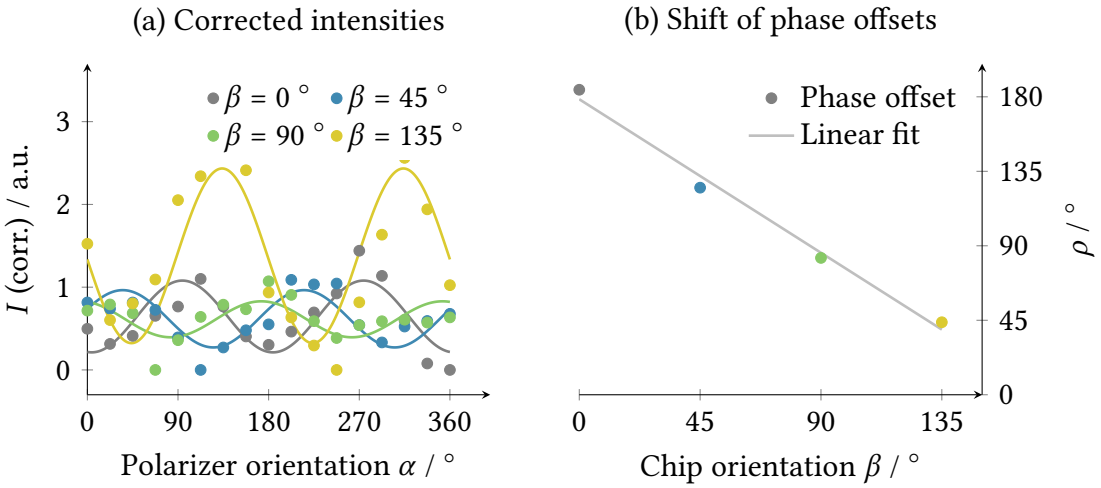

Figure 3.23: (a) Corrected fluorescence intensities of intercalated PicoGreen molecules in dependence on the polarizer orientation α for different chip orientations β (symbols), and corresponding fits (solid lines). (b) Phase offsets ρ of the $\sin^2$ fits in dependence of the respective chip orientation (symbols) and corresponding linear fit (solid line).

Polarized light fluorescence intensities of PicoGreen were measured at four different chip orientations: 0°, 45°, 90° and 135°. For each chip orientation, the polarizer and, thus, the orientation of the excitation polarization, was rotated in 22.5°-steps from 0° to 360°. A block of DNA-strands that was visible throughout all four data sets was selected as ROI. Their mean intensities show periodic fluctuations in dependence on the polarizer orientation α and an overall decrease of fluorescence intensity. The intensity decrease by photobleaching was accounted for by subtracting a linear approximation from each data set (Eq. (2.10)). Subsequently, $\sin^2$ functions were fitted to the data (Fig. 3.23a). The relatively high intensities obtained from chip orientation 135° are probably the result of newly formed DNA bands in the selected ROI. The phase offsets from the $\sin^2$ functions correlate linearly with the chip orientation β ($\rho = (-1.03 \pm 0.07) \cdot \beta + (178.54 \pm 6.25); R^2 = 0.98$). The negative slope is caused by rotation of the polarizer in the opposite direction than in the acridine orange measurements. The absolute value for the slope of 1.03 means that the intensity functions are shifted upon chip reorientation by the same angle, which can only be the case for

aligned samples. From the position of intensity maxima with respect to the polarizer orientation and the chip orientation follows that PicoGreen dyes are oriented perpendicular to the long axis of the DNA strands, which is in agreement with the concept of intercalation. These results demonstrate the suitability of the newly developed method for the determination of fluorophore orientations.

3.4.3 Aligned immobilization of proteins

eGFP was selected as a model protein for aligned immobilization experiments based on its exceptional structure and its fluorescence properties. The chromophore lies on the inside of the barrel-like protein structure, and it is stabilized in its conformation by covalent and hydrogen bonds. The orientation of the chromophore with respect to the overall protein structure can be deduced from the orientation of the TDM, which characterizes the interaction with light excitation and emission. On top of this, the fluorescence emission itself serves as an indicator for structural integrity and proper folding, since the protein is only fluorescent in its native state.

Immobilization at interdigitated electrodes

IDE were employed for aligned immobilization experiments of eGFP because of their high tangential electric field component as compared to the nanoelectrode arrays. In the latter, an upright orientation of the protein structure would be expected (Fig. 3.24a-c). As a consequence of the rotational freedom around the protein's long symmetry axis, the orientation of the TDM would be statistically distributed around the microscope optical axis even for perfectly aligned proteins. With IDE, however, proteins are expected to lie flat or acute-angled on the surface (Fig. 3.24d-f), where differences in TDM orientations would lead to more or less effective absorption and emission depending on the polarization of the excitation light. The resulting intensity variations would be measurable despite rotational freedom of the molecule.

The first experiments with eGFP were conducted on ITO IDE that exhibited narrowing electrode fingers with widths below 20 µm. The electrode material ITO was thought to be advantageous for fluorescence measurements due to its optical transparency and the lack of reflexions. Two different behaviors were observed for eGFP depending on the applied frequency. Positive DEP occurred at lower frequencies ($\approx$ 10 kHz), where eGFP accumulated at the electrode tips and along the electrode edges in proximity to the tips. Higher frequencies (> 1 MHz) lead to eGFP streamlines on the electrode centers that were directed outwards. After switching off the electric field, the proteins diffused away instantly. Consequently, the orientational investigation as

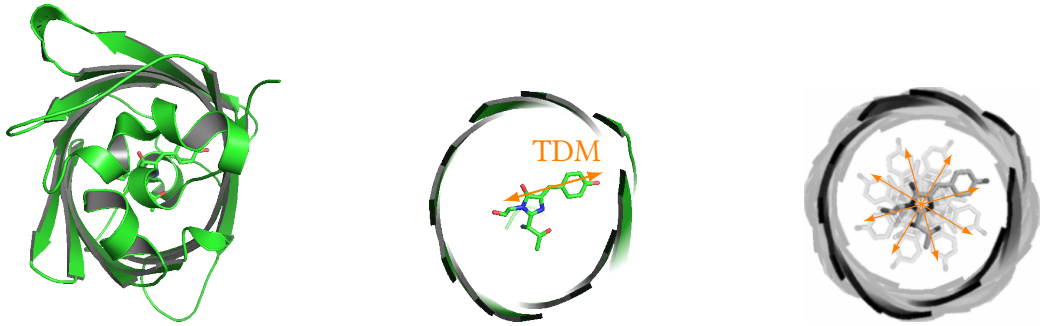

(a) Ribbon diagram of the eGFP structure, bottom view.

(b) Protein structure cut open to reveal the chromophore.

(c) TDM orientations for rotational freedom of the protein.

(d) Ribbon diagram of the eGFP structure, side view.

(e) Protein structure cut open to reveal the chromophore.

(f) TDM orientations for rotational freedom of the protein.

Figure 3.24: Transmission dipole moment (TDM) orientations in eGFP molecules as expected from X-ray crystallographic data for proteins with rotational freedom around the longitudinal axis. Perpendicular (a-c) or parallel (d-f) immobilization relative to the surface.

described in the preceding sections could not be conducted.

On nanoelectrode arrays, the proteins BSA or HRP had been immobilized permanently. There are three critical factors in that these nanoarrays differ from the ITO IDE: electrode arrangement, their material and dimensions. The few existing reports on reversible or permanent dielectrophoretic immobilization of proteins in dependence on the applied field strength [46, 48] hint towards the last factor being decisive. As a consequence, tungsten IDE with widths of 750 nm and gaps of 450 nm were chosen for the following experiments. eGFP accumulation was investigated by fluorescence microscopy in the frequency range between 1 kHz and 10 MHz with voltages up to 37 V. Low frequencies (< 10 kHz) were unfavorable due to the formation of protein aggregates on the electrode centers with heterogeneous orientations. Fluid streaming that prevented protein immobilization occurred preferentially at higher frequencies (> 1 MHz) and higher voltages. At intermediate frequencies (100 kHz - 1 MHz), accumulation at the electrode tips starting at a threshold voltage of approximately 5 V was observed. Upon turning off the electric field, proteins diffused away. No fluorescence

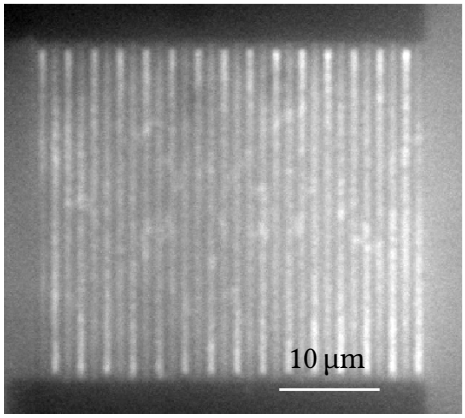

(a) Electrode chip with eGFP during field application.

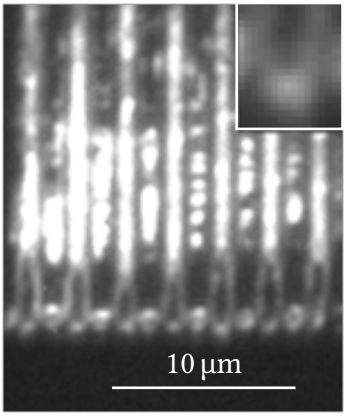

(b) Section of a rinsed electrode chip with eGFP after field application. Inset: Magnification of an electrode tip.

Figure 3.25: Reversible (a) and permanent (b) immobilization of eGFP at interdigitated electrodes; fluorescence micrographs.

could be detected at the electrode tips after rinsing the chips. In the range of 7 V to 10 V (100 kHz), protein accumulation occurred not only at the electrode tips but also along the electrode edges close to the tips, and additionally on the centers of the electrodes' surfaces starting at about 2 µm distance from the tips (Fig. 3.25). Upon turning off the electric field, proteins remained immobilized even after rinsing.

Orientation at electrode tips and edges

The orientation of immobilized eGFP molecules was derived by the orientation of its chromophore, which was determined through the TDM. First, ROIs at the electrode tips and edges were evaluated. At those ROIs, immobilization was expected as a result of positive DEP. Fluorescence micrographs with polarized excitation light were acquired of a dry electrode chip. The polarization of the excitation was varied stepwise from 0° to 450°, and for each 22.5° step a fluorescence micrograph was acquired. For evaluation, four ROIs were selected at the electrode tips and at the edges, respectively. Fluorescence intensities of those ROIs were averaged and subsequently corrected (see section 2.2.10). The data could be fitted very well by $\sin^2$-functions (Eq. (2.9)), which indicates preferential orientations in both ROIs. The resulting functions have phase offsets of 78° for the tips and −5° for the edges, respectively (Fig. 3.26), that means they are shifted by 83° to each other. This shift can only be interpreted as the angle between the average orientation of eGFP molecules in the two ROIs. This is in agreement with the directions of the electric field at the electrode edges and at the tips, which are orthogonal to each other in those regions. The deviation from exactly 90°

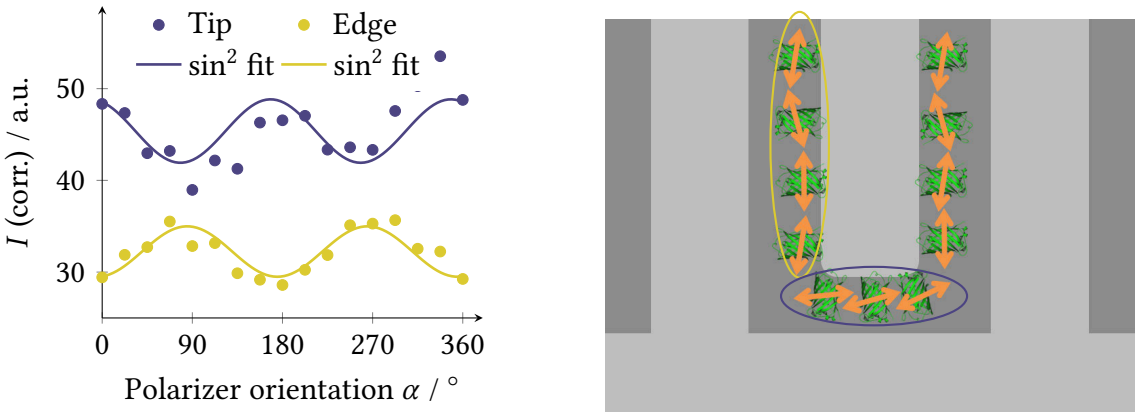

(a) Fluorescence intensities.

(b) Scheme of eGFP orientations.

Figure 3.26: Corrected fluorescence intensities of eGFP immobilized at the tips or along the edges of interdigitated electrodes, and scheme of the corresponding protein orientations.

is probably caused mainly by the rounded electrode tips and asymmetries due to limited photolithographical resolution. Further, minor contributions to the deviation are uncertainties in the determination of the orientation angle of the chip and the polarizer, which were assumed to be less than ± 1° or ± 5°, respectively. Moreover, a fix offset of the polarizer orientation is possible in addition to the uncertainty in adjusting the orientation angle. From the phase offsets an orientation of the chromophores' TDMs perpendicular to the electric field can be deduced. Consequently, the cylindrical protein structures are aligned with their longitudinal axes parallel to the electric field.

Orientation on electrode centers

The accumulation on the electrode centers was assumed to be the result of in indirect field effect that moves the fluid towards the electrode centers and carries the molecules along. Surprisingly, the fluorescence intensity in these regions was higher than at the edges and at the tips indicating higher amounts of immobilized proteins. This allowed the acquisition of several data sets for an expanded evaluation procedure. The chip was rotated after the acquisition of a data set with polarizer rotation from 0° to 450° in 22.5° steps. Thusly, polarizing effects caused by the optical setup could be ruled out reliably. By rotating the chip and thereby rotating the sample, effects caused by the sample upon rotation of the polarizer were shifted, whereas effects caused by the setup appeared at fix polarizer orientations. This evaluation protocol required a series of about 100 fluorescence micrographs and as a consequence, fluorescence bleaching lead to a constant decrease in fluorescence intensity in the course of data acquisition. This fluorescence bleaching was taken into account by fitting a monoexponential func-

tion (Eq. (2.11)) to the corrected data (Fig. 3.27). All six data sets were included in this fit as the images had been acquired consecutively with only short additional illumination times between the different chip orientations. The resulting fit parameters I_0, d, I_∞ were then used as start values for the intensity fits within the separate data sets according to Eq. (2.13). Here, the parameter boundaries were allowed to vary within the standard deviations of the initial fit parameters. The intensity data sets could be fitted successfully.

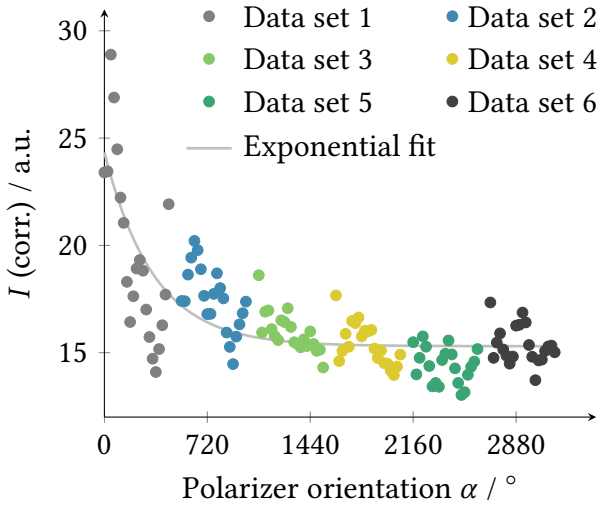

Figure 3.27: Corrected fluorescence intensities of immobilized eGFP in dependence on the polarizer orientation α, measured for six consecutive data sets (symbols). The exponential function (solid line) was fitted to the data to account for fluorescence bleaching.

The data sets each exhibit intensity maxima with a period of 180° (Fig. 3.28a) that is caused by polarizer rotation, which results in a repetition of the plane of polarization every 180°. Rotation of the chip causes a shift of intensity maxima. As the IDE have nearly the same orientation on chip orientations 2° (gray) and 183° (dark gray), the polarizer orientation angle is the same for their intensity maxima. These matching angles further confirm the procedure's validity.

The shift of the intensity maxima positions can be seen more clearly in Fig. 3.28b, where the shift of the phase offsets is displayed in dependence on the chip orientation. The strong linear correlation ($\rho = (0.99\pm0.08)\cdot\beta+(-9.34\pm8.41); R^2 = 0.97$) with a slope of 0.99 ± 0.08 clearly indicates a sample with preferentially oriented chromophores. As explained earlier, a slope of 1 results from the rotation of the sample, which causes a shift of the polarizer orientation for maximum intensity by the same amount – even in the case of unintended polarization effects introduced by the optics. The y-intercept of (−9.34±8.41) is similar to the one obtained from the fit to acridine orange phase offsets (−13.43 ± 9.94). Both intercepts deviate to negative values, indicating a fix deviation

of the polarizer orientation.

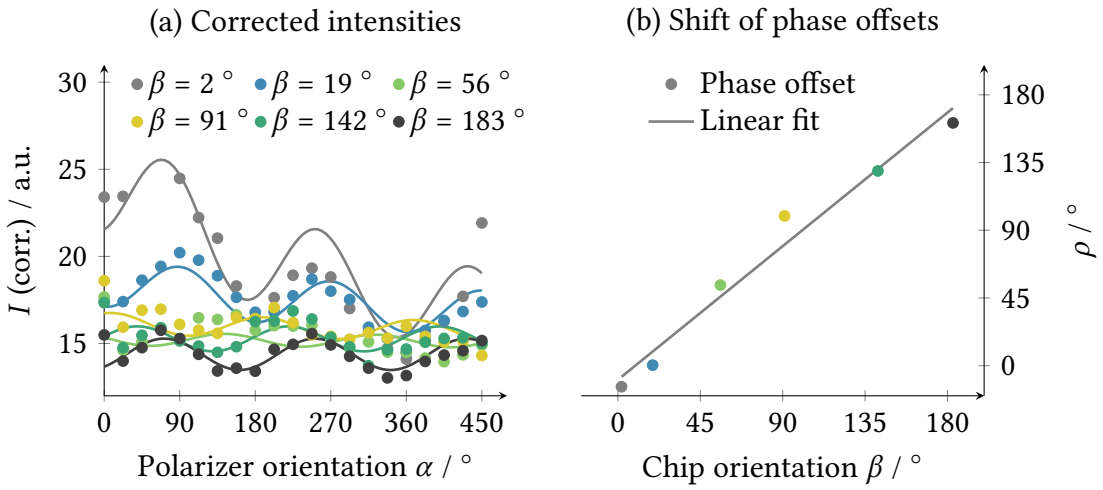

Figure 3.28: (a) Corrected fluorescence intensities of immobilized eGFP in dependence on the polarizer orientation α for different chip orientations β (symbols), and corresponding fits (solid lines). (b) Phase offsets ρ of the $\sin^2$ fits in dependence of the respective chip orientation (symbols) and corresponding linear fit (solid line).

Degree of alignment

The maximal possible modulation of fluorescence intensity in this optical setup was determined using two different polarizing standards: a reflecting polarizer grid, and the fluorescent dye acridine orange dissolved in a liquid crystal and being oriented by the guest-host effect in an AC electric field [65]. The polarizer grid was chosen for its perfectly aligned grid structure. However, it does not emit light but only reflects it, so that the absolute intensity modulation is very low. In contrast, the fluorescence intensity of acridine orange is high and produces a higher modulation amplitude. On the downside, while its degree of alignment should theoretically be close to perfect, the true value is unknown.

The minimal and the maximal intensity was determined for each sample, and a ratio Q was calculated to allow comparability in spite of the varying absolute intensities: $Q = \frac{I_{\max} - I_{\min}}{I_{\min}}$. As both standards led to the same ratio, it appeared reasonable to define their degree of alignment as 100 %. Randomly oriented eGFP in solution exhibited approximately 4 % modulation that might be caused by residual polarization effects of the optical setup. Immobilized eGFP at the electrode tips, edges and on the electrode centers yielded modulations of 51 %, 57 % and 61 % (Table 3.2), respectively, proving a preferential orientation of the immobilized proteins. Several factors are responsible for this reduction in modulation depth as compared to ideally oriented fluorophores. The

main contribution to this reduction stems from the rotational freedom around the protein's longitudinal axis. As the chromophore is oriented not exactly perpendicular to the protein structure, its alignment angle will vary even for perfectly aligned proteins with rotation around the main axis. Thermal motion acts on the whole protein structure and adds to a broader distribution of chromophore orientations. Furthermore, experimental uncertainties and measuring inaccuracies have to be considered. eGFP molecules are aligned more homogeneously on the electrode centers and along the edges. In those areas, the fluid flow or the electric field lines are in parallel. Contrary, the electric field lines diverge at the tips and cause a higher variation in molecular orientation.

Sample	I_{max}	I_{min}	Q	Modulation
Wire grid polarizer	24.9	18.0	0.38	100 %
Acridine orange	108	78.4	0.38	100 %
eGFP, electrode center	20.2	16.8	0.20	61 %
eGFP, electrode edge	35.0	29.5	0.19	57 %
eGFP, electrode tip	45.8	41.9	0.16	51 %
eGFP, solution	539	533	0.01	4 %

Table 3.2: Minimal and maximal intensities and the corresponding intensity modulation of immobilized eGFP and of control samples.

Transition dipole moment orientation

The angle of the chromophore plane in relation to the protein's symmetry axis δ can be derived from X-ray crystallographic data. Yet in the original publication for the protein structure determination of GFP this angle δ is not precisely given. It is referred to as "roughly perpendicular (60°)" [109], which probably means that the angle was estimated to lie within the range of 60° to 90°.

As the fluorescence intensity modulation is influenced by the orientation of the chromophore's TDM with respect to the protein's symmetry axis, the angle δ can also be derived from the fluorescence intensity modulation upon excitation with differently polarized light. From the similarity of the protein structures of GFP and eGFP and the orientation of their TDMs [111], it is reasonable to assume a similar angle δ for eGFP and GFP. An angle of 60° as mentioned in reference [109], however, would lead to a significant decrease in fluorescence modulation as compared to δ = 90°. The decrease in fluorescence modulation from measurements with polarized light was quantified by numerical integration over the absorption cross section for a complete turn around the protein's longitudinal axis (Fig. 3.29). For the calculation, it was assumed that proteins

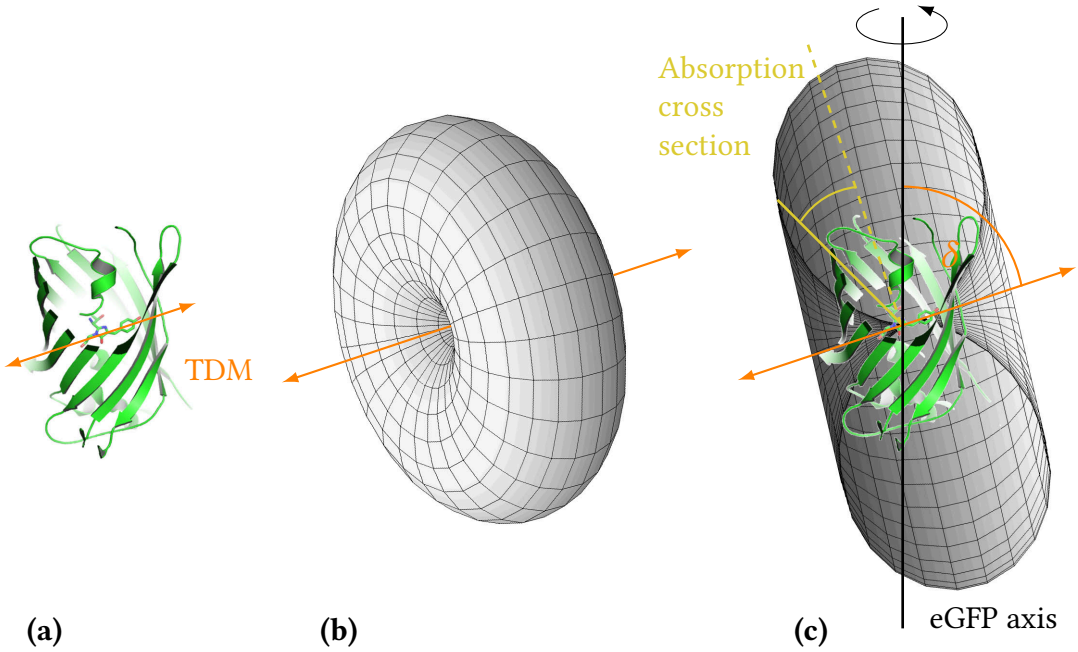

Figure 3.29: a) Ribbon diagram of the eGFP structure, cut open to reveal the chromophore with its transition dipole moment (TDM); b) Absorption cross section (torus surface) of the chromophore's TDM; c) Orientation of the angle δ between the TDM and the protein's longitudinal axis. The torus is cut open to illustrate the absorption cross section for a specific excitation polarization angle (yellow).

were aligned perfectly and that measurements were done with an ideal experimental setup. In this theoretical scenario, an angle $\delta = 60°$ would result in a variation of the TDM orientation by ± 30°, and the intensity modulation would consequently decrease to only 29 %. It would decrease further for real measurements with an imperfect optical setup.

Since the experimentally obtained modulation values reach up to 61 %, the angle between the chromophore's TDM and the protein's longitudinal axis must be closer to 90°. Numerical integration gave an angle $\delta = 73°$ that is further supported by close inspection of the 3D X-ray data. An angle δ between 70° and 75° was determined in this work from the X-ray crystal model (PDB ID: 2y0g) using the molecular viewers *VMD* and *PyMOL*. The very good agreement with the calculation demonstrates that AC electrokinetic immobilization together with fluorescence polarization can be employed for the investigation of TDM orientation within molecules without the need for crystallization, and, hence, *in situ* or even *in vivo*.

3.4.4 Discussion

The aligning action of electric fields on elongated micro- and nanoparticles has been investigated in the last decade mainly for conducting and semiconducting materials that are of interest for nanomaterial assemblies [80]. A similar orienting effect could be expected in principle for protein molecules in spite of their more globular shapes. In this work, a setup and measurement protocol for orientational detection was developed based on a fluorescence microscope. Acridine orange molecules were aligned in a liquid crystal in a DC electric field and were used as a positive control to compare and rate different polarizer configurations of the setup.

A solution of fluorophores was used as a negative control. Principally, fluorophores in solution have rotational and translational freedom. Short-range interactions between proteins or between proteins and the surface can, however, lead to temporary orientational effects. If such a sample is considered as a reference and its data is used to correct the data from the sample of interest, the so-determined degree of alignment will have the tendency to be underestimated.

The polarizing effects of the setup and of the dichroic mirror in particular were corrected using intensity data of a negative control. While this works fine for bright samples with a high degree of alignment, the correction might be insufficient for samples with a low degree of alignment, which lead to only weak intensity modulations. Therefore, multiple data sets at different sample orientations were included in the measurement protocol for a definite proof of alignment.

Two inherently different biomolecules, dsDNA and eGFP were aligned in the electric fields that had been applied to IDE. Stretching of DNA in AC electric fields had been described in literature before [23, 32, 155, 156, 157, 158]. Therein, fluorescence microscopy was used for observation. Mostly, a frequency of 1 MHz was applied for alignment, which is consistent with the results from this thesis. The orientational effect was explained by interactions of the induced dipole moment with the external electric field. As in most publications, no permanent immobiliation of the DNA strands was achieved at the IDE used in this work. Despite the dynamic formation of DNA strands between the IDE, an orientation of the DNA strands parallel to the electric field could be determined. The orientation of the intercalating fluorescence dye PicoGreen was further determined to be perpendicular to the DNA long axis, as was expected from intercalation of the dyes between the dsDNA base pairs. These results confirm the alignment of DNA strands that had been indicated by the presence of fluorescent bands between the IDE. It further suggests that this method is suitable for more detailed investigations of the binding mechanisms of DNA stains. Similar experiments are known from the literature for the fluorescence dye YOYO, where the orientation of the dyes,

when intercalated into stretched DNA strands, was determined by fluorescence polarization [159, 160]. For further experiments involving aligned DNA molecules, it is advisable to attach the ends of the strands or the complete strands to reduce detachment, reformation and realignment of DNA in the ROIs for evaluation. Attachment of the DNA strands at the ends can be achieved by using thiol-bonds [29, 30, 31] or biotin-avidin bonds [32].

Aligned immobilization of proteins by AC electric fields has not been reported so far. In this work, aligned immobilization of eGFP occurred at the tips, edges and centers of IDE. From DEP theory, only immobilization at electrode tips and along the edges close to the tips is expected, since $\nabla|E|^2$ and, hence, DEP attraction is strongest in those areas. As opposed to that, $\nabla|E|^2$ has a local minimum on the centers of the electrodes. However, the presented results are supported by similar immobilization patterns that had been reported for polystyrene particles at a frequency of 70 kHz in experiments with castellated electrodes [161] and at IDE with applied frequencies between 1 kHz to 30 kHz [162]. The immobilization patterns can be explained by an interplay of positive DEP, which causes a downward force, and AC EOF, which moves the particles towards the electrode centers. As the tangential components of the electric field are responsible for electroosmotic flow [14, 74, 161], the direction of the flow points towards the electrode centers resulting in particle accumulation along the electrodes' long axes. Immobilization on the electrode centers started at a distance of about 2 µm from the electrode tips. In Uppalapati's publication on microtubule accumulation, a similar behavior was described: Accumulation started at a frequency-dependent (< 500 kHz) distance from the electrode gap [97]. According to the detailed discussion of forces in non-uniform AC electric fields by Castellanos et al. [14], positive DEP and AC EOF are expected to be the dominating forces responsible for particle motion in our setup with low conductivities of the protein solutions and applied frequencies of 100 kHz.

An interplay of DEP, AC EOF and additional electrothermal flows has also been reported in combination with orientational effects on, e.g., gold nanorods [163] or microtubules [97] that were aligned with their long axes parallel to the electric field. This is in agreement with the newly presented results from eGFP alignment, where the proteins were also aligned parallel to the electric field. Hence, it is reasonable to assume the same orientation mechanism for the proteins even though their aspect ratio of 1.75 is significantly lower than that of, e.g., actin filaments, microtubules or DNA, which commonly have lengths in the micrometer range and diameters in the nanometer range, giving aspect ratios between 100 and 1000. Under the influence of an external electric field, these non-symmetrical objects experience a torque on their induced dipoles, which is commonly held responsible for their alignment with the electric field

[96, 155, 156].

From the aligned eGFP molecules, structural information was deduced in this work from the fluorescence intensity modulations upon polarized excitation. The angle between the chromophore plane and the protein's long axis, which is not discussed in the original publication on the crystal structure [110], was calculated to be 73°, which is in good agreement with the X-ray crystal model. An even more exact determination might be possible using partial de-excitation to narrow the polarization of the excitation light [164].

3.5 Additional applications using gold-plated electrodes

Electric field-assisted immobilization of biomolecules on metal electrodes, and aligned immobilization in particular, has been proven to be useful as one of the first steps in various applications. Gold is widely used as electrode or surface material for bioanalytic applications. The reactivity of gold with sulfur-containing molecules offers versatile possibilities for surface modifications and coupling of biomolecules. As gold electrodes cannot be fabricated directly in the clean rooms at IHP, other electrode materials have to be gold-plated after chip fabrication. In this section, the gold-plating of tungsten cylinder electrodes is described along with first experiments aiming at future applications of nanostructured gold electrodes in bioanalytic applications.

3.5.1 Electrolytic gold-plating of tungsten cylinder electrodes

At the IHP, where the tungsten electrode arrays were fabricated, a protocol for electroless gold-plating had been established within the scope of a diploma thesis [165]. Therein, major challenges involved adhesion of the gold structures and control over their sizes. The latter is more easily achieved using electroplating, which offers the possibility to adjust parameters like the applied voltage and current during an ongoing experiment.

Tungsten dissolution

Tungsten electrode arrays and a gold-plated copper wire were incubated in gold-plating solution, and voltages between 1.0 V to 3.0 V were applied. After varying experiment durations, the electrode chip was rinsed and dried. The success of gold-plating experiments was investigated using a SEM combined with EDX. What striked first in the elemental analysis was the absence of tungsten at the locations of non-contacted

electrodes. Only aluminum and traces of titanium from the underlying layer were detected (Fig. 3.30). The same elements were detected for unsuccessful gold-plating experiments at current densities below 400 A m^{-2}. These results indicate a dissolution of tungsten in the gold plating solution. The following dissolution mechanism was suggested in the literature [166, 167]:

$$\begin{array}{ccc} W + 6\,K_3[Fe(CN)_6] + 6\,KOH & \longrightarrow & WO_3 + 6\,K_4[Fe(CN)_6] + 3\,H_2O \\ WO_3 + 2\,KOH & \longrightarrow & K_2WO_4 + H_2O \\ \hline W + 6\,K_3[Fe(CN)_6] + 8\,KOH & \longrightarrow & K_2WO_4 + 6\,K_4[Fe(CN)_6] + 4\,H_2O \end{array}$$

The dissolution of tungsten in the gold-plating solution was verified with a negative control, for which the electrode chip was incubated with gold-plating solution for 15 min without applying a voltage. In the subsequent EDX analysis, no tungsten was detected. As successful gold-deposition had been achieved despite tungsten dissolution, no alternative gold-plating solution was tested. To prevent or reduce the dissolution of tungsten, the voltage for gold-plating was applied prior to addition of the plating solution in all further experiments.

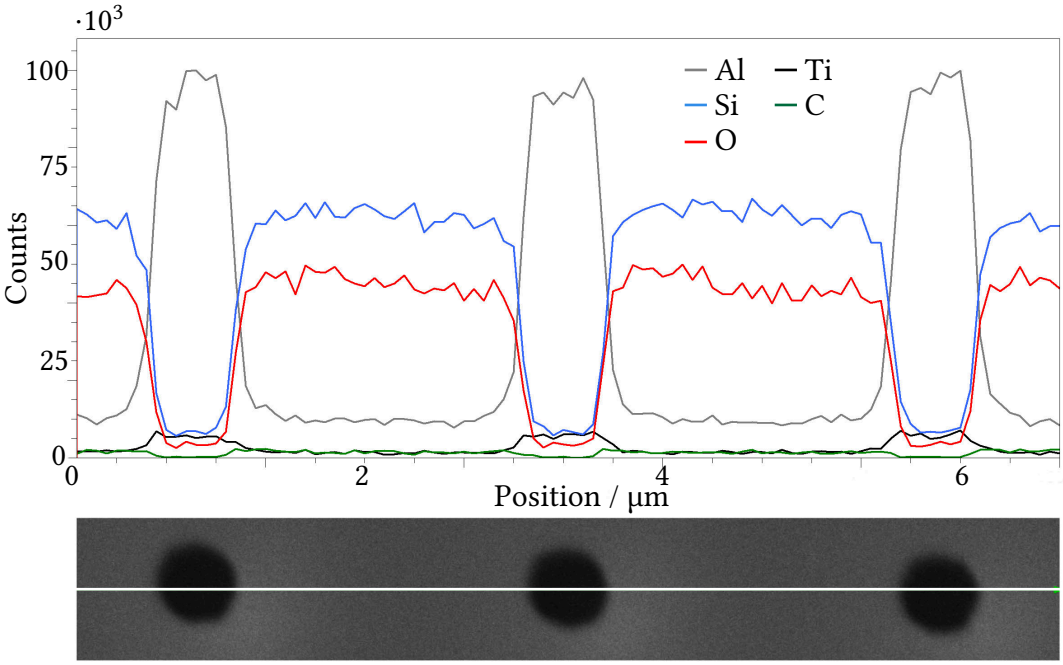

Figure 3.30: EDX elemental line scan of three hollow cylinders that used to be filled with tungsten.

Growth of gold structures

The experimental parameters that influence the gold-plating process are the applied voltage, the number or, more precisely, the surface area of electrodes to be plated, and the duration of the experiment. These parameters determine the current density and the change in electric charge that is needed for the deposition of gold. A limitation of the current density decelerates the electrodeposition process and might, hence, help to gain better control over the gold structures. The influence of various parameters was investigated with the aim to achieve homogeneous gold structures on all electrodes. For the limitation of current density, a resistor with $1 \cdot 10^6\,\Omega$ was used in some experiments. Voltages between 1.0 V and 3.0 V were applied for durations of 0.17 min to 30 min. The current measured was 1.6 µA to 7.0 µA at current densities of $0.5\,\mathrm{A\,m^{-2}}$ to $1800\,\mathrm{A\,m^{-2}}$. The parameters are summarized in Table 3.3.

Chip name	Voltage [V]	Duration [min]	Current density [$\mathrm{A\,m^{-2}}$]	Gold structure
W86	1.0	17	400	Rings (Fig. 3.31a)
W95	1.0	15	600	Dendritic spheroids
W88	1.0	15	600	Dendritic rings (Fig. 3.31b)
W81	1.5	3	900	Large spheroids; smaller polyhedra
W90	1.5	0.5	1400	Large spheroids; smaller polyhedra; dendritic rings (Fig. 3.31d)
W84	1.5	0.5	1800	Large spheroids (Fig. 3.31e)
W85	1.5	0.17	1800	Large spheroids
W133	3.0	30	500	Agglomerates of smaller spheroids (Fig. 3.31c)
W130	3.0	30	700	Agglomerates of smaller spheroids
W131	3.0	30	1300	Rose petal-like, merged gold structures (Fig. 3.31f)

Table 3.3: Effect of experimental parameters for electrolytic gold-plating of tungsten cylinder electrodes on the structure of deposited gold.

Only at current densities of approximately $400\,\mathrm{A\,m^{-2}}$ or higher, gold was detected at the locations of contacted electrodes. The gold structures were investigated using the SEM. On some chips, the gold deposits were even visible with a light microscope. The detected gold deposits differed in structure and size. There were, e.g., rings of gold, polyhedra or spheroids. In the center of some of the gold rings, no tungsten was detected. Apparently, gold deposition was not dependent on the presence of tungsten. This was verified by reusing an electrode chip where the first gold-plating attempt (1.0 V, $400\,\mathrm{A\,m^{-2}}$) had failed, and the tungsten had been dissolved. The second attempt at a higher voltage (3.0 V, $900\,\mathrm{A\,m^{-2}}$) was successful. From this follows a gold depo-

sition beginning at the edges of the TiN hollow cylinders that normally enclose the tungsten electrodes. In the course of the plating process the deposits grow and form differently sized gold aggregates whose shapes depend presumably on the growth velocity that is determined by the current density.

At lower current densities, the growth of gold structures was slower than tungsten dissolution, which lead to the deposition of gold rings along the TiN edges (Fig. 3.31a).

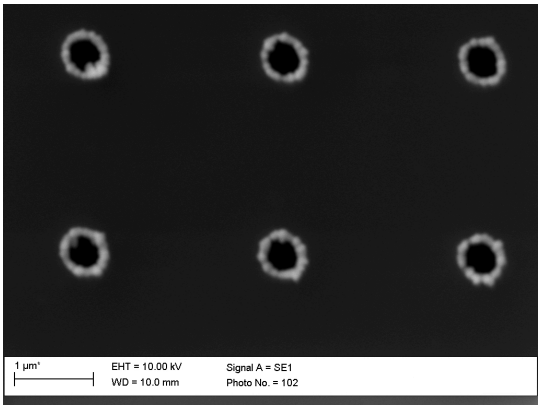

(a) Rings.

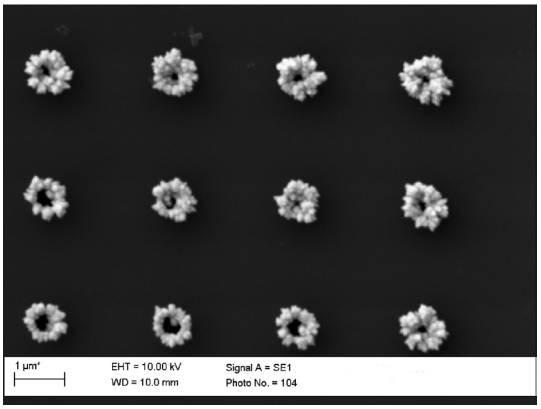

(b) Dendritic rings.

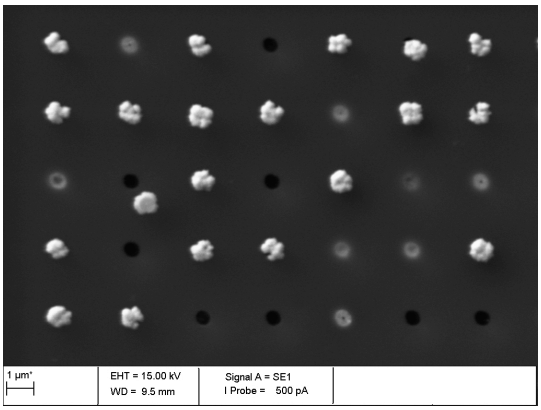

(c) Agglomerates of smaller spheroids.

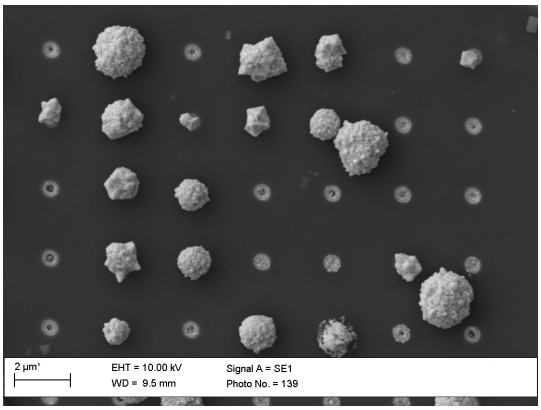

(d) Large spheroids, smaller polyhedra.

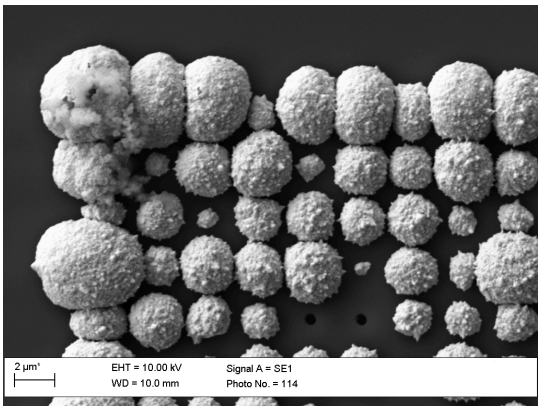

(e) Large spheroids.

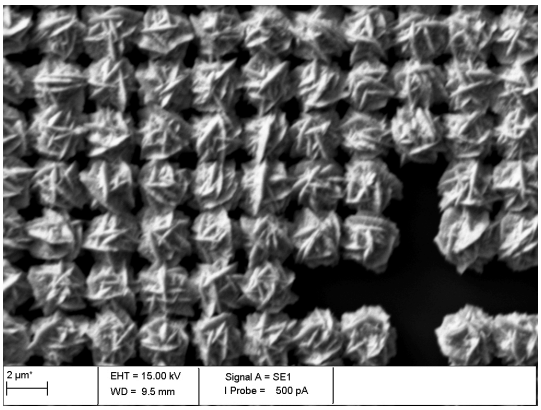

(f) Rose petal-like gold structures.

Figure 3.31: Gold-plated tungsten electrodes with different gold structures; SEM micrographs.

With longer experiment duration, dendritic structures grew from the rings (Fig. 3.31b). At higher current densities, gold was again deposited at the electrode edges at first, but tungsten signals in the EDX spectra gave evidence that gold growth was faster than tungsten dissolution. As a result, the whole tungsten surface was covered by gold in the course of an experiment. Here, spherical shapes of gold particles were favored (Fig. 3.31e). In longer experiments at high current densities, rose petal-like structures were formed (Fig. 3.31f).

On some chips, the gold particles were not homogeneous in size and shape, and some of the electrodes were not covered by gold. This is either the result of inactive electrodes that are not properly connected to the underlying metal layer for the electric contact or the result of insufficient adherence of some gold particles. If the gold particles are removed during an experiment, e.g. by fluid flow, it might cause delayed growth of new gold particles that in consequence are smaller.

Gold adherence

Gold particles were observed to be partially removed as a result of fluid flow during experiments or of rinsing and drying the chips afterwards. Therefore, gold adherence was investigated using strips of adhesive tape that were pressed onto the dry chips with gold-plated electrodes and subsequently removed. Some gold particles were removed with the strip depending on their size, which was discernible on micrographs of the chips showing less gold particles. Larger gold particles (Fig. 3.32a vs. 3.32b) were more likely to be removed than small gold particles (Fig. 3.32c vs. 3.32d). The lower adherence of big gold particles might be the result of their higher growth velocity, where the contact of gold to the underlying material is not as close as it is expected for slower growth.

In addition to a reduced current density, which reduces the growth velocity, the adherence of gold on metal surfaces after plating processes can be enhanced by cleaning steps prior to plating and by annealing after plating. Clean surfaces minimize the inclusion of contaminants and enable better controlled growth. Pre-cleaning with isopropanol/ethanol or with 10 % hydrochloric acid was tested. However, there were no discernible effects of the pre-treatment on the plating process or gold adhesion. This is probably due to the low contamination of the electrode chips that had been manufactured in clean rooms.

Another option to gain better adherence is annealing after the plating process. High temperatures stimulate thermal motion and facilitate atomic rearrangements towards higher ordered structures and, hence, more stable bonds. Electrode chips with differently sized gold structures were annealed at 300 °C for 30 min. Annealing significantly

reduced the amount of gold particles removed by adhesive strips for small gold particles (Fig. 3.32e vs. 3.32f), whereas large particles were still removed to a large extent.

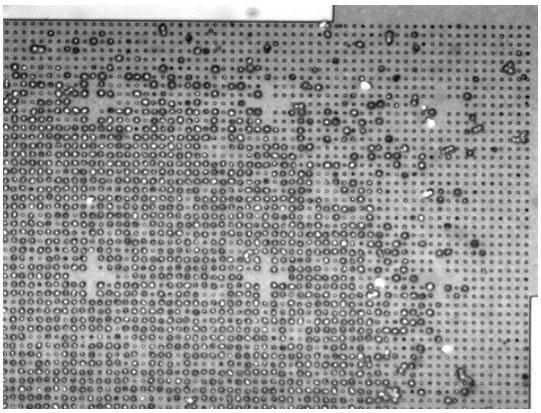

(a) Large gold particles before adherence test.

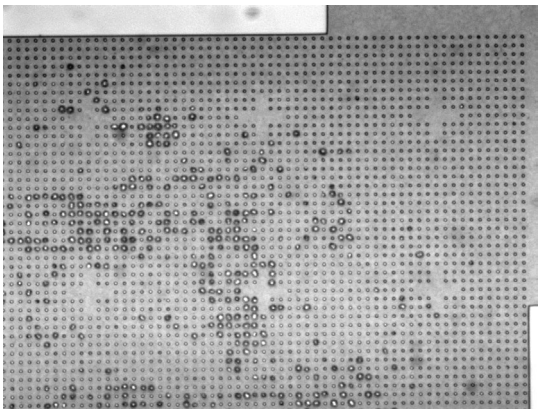

(b) Large gold particles after adherence test.

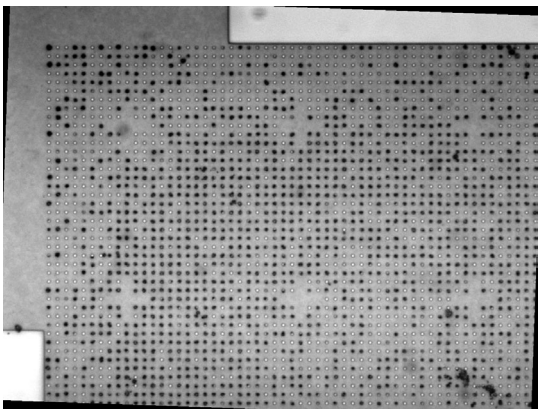

(c) Small gold particles before adherence test.

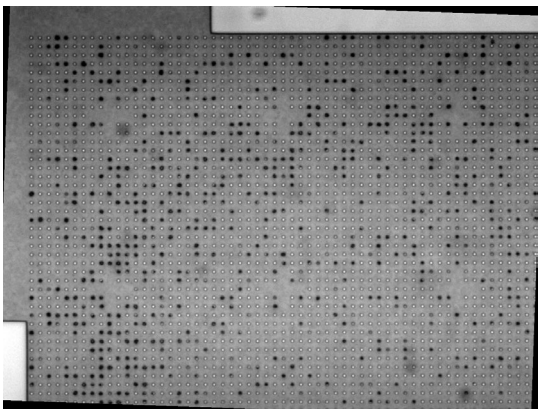

(d) Small gold particles after adherence test.

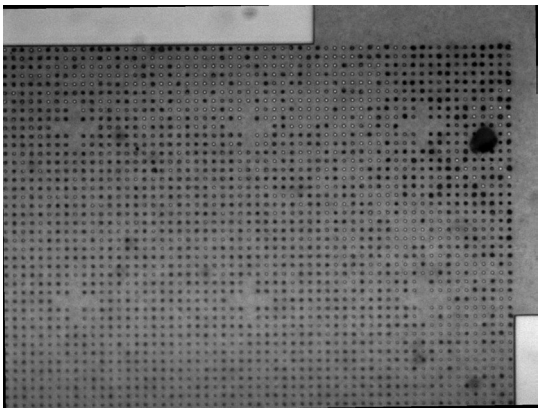

(e) Small gold particles before annealing and adherence test.

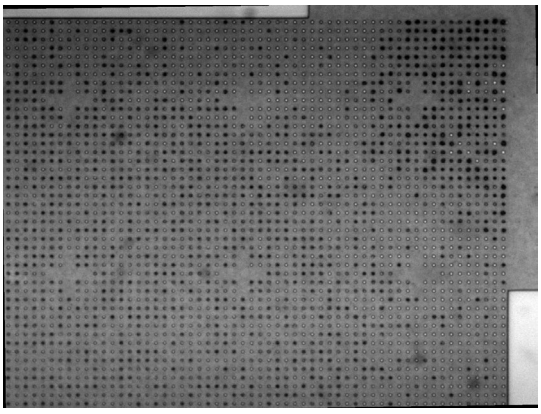

(f) Small gold particles after annealing and subsequent adherence test.

Figure 3.32: Gold-plated electrodes before (a, c, e) and after (b, d, f) adherence tests; incident light micrographs.

Carbon contamination

A further aspect that was noted was the effect of SEM measurements on the appearence of electrode chips and on subsequent gold-plating processes. Regions that had been scanned with the SEM appeared darker in both light and scanning electron micrographs. This can be explained as follows: In those regions, volatile hydrocarbon compounds that had been adsorbed on the chip surface were presumably cracked by the electron beam and subsequently polymerized [168]. High magnifications accelerated this process due to the increased exposure to the electron beam. The polymeric layer covered the whole surface including the electrodes, thus shielding the electric contact. This prevented gold deposition in a gold-plating experiment after SEM measurements, where sections of all four subarrays had been scanned prior to plating (Fig. 3.33a). In the scanned region, no deposition of gold occurred, while gold deposits were detected on most remaining electrodes (Fig. 3.33b). Thus, selective inactivation of specific electrode areas can be achieved, giving the opportunity to use a standardized electrode array for diverse experiments and to introduce substructures according to present needs.

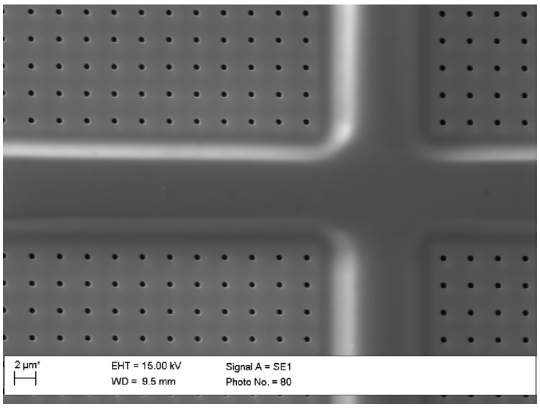

(a) Electrode chip, scanned before gold-plating.

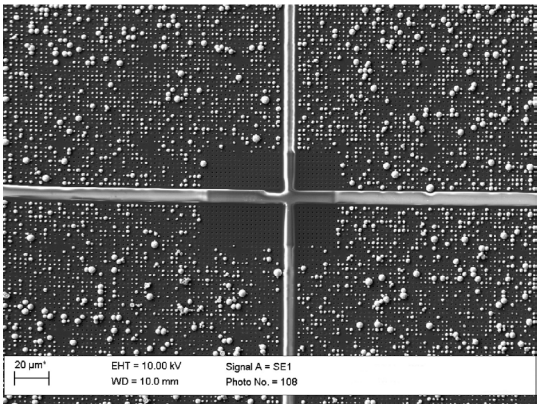

(b) The same electrode chip at lower magnification, scanned after subsequent gold-plating.

Figure 3.33: Effect of carbon contamination in SEM measurements prior to gold-plating experiments; SEM micrographs.

Hydrocarbon contamination of the samples can be reduced by cleaning the samples with solvents like acetone or ethanol and by wearing gloves while loading the sample chamber of the SEM. The main contamination, however, is probably caused by atmospheric hydrocarbons and oil from the vacuum pump. Consequently, electrode chips should not be characterized by SEM/EDX before gold-plating.

3.5.2 Immobilization and activity of enzymes on gold-plated electrodes

Immobilization of proteins, and of enzymes in particular, on gold electrodes is part of numerous bioanalytic methods, and there exists a pool of established protocols for covalent coupling reactions. One of these standard protocols was applied to the gold-plated electrodes, as was the newly developed dielectrophoretic immobilization method.

Covalent immobilization

Gold-plated electrodes were incubated in mercapto undecanoic acid (MUA) to allow adsorption of their thiol groups on the gold surface. MUA is known to form self assembled monolayers (SAM) on gold [169]. For functionalization of the gold-plated electrodes, however, it was not necessary to obtain monolayers. The carboxyl groups of MUA were activated by a mixture of 1-ethyl-3-(3-dimethylaminopropyl)carbodiimide (EDC) and *N*-hydroxysuccinimide (NHS). Enzyme immobilization was accomplished by subsequent addition of a solution of HRP or HRP-Oyster-555, respectively. After HRP-Oyster-555 immobilization, the chips were investigated by fluorescence microscopy. However, the fluorescence of the label was presumably quenched by gold, so that no fluorescence could be detected at the electrodes. Addition of DHR, the non-fluorescent substrate for HRP, with H_2O_2 as co-oxidant, caused fluorescence in the wavelength range of the oxidation product Rh123 located at individual electrodes. Whilst the direct detection of immobilized enzymes was not possible, their presence could be proved by the subsequent enzymatic reaction. The fact that Rh123 fluorescence is not quenched might be the result of the larger distance of these fluorophores to the gold surface compared to the labels that are directly attached to the enzymes.

Dielectrophoretic immobilization

Gold-plated electrodes were used for dielectrophoretic immobilization of proteins. A solution of HRP-Oyster-555 was used, and the success of the immobilization reaction (10 kHz, 10 V, 10 min) was investigated using fluorescence microscopy by comparing fluorescence micrographs before and after DEP. Some of the gold-plated electrodes showed photoluminescence in a broad wavelength range that was detected with different emission filters, including the filter matching the emission of HRP-Oyster-555, which rendered evaluation difficult. Some luminescing electrodes appeared dark after DEP, probably caused by immobilized proteins that shielded the gold surface and reduced or prevented plasmonic excitation, or by fluorescence quenching on gold. Some

individual electrodes, however, showed fluorescence that had not been detected before DEP. As a consequence, quantification was not possible. Although the luminescence processes are not understood at this point, these experiments show the applicability of dielectrophoretic immobilization on gold-plated electrodes.

3.5.3 Raman measurements of horseradish peroxidase on gold-plated electrodes

HRP was dielectrophoretically immobilized on gold-plated electrodes using conditions optimized for tungsten electrodes (10 kHz, 12 V, 5 min to 10 min). The gold particles had different sizes and shapes as a result of the experimental parameters used for gold-plating. Both native HRP and HRP-Oyster-555 were immobilized to identify any influence of the label on the Raman measurements. Control samples were prepared on electrode chips where HRP or HRP-Oyster-555 solution was dried without field application. As a further control, HRP was dielectrophoretically immobilized on non-plated tungsten electrodes. An overview of the samples prepared for Raman measurement is given in Table 3.4.

Chip	Gold-plating	Sample	Enzyme immobilization	Raman
W62	-	HRP-Oyster-555	DEP: 10 kHz, 12 V, 8 min	No signals
W91	Small particles	HRP-Oyster-555	DEP: 10 kHz, 12 V, 9 min	No signals
W96	Large particles	HRP-Oyster-555	DEP: 10 kHz, 12 V, 5 min	No signals
W98	Large particles	HRP-Oyster-555	Dried from solution	Broad signals
W97	Large particles	HRP	DEP: 10 kHz, 12 V, 10 min	No signals
W92	Small particles	HRP	DEP: 10 kHz, 12 V, 10 min	No signals
W93	Small particles	HRP	Dried from solution	Distinct signals

Table 3.4: Overview of the samples with fluorescenctly labeled and unlabeled horseradish peroxidase on gold-plated electrodes used for Raman measurements.

Raman measurements were conducted by Dr. Khoa Ly from TU Berlin. Excitation with a 413 nm laser was expected to yield Raman spectra without surface enhancement effects. Unfortunately, such a spectrum was only obtained for the control sample with dried HRP (Fig. 3.34, W93, yellow). The control sample with dried HRP-Oyster-555 showed broadened signals caused by the fluorescence label. (Fig. 3.34, W98, orange). For samples with dielectrophoretically immobilized HRP or HRP-Oyster-555, no Raman signals occurred. The amount of enzyme on these samples is probably too low, since only a fraction of the protein is immobilized from solution under the experimental conditions used.

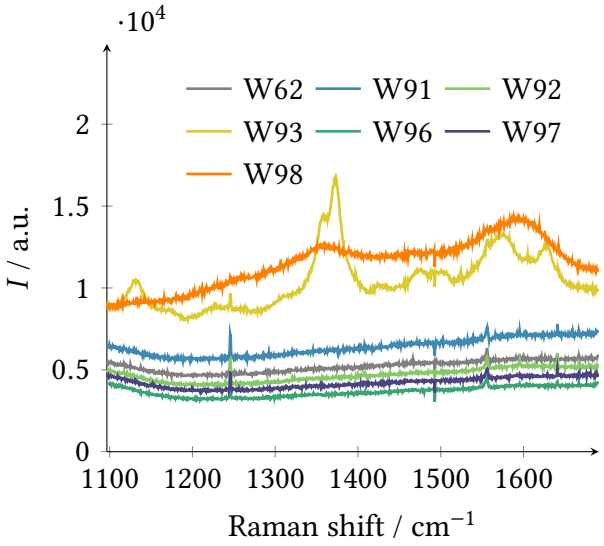

Figure 3.34: Raman measurements of several samples with fluorescently labeled and unlabeled horseradish peroxidase.

3.5.4 Discussion

A protocol for electrolytic gold-plating of tungsten cylinder electrodes was developed. The effects of experimental parameters on the size and shape of gold deposits were investigated. All parameters that influence the current density, namely the applied voltage, the optional series resistor for current limitation, and the number of contacted electrodes, were decisive for the size and shape of gold deposits. Gold adhesion was better for slowly grown structures, and it was further improved by annealing of the chips in succession to plating. At slow growth conditions, however, the electrode material tungsten might be dissolved by the gold-plating solution used. While this did not hamper gold deposition in general, the use of an alternative gold-plating solution might be advisable for future experiments that require slowly grown structures.

The gold-plated electrodes were considered as a platform for additional bioanalytical applications. Both immobilization approaches, covalent coupling and dielectrophoretic immobilization, seemed to work on the gold-plated electrodes. While the dielectrophoretic method is accomplished in one step, the covalent approach on SAM provides more variability concerning further modifications that might be necessary for the use in biosensors [152, 170]. Due to the complex luminescent effects of gold, especially when being nanostructured [171], no quantification of immobilized enzymes was possible from fluorescence measurements. The same holds true for enzymatic activity. As the gold-plated electrodes exhibit differently structured surfaces, a quantification using the AFM is not productive. An approach to quantification via fluorescence intensities would be to use of a linker to separate the proteins from the gold surface,

since the quenching effects are distance-dependent [172]. Despite the benefit of a spatial separation for evaluation of immobilization success and enzymatic activity, it is disadvantageous for Raman spectroscopy, in particular for SERS, where the proximity of gold nanostructures is exploited for signal enhancement [173]. Alternatively, fluorescence lifetime imaging might be a promising approach to differentiate the signals.

First Raman measurements were done by the cooperation partners from TU Berlin. The fluorescence label was found to seriously broaden the Raman signals, which is why future experiments should be done with unlabeled proteins only. As the samples prepared with dielectrophoretically immobilized enzymes gave no signals, the immobilization conditions have to be optimized to gain much higher protein amounts on the electrodes.

4 Conclusions and summary

4.1 Conclusions

In this thesis, biomolecules like proteins and DNA were aligned and immobilized at nanoelectrodes using an electric field-assisted method. Dielectrophoresis is the most important electrokinetic effect that occurs in the applied inhomogenous electric fields. General investigations of molecular dielectrophoresis are sometimes impeded by other interfering electrokinetic effects that lead to motion of the molecules. While there were systematic studies on the influence of particle radius, medium conductivity and the applied frequency and voltage [14], there had been no attempt to minimize alternating current electroosmotic flow through a suitable electrode configuration so far. In this thesis, an electrode configuration was used that had been designed with the intention to reduce tangential components of the electric field and the associated alternating current electroosmotic flow. This electrode configuration consists of a nanoelectrode array for protein attraction and a distant counter electrode, and this geometry has been adapted by other working groups in the meantime [55]. The nanoelectrodes were used for general investigations of molecular dielectrophoresis with the protein bovine serum albumin (BSA). They comprised the influence of experimental parameters like the frequency and the applied voltage, which are varied in most dielectrophoretic studies, and of different medium conductivities. Several other research groups had previously used BSA in insulator-based setups at varying pH and medium conductivity [44], with different insulating post designs [49], and in electrode-based setups with different electrode gaps [25].

Apart from the parameters that had already been studied, the effect of the experiment duration was quantified in this work, as it had a substantial impact on the amount of collected proteins that were immobilized permanently at the electrodes. Before the work for this doctoral thesis had started, a permanent immobilization of proteins had only been reported once [46]. In that report, nanopillar electrodes were used, and reversible or permanent immobilization of fluorescently labeled BSA was observed in dependence on the electric field strength. An electric field strength of $5 \cdot 10^6\,\mathrm{V\,m^{-1}}$ was necessary for permanent immobilization of BSA, which is one order of magnitude higher than that applied in this work. However, it is not the electric field strength but the gradient of the electric field squared that is decisive for the dielectrophoretic force (Eq. (1.1)). It amounts to $10^{17}\,\mathrm{V^2\,m^{-3}}$ for the nanoarray electrodes and to $10^{20}\,\mathrm{V^2\,m^{-3}}$ for interdigitated electrodes as compared to $10^{14}\,\mathrm{V^2\,m^{-3}}$ to $10^{16}\,\mathrm{V^2\,m^{-3}}$ in other studies, where the attraction of proteins was temporary [41, 49, 72].

It is likely that the electric field strengths or, more precisely, the field gradients needed for permanent immobilization cannot be reached with common electrode configurations. In contrast, these gradients are generated easily with the nanoelectrodes

used in reference [46] and in this thesis, where the radius of curvature at the top of the electrodes is in the low nanometer range and, hence, only a few times larger than that of the biomolecules. Permanent immobilization of proteins or enzymes in particular [118] is a fundamental step in numerous bioanalytic applications and, hence, immobilization protocols that are simple, fast and cost-efficient are highly beneficial for their development.

Beyond the general investigations of molecular dielectrophoresis, the dielectrophoretically immobilized proteins were quantified for the first time in an absolute manner. The volumes of deposited proteins on the electrodes were determined using an atomic force microscope, and a maximal number of proteins contained in those volumes was calculated on the basis of their packing density in crystals. This approach might only give an upper limit at this time, but the calculation can easily be refined as soon as more precise information on the specific protein interactions and their associated packing density is available. In addition to the possibility for an absolute quantification, the effort to operate an atomic force microscope is justified for the detection of samples that cannot be reliably measured by fluorescence microscopy. This applies for unlabeled samples, or if the measurements are obstructed by strong luminescent backgrounds. For such samples, this newly developed method is a promising approach to quantification.

With regard to biosensing applications, the proof of a retained biofunctionality of dielectrophoretically immobilized proteins is crucial. Molecular dielectrophoresis of an enzyme had only been demonstrated for ribonuclease A, yet without considering its functionality [40]. Molecular dielectrophoresis of the enzyme horseradish peroxidase was conducted for the first time within this work. What is more, its functionality after dielectrophoretic manipulation was demonstrated. Aside from the publication on the retained binding ability of antibodies after dielectrophoresis [48], which was published nearly at the same time from our working group, this is the only report on the biofunctionality of dielectrophoretically immobilized proteins to date. Long-term storage, which is an important issue for biosensing devices, was also tested for dielectrophoretically immobilized enzymes in this work. The samples could be stored up to two weeks at room temperature. Enzyme stability is a problem also in solution and with other immobilization methods [120]. Hence, the activity decrease of dielectrophoretically immobilized HRP is not a criterion for exclusion of this method for bioanalytical applications, as there remain various storing conditions [174] to be tested in order to delay the activity loss.

With the aim of improving the sensitivity, an aligned immobilization method was desirable. For the investigation of the aligning effect of electric fields, a fluorescence

microscope setup and a suitable measurement and evaluation protocol were developed. As DNA stretching and aligning between opposed, coplanar electrodes have been reported in quite a number of publications [23, 32, 155, 158], it served as a valuable control for the applicability of the protocol. Additionally, information on the binding mechanism of fluorescence stains to DNA can be assessed with this method, which has already been done for some stains [159, 160]. This approach can be extended to other new stains and to fluorescent proteins as well.

The aligned immobilization of proteins by electric fields was demonstrated in this work for the first time. The enhanced Green Fluorescent Protein (eGFP) was chosen for its fluorescence properties that were needed for orientational investigations with the developed optical setup. Interdigitated electrodes were employed despite the greater influence of alternating current electroosmotic flow, because with the optical setup used, the orientation could only be determined for proteins oriented with their longitudinal axes parallel to the surface. In a 3D electrode configuration, however, the proteins would have an upright orientation with relation to the surface. For orientational investigations in such a configuration, total internal reflection fluorescence microscopy might be a suitable technique, as it exhibits polarization also along the z-axis as a consequence of the illumination angle.

The proof of aligned immobilization of proteins is the most important finding of this work as it verifies the initial hypothesis. While the aligned immobilization of conducting and semiconducting nanoobjects by electric fields had been reported multiple times [80], it was not clear if this method would apply to proteins. As the alignment of induced dipoles in the nanoobjects is held responsible for the orientational effect [66, 96, 155, 156, 175], alignment of proteins was not at all obvious because these molecules are smaller and non-conducting. The demonstrated success suggests the electric-field assisted immobilization method for applications that benefit from a specific and homogeneous orientation of proteins. For biosensing reactions, for example, this aligned immobilization could lead to improved sensitivities due to enhanced accessibility of the active sites of enzymes or antibodies. It must be kept in mind, however, that the orientation of the proteins is a result of protein-specific properties and, hence, their induced dipoles. The proteins will always align with the electric field and the direction of alignment can only be influenced by suitable electrode geometries that produce the desired electric field.

In addition to the alignment of the proteins, structural information were derived from fluorescence measurements with polarized excitation: the orientation of the chromophore relative to the eGFP longitudinal axis was determined. The fact that this angle had not been described in the publication on the X-ray crystal structure [110] suggests

the use of polarized light measurements to gain structural information also on other fluorescent proteins without the need to crystallize them.

Control over the orientation of proteins as for example in aligned immobilization is beneficial for bioanalytical studies in view of possibly facilitated access to binding sites, which can lead to enhanced sensitivities of biosensing applications. With regard to bioanalytical applications in general, gold electrodes offer more variability than tungsten electrodes for, e.g. surface enhanced raman spectroscopy [176] or concerning modifications of the surface by covalent or adsorptive attachment of biomolecules [177, 178]. Since gold cannot be employed in the clean rooms of the Leibniz Institute for Innovative Microelectronics (IHP) where the tungsten nanoelectrode arrays are fabricated, the electrodes need to be gold-plated afterwards. An electroless gold-plating protocol had been applied at the IHP with the intention to use the gold-plated electrodes in biosensors [165]. Optimizations of gold deposition in electrodeless systems, however, are limited to the composition of the plating solution, pre- and post-treatment. In contrast, direct influence on the gold deposition rate can be accomplished in electroplating by optimizing the current density. With the same equipment that was used for dielectrophoresis experiments, the tungsten nanoelectrodes were gold-plated successfully. The distribution of deposited gold and the nanostructuring was characterized by scanning electron microscopy.

The gold-plated electrodes with nanostructured surfaces might be beneficial for signal enhancement effects in Raman measurements [173, 179]. The fact that preliminary Raman measurements of horseradish peroxidase on gold-plated electrodes were only successful for those samples with dried enzymes from solution but not for those with dielectrophoretically immobilized enzymes indicates that the gold-plated electrodes are generally suitable for Raman measurements. In the samples with dielectrophoretically immobilized enzymes, the amount of enzymes was probably not high enough and should be increased for future experiments.

All in all, the insights from the presented results contribute significantly to the current research in the field of molecular dielectrophoresis. They further provide the prerequisites for future experiments involving the orientational manipulation of functional biomolecules and possibly an incorporation into diverse bioanalytical applications.

4.2 Summary

Sensitive diagnostic devices are of special interest for prevention, early detection and monitoring of diseases and to assure a suitable treatment. In these devices, miniatur-

ized structures from the semiconductor industry are used more and more frequently, taking advantage of the standardized fabrication protocols and the associated reduced costs for mass production. Micro- and nanostructures are thus accessible that can be used to apply electric fields for the manipulation of biomolecules, e.g. for alignment, accumulation or immobilization. In biosensors, the biomolecules that are responsible for the sensing reaction are immobilized on a transducer surface. The transduced signal is a measure of the concentration of analytes that bind or react with the biomolecules during the sensing reaction. Specific homogeneous orientations of these biomolecules can lead to facilitated access to their active sites and thus to signal enhancement.

In this dissertation, an electric field-assisted method was developed and applied to achieve immobilization and alignment of biomolecules on metal electrodes in a simple one-step experiment. Neither modifications of the biomolecule nor of the electrodes were needed. The two major electrokinetic effects that lead to molecule motion in the chosen electrode configurations used were identified as dielectrophoresis and alternating current electroosmotic flow. To minimize alternating current electroosmotic flow, a new 3D electrode configuration was designed. Thus, the influence of experimental parameters on the dielectrophoretic force and the associated molecule movement could be studied. Permanent immobilization of proteins was examined and quantified absolutely using an atomic force microscope. By measuring the volumes of the immobilized protein deposits, a maximal number of proteins contained therein was calculated. This was possible since the proteins adhered to the tungsten electrodes even after switching off the electric field. The permanent immobilization of functional proteins on surfaces or electrodes is one crucial prerequisite for the fabrication of biosensors.

Furthermore, the biofunctionality of the proteins must be retained after immobilization. Due to the chemical or physical modifications on the proteins caused by immobilization, their biofunctionality is sometimes hampered. The activity of dielectrophoretically immobilized proteins, however, was proven here for an enzyme for the first time. The enzyme horseradish peroxidase was used exemplarily, and its activity was demonstrated with the oxidation of dihydrorhodamine 123, a non-fluorescent precursor of the fluorescence dye rhodamine 123.

Molecular alignment and immobilization - reversible and permanent - was achieved under the influence of inhomogeneous AC electric fields. For orientational investigations, a fluorescence microscope setup, a reliable experimental procedure and an evaluation protocol were developed and validated using self-made control samples of aligned acridine orange molecules in a liquid crystal. Lambda-DNA strands were stretched and aligned temporarily between adjacent interdigitated electrodes, and the orientation of PicoGreen molecules, which intercalate into the DNA strands, was de-

termined. Similarly, the aligned immobilization of enhanced Green Fluorescent Protein was demonstrated exploiting the protein's fluorescence and structural properties. For this protein, the angle of the chromophore with respect to the protein's geometrical axis was determined in good agreement with X-ray crystallographic data. Permanent immobilization with simultaneous alignment of the proteins was achieved along the edges, tips and on the surface of interdigitated electrodes. This was the first demonstration of aligned immobilization of proteins by electric fields. Thus, the presented electric field-assisted immobilization method is promising with regard to enhanced antibody binding capacities and enzymatic activities, which is a requirement for industrial biosensor production, as well as for general interaction studies of proteins.

Bibliography

[1] Global Burden of Disease Study 2013 Collaborators, *Lancet* **2015**, *386*, 743–800.

[2] Price, C. P.; Kricka, L. J. *Clinical Chemistry* **2007**, *53*, 1665–1675.

[3] Smith, R. A.; von Eschenbach, A. C.; Wender, R.; Levin, B.; Byers, T.; Rothenberger, D.; Brooks, D.; Creasman, W.; Cohen, C.; Runowicz, C.; Saslow, D.; Cokkinides, V.; Eyre, H. *A Cancer Journal for Clinicians* **2001**, *51*, 38–75.

[4] Patterson, C.; Feightner, J. W.; Garcia, A.; Hsiung, G.-Y. R.; MacKnight, C.; Sadovnick, A. D. *Canadian Medical Association Journal* **2008**, *178*, 548–556.

[5] Hudson, M. P.; Christenson, R. H.; Newby, L. K.; Kaplan, A. L.; Ohman, E. M. *Clinical Chimica Acta* **1999**, *284*, 223–237.

[6] Torbicki, A.; Perrier, A.; Konstantinides, S.; Agnelli, G.; Galiè, N.; Pruszczyk, P.; Bengel, F.; Brady, A. J. B.; Ferreira, D.; Janssens, U.; Klepetko, W.; Mayer, E.; Remy-Jardin, M.; Bassand, J.-P. *European Heart Journal* **2008**, *29*, 2276–2315.

[7] Peercy, P. S. *Nature* **2000**, *406*, 1023–1026.

[8] Tüdos, A. J.; Besselink, G. A. J.; Schasfoort, R. B. M. *Lab on a Chip* **2001**, *1*, 83–95.

[9] Birkholz, M.; Mai, A.; Wenger, C.; Meliani, C.; Scholz, R. *WIREs Nanomedicine and Nanobiotechnology* DOI:10.1002/wnan.1376.

[10] Turková, J. *Journal of Chromatography B* **1999**, *722*, 11–31.

[11] Rao, S. V.; Anderson, K. W.; Bachas, L. G. *Mikrochimica Acta* **1998**, *128*, 127–143.

[12] Li, M.; Bhiladvala, R. B.; Morrow, T. J.; Sioss, J. A.; Lew, K.-K.; Redwing, J. M.; Keating, C. D.; Mayer, T. S. *Nature Nanotechnology* **2008**, *3*, 88–92.

[13] Nakano, A.; Ros, A. *Electrophoresis* **2013**, *34*, 1085–1096.

[14] Castellanos, A.; Ramos, A.; González, A.; Green, N. G.; Morgan, H. *Journal of Physics D: Applied Physics* **2003**, *36*, 2584–2597.

[15] Ramos, A.; Morgan, H.; Green, N. G.; Castellanos, A. *Journal of Colloid and Interface Science* **1999**, *217*, 420–422.

[16] Green, N.; Ramos, A.; González, A.; Morgan, H.; Castellanos, A. *Physical Review E* **2002**, *66*, 026305.

[17] Pohl, H. A. *Journal of Applied Physics* **1951**, *22*, 869–871.

[18] Pethig, R. *Biomicrofluidics* **2010**, *4*, 022811.

[19] Kang, Y.; Li, D.; Kalams, S. A.; Eid, J. E. *Biomedical Microdevices* **2008**, *10*, 243–249.

[20] Deng, Y.-L.; Chang, J.-S.; Juang, Y.-J. *Bioresource Technology* **2013**, *135*, 137–141.

[21] Yang, J.; Huang, Y.; Wang, X. B.; Becker, F. F.; Gascoyne, P. R. *Biophysical Journal* **2000**, *78*, 2680–2689.

[22] Borgatti, M.; Bianchi, N.; Mancini, I.; Feriotto, G.; Gambari, R. *International Journal of Molecular Medicine* **2008**, *21*, 3–12.

[23] Washizu, M.; Kurosawa, O. *IEEE Transactions on Industry Applications* **1990**, *26*, 1165–1172.

[24] Kumemura, M.; Collard, D.; Yamahata, C.; Sakaki, N.; Hashiguchi, G.; Fujita, H. *ChemPhysChem* **2007**, *8*, 1875–1880.

[25] Zheng, L.; Brody, J. P.; Burke, P. J. *Biosensors and Bioelectronics* **2004**, *20*, 606–619.

[26] Henning, A.; Henkel, J.; Bier, F. F.; Hölzel, R. *PMC Biophysics* **2008**, *1*, 1–12.

[27] Asbury, C. L.; Diercks, A. H.; van den Engh, G. *Electrophoresis* **2002**, *23*, 2658–2666.

[28] Giraud, G.; Pethig, R.; Schulze, H.; Henihan, G.; Terry, J. G.; Menachery, A.; Ciani, I.; Corrigan, D.; Campbell, C. J.; Mount, A. R.; Ghazal, P.; Walton, A. J.; Crain, J.; Bachmann, T. T. *Biomicrofluidics* **2011**, *5*, 24116.

[29] Namasivayam, V.; Larson, R. G.; Burke, D. T.; Burns, M. A. *Analytical Chemistry* **2002**, *74*, 3378–3385.

[30] Kuzyk, A.; Yurke, B.; Toppari, J. J.; Linko, V.; Törmä, P. *Small* **2008**, *4*, 447–450.

[31] Linko, V.; Leppiniemi, J.; Paasonen, S.-T.; Hytönen, V. P.; Toppari, J. J. *Nanotechnology* **2011**, *22*, 275610.

[32] Kabata, H.; Kurosawa, O.; Arai, I.; Washizu, M.; Margarson, S. A.; Glass, R. E.; Shimamoto, N. *Science* **2007**, *262*, 1561–1563.

[33] Rothemund, P. W. K. *Nature* **2006**, *440*, 297–302.

[34] Yamamoto, T. *IEEE Transactions on Industry Applications* **2000**, *36*, 1010–1017.

[35] Regtmeier, J.; Eichhorn, R.; Bogunovic, L.; Ros, A.; Anselmetti, D. *Analytical Chemistry* **2010**, *82*, 7141–7149.

[36] Regtmeier, J.; Eichhorn, R.; Viefhues, M.; Bogunovic, L.; Anselmetti, D. *Electrophoresis* **2011**, *32*, 2253–2273.

[37] Lee, H. J.; Yasukawa, T.; Shiku, H.; Matsue, T. *Biosensors and Bioelectronics* **2008**, *24*, 1000–1005.

[38] Kuo, Z. T.; Hsieh, W. H. *Sensors and Actuators B: Chemical* **2009**, *141*, 293–300.

[39] Hughes, M. P.; Morgan, H. *Analytical Chemistry* **1999**, *71*, 3441–3445.

[40] Washizu, M.; Suzuki, S. *IEEE Transactions on Industry Applications* **1994**, *30*, 835–843.

[41] Hölzel, R.; Calander, N.; Chiragwandi, Z.; Willander, M.; Bier, F. *Physical Review Letters* **2005**, *95*, 128102.

[42] Clarke, R. W.; White, S. S.; Zhou, D.; Ying, L.; Klenerman, D. *Angewandte Chemie* **2005**, *117*, 3813–3816.

[43] Bakewell, D. J. G.; Hughes, M. P.; Milner, J. J.; Morgan, H. *Proceedings of the 20th Annual International Conference of the IEEE Engineering in Medicine and Biology Society* **1998**, *20*, 1079–1082.

[44] Lapizco-Encinas, B. H.; Ozuna-Chacón, S.; Rito-Palomares, M. *Journal of Chromatography A* **2008**, *1206*, 45–51.

[45] Liao, K.-T.; Tsegaqe, M.; Chaurey, V.; Chou, C.-F.; Swami, N. S. *Electrophoresis* **2012**, *33*, 1958–1966.

[46] Yamamoto, T.; Fujii, T. *Nanotechnology* **2007**, *18*, 495503.

[47] Wilson, D. S.; Nock, S. *Current Opinion in Chemical Biology* **2002**, *6*, 81–85.

[48] Otto, S.; Kaletta, U.; Bier, F. F.; Wenger, C.; Hölzel, R. *Lab on a Chip* **2014**, *14*, 998–1004.

[49] Nakano, A.; Chao, T.-C.; Camacho-Alanis, F.; Ros, A. *Electrophoresis* **2011**, *32*, 2314–2322.

[50] Chaurey, V.; Rohani, A.; Su, Y.-H.; Liao, K.-T.; Chou, C.-F.; Swami, N. S. *Electrophoresis* **2013**, *34*, 1097–1104.

[51] Clarke, R.; Piper, J.; Ying, L.; Klenerman, D. *Physical Review Letters* **2007**, *98*, 198102.

[52] Hölzel, R.; Gajovic-Eichelmann, N.; Bier, F. F. *Biosensors and Bioelectronics* **2003**, *18*, 555–564.

[53] Ivory, C. F.; Srivastava, S. K. *Electrophoresis* **2011**, *32*, 2323–1330.

[54] Lesser-Rojas, L.; Ebbinghaus, P.; Vasan, G.; Chu, M.-L.; Erbe, A.; Chou, C.-F. *Nano Letters* **2014**, *14*, 2242–2250.

[55] Schäfer, C.; Kern, D. P.; Fleischer, M. *Lab on a Chip* **2015**, *15*, 1066–1071.

[56] Brooks, P. R. *Science* **1976**, *193*, 11–16.

[57] Beuhler, Jr., R. J.; Bernstein, R. B.; Kramer, K. H. *Journal of the American Chemical Society* **1966**, *88*, 5331–5332.

[58] Stapelfeldt, H.; Seideman, T. *Reviews of Modern Physics* **2003**, *75*, 543–557.

[59] Nevo, I.; Holmegaard, L.; Nielsen, J. H.; Hansen, J. L.; Stapelfeldt, H.; Filsinger, F.; Meijer, G.; Küpper, J. *Physical Chemistry Chemical Physics* **2009**, *11*, 9912–9918.

[60] Sakai, H.; Minemoto, S.; Nanjo, H.; Tanji, H.; Suzuki, T. *Physical Review Letters* **2003**, *90*, 083001.

[61] Lemeshko, M.; Krems, R. V.; Doyle, J. M.; Kais, S. *Molecular Physics* **2013**, *111*, 1648–1682.

[62] Dong, F.; Miller, R. E. *Science* **2002**, *298*, 1227–1230.

[63] Basova, T. V.; Kiselev, V. G.; Plyashkevich, V. A.; Cheblakov, P. B.; Latteyer, F.; Peisert, H.; Chassè, T. *Chemical Physics* **2011**, *380*, 40–47.

[64] Heilmeier, G. H.; Castellano, J. A.; Zanoni, L. A. *Molecular Crystals* **1969**, *8*, 293–304.

[65] Sackmann, E.; Rehm, D. *Chemical Physics Letters* **1970**, *4*, 537–540.

[66] Böhm, K. J.; Mavromatos, N. E.; Michette, A.; Stracke, R.; Unger, E. *Electromagnetic Biology and Medicine* **2005**, *24*, 319–330.

[67] Teixeira-Pinto, A. A.; Nejelski, Jr., L. L.; Cutler, J. L.; Heller, J. H. *Experimental Cell Research* **1960**, *20*, 548–564.

[68] Mischel, M.; Ackermann, R.; Hölzel, R.; Lamprecht, I. *Bioelectrochemistry and Bioenergetics* **1992**, *27*, 413–427.

[69] Iglesias, F.; Lopez, M.; Santamaria, C.; Dominguez, A. *Biophysical journal* **1985**, *48*, 721–726.

[70] Miller, R. D.; Jones, T. B. *Biophysical Journal* **1993**, *64*, 1588–1595.

[71] Nishioka, M.; Tanizoe, T.; Katsura, S.; Mizuno, A. *Journal of Electrostatics* **1995**, *35*, 83–91.

[72] Asokan, S. B.; Jawerth, L.; Carroll, R. L.; Cheney, R. E.; Washburn, S.; Superfine, R. *Nano Letters* **2003**, *3*, 431–437.

[73] Arsenault, M. E.; Zhao, H.; Purohit, P. K.; Goldman, Y. E.; Bau, H. H. *Biophysical Journal* **2007**, *93*, L42–L44.

[74] Morgan, H.; Green, N. *Journal of Electrostatics* **1997**, *42*, 279–293.

[75] Germishuizen, W. A.; Wälti, C.; Wirtz, R.; Johnston, M. B.; Pepper, M.; Davies, A. G.; Middelberg, A. P. J. *Nanotechnology* **2003**, *14*, 896–902.

[76] Lin, H.-Y.; Tsai, L.-C.; Chi, P.-Y.; Chen, C.-D. *Nanotechnology* **2005**, *16*, 2738–2742.

[77] Morrow, T. J.; Li, M.; Kim, J.; Mayer, T. S.; Keating, C. D. *Science* **2009**, *323*, 352.

[78] Freer, E. M.; Grachev, O.; Duan, X.; Martin, S.; Stumbo, D. P. *Nature Nanotechnology* **2010**, *5*, 525–530.

[79] Suehiro, J.; Nakagawa, N.; Hidaka, S.-I.; Ueda, M.; Imasaka, K.; Higashihata, M.; Okada, T.; Hara, M. *Nanotechnology* **2006**, *17*, 2567–2573.

[80] Smith, B. D.; Mayer, T. S.; Keating, C. D. *Annual Review of Physical Chemistry* **2012**, *63*, 241–263.

[81] Pörschke, D. *Biophysical Chemistry* **1987**, *28*, 137–147.

[82] Antosiewicz, J.; Porschke, D. *Biochemistry* **1989**, *28*, 10072–10078.

[83] Porschke, D. *Biophysical Chemistry* **1997**, *66*, 241–257.

[84] Peluso, P.; Wilson, D. S.; Do, D.; Tran, H.; Venkatasubbaiah, M.; Quincy, D.; Heidecker, B.; Poindexter, K.; Tolani, N.; Phelan, M.; Witte, K.; Jung, L. S.; Wagner, P.; Nock, S. *Analytical Biochemistry* **2003**, *312*, 113–124.

[85] Cha, T.; Guo, A.; Zhu, X.-Y. *Proteomics* **2005**, *5*, 416–419.

[86] Wang, X.; Zhou, D.; Sinniah, K.; Clarke, C.; Birch, L.; Li, H.; Rayment, T.; Abell, C. *Langmuir* **2006**, *22*, 887–892.

[87] Turkova, J.; Petkov, L.; Sajdok, J.; Kas, J.; Benes, M. J. *Journal of Chromatography A* **1990**, *500*, 585–593.

[88] Iwakura, M.; Kokubu, T. *Journal of Biochemistry* **1993**, *114*, 339–343.

[89] Pugnière, M.; San Juan, C.; Coletti-Previero, M.-A.; Previero, A. *Bioscience Reports* **1988**, *8*, 263–269.

[90] Cha, T.; Guo, A.; Jun, Y.; Pei, D.; Zhu, X.-Y. *Proteomics* **2004**, *4*, 1965–1976.

[91] Huang, W.; Wang, J.; Bhattacharyya, D.; Bachas, L. G. *Analytical Chemistry* **1997**, *69*, 4601–4607.

[92] Kallwass, H. K. W.; Parris, W.; Macfarlane, E. L. A.; Gold, M.; Jones, J. B. *Biotechnology Letters* **1993**, *15*, 29–34.

[93] Hallett, P.; Offer, G.; Miles, M. J. *Biophysical Journal* **1995**, *68*, 1604–1606.

[94] Anselmetti, D.; Fritz, J.; Smith, B.; Fernandez-Busquets, X. *Single Molecules* **2000**, *1*, 53–58.

[95] Müller, D. J.; Engel, A. *Nature Protocols* **2007**, *2*, 2191–2197.

[96] Minoura, I.; Muto, E. *Biophysical Journal* **2006**, *90*, 3739–3748.

[97] Uppalapati, M.; Huang, Y.-M.; Jackson, T. N.; Hancock, W. O. *Small* **2008**, *4*, 1371–1381.

[98] Schermelleh, L.; Heintzmann, R.; Leonhardt, H. *The Journal of Cell Biology* **2010**, *190*, 165–175.

[99] Betzig, E.; Chichester, R. J. *Science* **1993**, *262*, 1422–1425.

[100] Patra, D.; Gregor, I.; Enderlein, J. *The Journal of Physical Chemistry A* **2004**, *108*, 6836–6841.

[101] Toprak, E.; Enderlein, J.; Syed, S.; McKinney, S. A.; Petschek, R. G.; Ha, T.; Goldman, Y. E.; Selvin, P. R. *Proceedings of the National Academy of Sciences of the United States of America* **2006**, *103*, 6495–6499.

[102] Lieb, M. A.; Zavislan, J. M.; Novotny, L. *Journal of the Optical Society of America B* **2004**, *21*, 1210–1215.

[103] Ha, T.; Laurence, T. A.; Chemla, D. S.; Weiss, S. *The Journal of Physical Chemistry B* **1999**, *103*, 6839–6850.

[104] Axelrod, D. *Biophysical Journal* **1979**, *26*, 557–574.

[105] Natarajan, L. V.; Stein, M. F.; Blankenship, Robert, E.; Chang, R. *Chemical Physics Letters* **1983**, *95*, 525–528.

[106] Güttler, F.; Sepiol, J.; Plakhotnik, T.; Mitterdorfer, A.; Renn, A.; Wild, U. P. *Journal of Luminescence* **1993**, *56*, 29–38.

[107] Inoué, S.; Shimomura, O.; Goda, M.; Shribak, M.; Tran, P. T. *Proceedings of the National Academy of Sciences of the United States of America* **2002**, *99*, 4272–4277.

[108] Forkey, J. N.; Quinlan, M. E.; Goldman, Y. E. *Biophysical Journal* **2005**, *89*, 1261–1271.

[109] Ormö, M.; Cubitt, A. B.; Kallio, K.; Gross, L. A.; Tsien, R. Y.; Remington, S. J. *Science* **1996**, *273*, 1392–1395.

[110] Royant, A.; Noirclerc-Savoye, M. *Journal of Structural Biology* **2011**, *174*, 385–390.

[111] Ansbacher, T.; Srivastava, H. K.; Stein, T.; Baer, R.; Merkx, M.; Shurki, A. *Physical Chemistry Chemical Physics* **2012**, *14*, 4109–4117.

[112] Seebacher, C.; Hellriegel, C.; Bräuchle, C.; Ganschow, M.; Wöhrle, D. *The Journal of Physical Chemistry B* **2003**, *107*, 5445–5452.

[113] Scheller, F.; Schubert, F. *Biosensoren*; Birkhäuser, 1989.

[114] Sethi, R. S. *Biosensors and Bioelectronics* **1994**, *9*, 243–264.

[115] Kimmel, D. W.; LeBlanc, G.; Meschievitz, M. E.; Cliffel, D. E. *Analytical Chemistry* **2012**, *84*, 685–707.

[116] D'Souza, S. F. *Applied Biochemistry and Biotechnology* **2001**, *96*, 225238.

[117] Mongra, A. C. *Journal of Academia and Industrial Research* **2012**, *1*, 310–312.

[118] Brena, B. M.; Batista-Viera, F. *Methods in Biotechnology: Immobilization of Enzymes and Cells*; 2006; pp 15–30.

[119] Welinder, K. G. *European Journal of Biochemistry* **1979**, *96*, 483–502.

[120] Temoçin, Z.; Yiğitoğlu, M. *Bioprocesses and Biosystems Engineering* **2009**, *32*, 467–474.

[121] Jönsson, G.; Gorton, L. *Electroanalysis* **1989**, *1*, 465–468.

[122] Wang, J.; Freiha, B.; Naser, N.; Gonzalez Romero, E.; Wollenberger, U.; Ozsoz, M.; Evans, O. *Analytica Chimica Acta* **1991**, *254*, 81–88.

[123] Ruzgas, T.; Emnéus, J.; Gorton, L.; Marko-Varga, G. *Analytica Chimica Acta* **1995**, *311*, 245–253.

[124] Meng, Y.; High, K.; Antonello, J.; Washabaugh, M. W.; Zhao, Q. *Analytical Biochemistry* **2005**, *345*, 227–236.

[125] Cormier, M. J.; Prichard, P. M. *The Journal of Biological Chemistry* **1968**, *243*, 4706–4714.

[126] Ando, Y.; Kiwa, K.; Yamada, N.; Irie, T.; Enomoto, T.; Kubota, H.; Ohmiya, Y.; Akiyama, H. *Photochemistry and Photobiology* **2007**, *83*, 1205–1210.

[127] Kahn, P.; Idrees, D.; Moxley, M. A.; Corbett, J. A.; Ahmad, F.; von Figura, G.; Sly, W. S.; Waheed, A.; Hassan, M. I. *Applied Biochemistry and Biotechnology* **2014**, *173*, 333–355.

[128] Díaz, A. N.; Sanchez, F. G.; García, J. A. G. *Analytica Chimica Acta* **1996**, *327*, 161–165.

[129] Kamidate, T.; Maruya, M.; Tani, H.; Ishida, A. *Analytical Sciences* **2009**, *25*, 1163–1166.

[130] Kuroda, N.; Murasaki, N.; Wada, M.; Nakashima, K. *Luminescence* **2001**, *16*, 167–172.

[131] Crow, J. P. *Nitric Oxide: Biology and Chemistry* **1997**, *1*, 145–157.

[132] Kubin, R. F.; Fletcher, A. N. *Journal of Luminescence* **1982**, *27*, 455–462.

[133] Wardman, P. *Free Radical Biology and Medicine* **2007**, *43*, 995–1022.

[134] Rasband, W. *ImageJ*; U. S. National Institutes of Health, Bethesda: Maryland, USA, 1997.

[135] Nečas, D.; Klapetek, P. *Central European Journal of Physics* **2012**, *10*, 181–188.

[136] Majorek, K. A.; Porebski, P. J.; Dayal, A.; Zimmerman, M. D.; Jablonska, K.; Stewart, A. J.; Chruszcz, M.; Minor, W. *Molecular Immonology* **2013**, *52*, 174–182.

[137] Coles, M. J. *Molecular Crystals and Liquid Crystals* **1978**, *49*, 13–18.

[138] Lakowicz, J. R. *Principles of Fluorescence Spectroscopy*, 3rd ed.; Springer: New York, 2006.

[139] Thompson, N. L.; McConnell, H. M.; Burghardt, T. P. *Biophysical Journal* **1984**, *46*, 739–747.

[140] Hoettges, K. F.; Hughes, M. P.; Cotton, A.; Hopkins, N. A. E.; McDonnell, M. B. *IEEE Engineering in Medicine and Biology Magazine* **2003**, *20*, 68–74.

[141] Du, J. R.; Juang, Y. J.; Wu, J. T.; Wei, H. H. *Biomicrofluidics* **2008**, *2*, 1–10.

[142] Dürr, M.; Kentsch, J.; Müller, T.; Schnelle, T.; Stelzle, M. *Electrophoresis* **2003**, *24*, 722–731.

[143] Wei, M.-T.; Junio, J.; Ou-Yang, H. D. *Biomicrofluidics* **2009**, *3*, 12003.

[144] Hughes, M. P. *Journal of Colloid and Interface Science* **2002**, *250*, 291–294.

[145] Gunda, N. S. K.; Mitra, S. K. *Biomicrofluidics* **2010**, *4*, 14105.

[146] Barsotti, R. J.; Vahey, M. D.; Wartena, R.; Chiang, Y.-M.; Voldman, J.; Stellacci, F. *Small* **2007**, *3*, 488–499.

[147] Norde, W.; Zoungrana, T. *Biotechnology and Applied Biochemistry* **1998**, *28*, 133–143.

[148] Rothe, G.; Valet, G. *Advances in Cellular Pathology* **1990**, 313–314.

[149] Royall, J. A.; Ischiropoulos, H. *Archives of Biochemistry and Biophysics* **1993**, *302*, 348–355.

[150] Kumemura, M.; Collard, D.; Yoshizawa, S.; Wee, B.; Takeuchi, S.; Fujita, H. *ChemPhysChem* **2012**, *13*, 3308–3312.

[151] Radi, A.-E.; Muñoz Berbel, X.; Cortina-Puig, M.; Marty, J.-L. *Electroanalysis* **2009**, *21*, 696–700.

[152] Wink, T.; van Zuilen, S. J.; Bult, A.; van Bennkom, W. P. *The Analyst* **1997**, *122*, 43R–50R.

[153] Andersson, M. M.; Hatti-Kaul, R. *Journal of Biotechnology* **1999**, *72*, 21–31.

[154] Dragan, A. I.; Casas-Finet, J. R.; Bishop, E. S.; Strouse, R. J.; Schenerman, M. A.; Geddes, C. D. *Biophysical Journal* **2010**, *99*, 3010–3019.

[155] Dewarrat, F.; Calame, M.; Schönenberger, C. *Single Molecules* **2002**, *3*, 189–193.

[156] Germishuizen, W. A.; Tosch, P.; Middelberg, A. P. J.; Wälti, C.; Davies, A. G.; Wirtz, R.; Pepper, M. *Journal of Applied Physics* **2005**, *97*, 014702.

[157] Sung, K. E.; Burns, M. A. *Analytical Chemistry* **2006**, *78*, 2939–2947.

[158] Wälti, C.; Germishuizen, W. A.; Tosch, P.; Kaminski, C. F.; Davies, A. G. *Journal of Physics D: Applied Physics* **2007**, *40*, 114–118.

[159] Larsson, A.; Carlsson, C.; Jonsson, M.; Albinssont, B. *Journal of the American Chemical Society* **1994**, *116*, 8459–8465.

[160] Bennink, M. L.; Schärer, O. D.; Kanaar, R.; Sakata-Sogawa, K.; Schins, J. M.; Kanger, J. S.; de Grooth, B. G.; Greve, J. *Cytometry* **1999**, *36*, 200–208.

[161] Green, N. G.; Ramos, A.; Morgan, H. *Journal of Physics D: Applied Physics* **2000**, *33*, 632–641.

[162] Oh, J.; Hart, R.; Jorge, C.; Noh, H. M. *Lab on a Chip* **2009**, *9*, 62–78.

[163] Ahmed, W.; Kooij, E. S.; van Silfhout, A.; Poelsema, B. *Nano Letters* **2009**, *9*, 3786–3794.

[164] Hafi, N.; Grunwald, M.; van den Heuvel, L. S.; Aspelmeier, T.; Chen, J.-H.; Zagrebelsky, M.; Schütte, O. M.; Steinem, C.; Korte, M.; Munk, A.; Walla, P. J. *Nature Methods* **2014**, *11*, 579–586.

[165] Kitzmann, J. Strukturierte Goldabscheidung mittels Galvanik und PVD. Diplomarbeit, Technische Hochschule Wildau, 2011.

[166] Hampel, C. A. *Industrial and Engineering Chemistry* **1961**, *53*, 90.

[167] Neugebauer, J.; Kiss, K. *Acta Chimica (Budapest)* **1965**, *44*, 241–251.

[168] Reimer, L. *Scanning Electron Microscopy - Physics of Image Formation and Microanalysis*, 2nd ed.; Springer, 1998; pp 130–133.

[169] Bain, Colin, D.; Troughton, E. B.; Tao, Y.-T.; Evall, J.; Whitesides, G. M.; Nuzzo, R. G. *Journal of the American Chemical Society* **1989**, *111*, 321–335.

[170] Frasconi, M.; Mazzei, F.; Ferri, T. *Analytical and Bioanalytical Chemistry* **2010**, *398*, 1545–1564.

[171] Dulkeith, E.; Niedereichholz, T.; Klar, T. A.; Feldmann, J.; von Plessen, G.; Gittins, D. I.; Mayya, K. S.; Caruso, F. *Physical Review B* **2004**, *70*, 205424.

[172] Schneider, G.; Decher, G. *Nano Letters* **2015**, *6*, 530–536.

[173] Xiao, J.; Qi, L. *Nanoscale* **2011**, *3*, 1383–1396.

[174] Ricci, F.; Amine, A.; Palleschi, G.; Moscone, D. *Biosensors and Bioelectronics* **2003**, *18*, 165–174.

[175] Shekhar, S.; Stokes, P.; Khondaker, S. I. *ACS Nano* **2011**, *5*, 1739–1746.

[176] Leung, L.-W. H.; Gosztola, D.; Weaver, M. J. *Langmuir* **1987**, *3*, 45–52.

[177] Veiseh, M.; Zareie, M. H.; Zhang, M. *Langmuir* **2002**, *18*, 6671–6678.

[178] Abad, J. M.; Pita, M.; Fernández, V. M. *Methods in Biotechnology: Immobilization of Enzymes and Cells*; 2006; pp 229–238.

[179] Hossain, M. K.; Kitahama, Y.; Huang, G. G.; Kaneko, T.; Ozaki, Y. *Applied Physics B: Lasers and Optics* **2008**, *93*, 165–170.

A Appendix

A.1 Abbreviations and acronyms

AC	alternating current
AC EOF	alternating current electroosmotic flow
AFM	atomic force microscope
a.u.	arbitrary units
BG	background
BSA	bovine serum albumin
BSA-Oyster-647	bovine serum albumin, labeled with the fluorescence dye Oyster-647
CLSM	confocal laser scanning microscope
CMOS	complementary metal-oxide-semiconductor
DC	direct current
DEP	dielectrophoresis
DHR	dihydrorhodamine 123
DNA	desoxyribonucleid acid
DOL	density of labeling
dsDNA	double-stranded desoxyribonucleic acid
EDC	1-ethyl-3-(3-dimethylaminopropyl)carbodiimide
EDX	energy dispersive X-ray spectroscopy
eGFP	enhanced Green Fluorescent Protein
ELISA	enzyme-linked immunosorbent assay
FCS	fluorescence correlation spectroscopy
GFP	Green Fluorescent Protein
HRP	horseradish peroxidase

HRP-Oyster-555	horseradish peroxidase, labeled with the fluorescence dye Oyster-555
IDE	interdigitated electrodes
IHP	Leibniz Institute for Innovative Microelectronics
ITO	indium tin oxide
MUA	mercapto undecanoic acid
NA	numerical aperture
NHS	*N*-hydroxysuccinimide
PDB ID	Protein Data Bank identifier
Rh123	rhodamine 123
RNA	ribonucleic acid
ROI	region of interest
RPE	R-phycoerythrin
SAM	self assembled monolayers
SAW	surface acoustic wave
SEM	scanning electron microscope
SERS	surface enhanced raman spectroscopy
TDM	transition dipole moment
TFP	tetrafluorophenyl
TIRF	total internal reflection fluorescence

A.2 Symbols and constants

α	polarization orientation angle
β	chip orientation angle
δ	angle between the chromophore's transmission dipole moment and the protein's longitudinal axis

ϵ	molar extinction coefficient
ε_x^*	complex permittivity of a material x
ε_x	relative permittivity of a material x
ε_0	vacuum permittivity
E	electric field strength
EE	enzyme efficiency
F_{DEP}	dielectrophoretic force
h	height
i	imaginary unit
I	intensity
K	Clausius-Mossotti factor
λ	wavelength
∇	gradient
ω	angular frequency
r_p	particle radius
ρ	phase offset
σ_x	electrical conductivity of a material x
t	time
U	voltage
V	volume